Galaxy Evolution with FMOS

Emma Frances Curtis Lake

Physics Department and New College, Oxford

A thesis submitted for the degree of Doctor of Philosophy
in the University of Oxford.

Michaelmas Term 2010

To My Dad

Sorry dad, but you're gonna have to share this one

****

In loving memory of a wonderful girl,
Jane, I am sorry I do not have anything more appropriately fun or interesting to dedicate to you... And there isn't even a single mention of Rugby! Oh, would you look at that, now there is ;-)

Abstract

This thesis is concerned with the targeting of emission line galaxies with FMOS (Fibre Multi-Object Spectrograph) to determine properties of star forming galaxies at redshift ~ 1.5, and provide measurements of the growth rate of large-scale structure through Redshift Space Distortions (RSDs). I also consider the opportunities of targeting the passive galaxy population at high redshift, through measurements of their continuum.

I start with the extensive broad-band photometric data available in the UKIDSS-UDS (United Kingdom Infrared Telescope Deep Sky Survey - Ultra-Deep Survey) field which is used to produce a band-merged catalogue, later used for determining photometric redshifts. In producing this catalogue, I approach the issue of source confusion present in the deep Spitzer imaging using z-band priors on profile position and shape and an iterative Expectation-Maximisation algorithm.

Photometric redshift estimates are compared against color selections as potential targeting techniques for a wide-area redshift survey with FMOS. Different photometric survey areas are considered, and the quality of selection given the available broad-band data tested, by adjusting the photometric catalogue produced for the UDS. The results indicate that the SWIRE (Spitzer Wide area InfraRed Extragalactic Survey) fields are too small to provide adequate sources with a consistent selection mechanism. The CFHTLS (Canada-France-Hawaii Telescope Legacy Survey) would have a large enough area given deeper z'-band imaging, and SWIRE-depth coverage in the Spitzer 3.6 μm and 4.5 μm bands.

I present FMOS commissioning data obtained for the UDS field, including the spectroscopic targeting of sources from the High-Z Emission Line Survey (HiZELS). With this data, I am able to test the current quality of flux calibration using cool stars targeted simultaneously and the level of systematic errors left by sky-subtraction. The sample of HiZELS sources selected to place Hα at z~1.45 show low contamination from other emission lines, and only one out of 9 targets assigned a redshift has any indication of AGN activity.

Finally, I present longslit observations of faint, passive galaxies at redshift ~ 1.9, selected as members of a possible cluster, JKCS 041, selected from broad band colours. One object was observed with high enough signal to noise to constrain the position of the 4000 Å Balmer break, providing a tighter constraint on the photometric redshift of $1.8867^{+0.0034}_{-0.0117}$.

Declaration

I declare that no part of this thesis has been accepted, or is currently being submitted, for any degree or diploma or certificate or any other qualification in this University or elsewhere. Except where explicit reference is made to the work of others, the work contained in this thesis is my own, and is not the outcome of work done in collaboration.

Emma F. Curtis Lake

(November 2010)

Acknowledgements

First I would like to thank my supervisor, Gavin Dalton, for giving me this project in the first place and for the help and advice over the years and the final thesis comments, as well as the many games of pool at HP. I thank Tom Mauch for all his time and support and I want to thank Steve Rawlings for taking an interest and putting me in touch with the Edinburgh group.

Thanks go to Pat Roche and Isobel Hook for reading my yearly reports and offering advice and guidance along the way. Many thanks to Matt Jarvis and Andy Bunker, my examiners, who actually had to read this thing, sorry for boring you guys and thank you for the comments and improvements!

Although it wasn't the best start to my first postDoc, I am so grateful to Ross McLure for being so understanding about the time taken to complete this thesis, as well as giving me a reason to push to finish in the first place! I'm also thankful to have been given such a helpful and understanding office mate, Vivienne Wild, whose useful comments certainly improved this work.

Then there are all the other people that contributed to making my three years in Oxford some of the best years of my life (thus far). To everyone in my year - I'm so glad to have met you all and to have shared wonderful times with you in Oxford - I wish you all luck and, very selfishly, I wish as many of you as possible stay in Astro so that I can try and meet up with you at conferences and departments around the world. Same goes to those in the years above and the years below, thank you for making a lovely, close-knit community of students. It is certainly what has made the time so special! Some special thanks need to be said separately, so here goes:-

Ben - thanks for the inventions
Lisa - thanks so much for the support you offered in the final few months, sorry for crying at you!
Nat - thanks for being an awesome office mate - miss you!
Sam - thanks for bringing in your harp to the office
Nic - thanks for einstein - I'll give him back soon, promise - sorry for stealing him ;-)
Calum - thanks for the poker
Ali - thanks for being that little bit inspirational - even if I stopped running as soon as you left.
Paul - thank you so much for the dancing fun - more to be had I very much hope!
Seb - thank you for the music ;-) heehee, don't really want to add to that
Grandad Ollie - thanks for the wonderful stories
Sarah M - thank you for help with hitchhiker's
Qiang - thank you for letting me talk through problems with you back when we were still office mates
Cedric Ollie - OK, so you weren't part of the department really, but I'll count you here anyway - thanks for the Ollie flatmate weekends.

Then to my two wonderful friends - Sarah B and Graeme - now I have to thank you both separately so don't go getting all silly about who I mention first! Sarah - thank you for the wonderful food, dancing, girlieness, fun, support and friendship. Good luck for your write up! Graeme - thank you for the tea trips, driving three of us to Paris, company on late/all night working sessions and just generally being a true, and wonderful friend. Sorry to both of you if my thanks here do not sufficiently convey the depth of feeling with which I express them.

The only reason I applied to Oxford in the first place was to be able to stay with Eric, and it was certainly worth it. He's probably the reason I can program at all, though he would say that I do so appallingly and would probably prefer that I didn't. Thank you for your patience in the last few months of writing this thesis when I wasn't that fun to live with and for all your support! Let's make sure Edinburgh, and the next place, and the next place are as fun.

Last of all, thanks to my family, and to my Dad in particular. I would obviously not have managed any of this without you putting me through school and University, but more than that, you have always taught us (your children) to think independently and analyse situations from different viewpoints. I enjoy our science/philosophy-based discussions, of which I hope there are many more to come and I hope that I continue to improve those skills that you nurtured (yes, I know, I sneered at that word also). So, I dedicate this thesis to you... can I consider it a debt re-paid?! Ha - that would be poor payment indeed!

Contents

Chapter 1

Introduction

The Fibre Multi-Object Spectrograph (FMOS, Kimura et al. (2010)) is now available for open use on the Subaru 8m telescope in Hawaii. This instrument allows simultaneous observations of up to 400 objects within a wide (30' diameter) field of view, within a wavelength range of 0.9-1.8μm. The high multiplicity of this instrument makes it ideal for use in a wide area galaxy redshift survey at $z \sim 1.5$, which will provide constraints of the growth-rate parameter, through measurements of Redshift Space Distortions (RSDs), as well as a statistically significant sample of emission line galaxies for the study of galaxy evolution in what has been termed the redshift desert.

This thesis focuses on the selection of emission line galaxies from available broad-band imaging data for targeting with FMOS with a view to a wide-area redshift survey. I present data from engineering observations with an emphasis on what FMOS can reveal about galaxy evolution, given it's sensitivity and performance, and how this would affect the targeting selection function. Finally, I consider whether FMOS would be suitable for continuum observations of passive galaxies at high redshift, using long-slit observations of members of a possible galaxy cluster at $z \sim 1.9$ as a case study.

In this introduction, I first outline the significance of measurements of Redshift Space Distortions and how FMOS could contribute to the understanding of the nature of Dark Energy. The insights gained into the nature of star-forming galaxies provided by these observations is put into context, with an overview of the current state of knowledge of the Cosmic Star Formation Rate. Integral to this consideration is an understanding of the nature of different star formation rate indicators that have been used to provide

estimates of the cosmic star formation rate at different epochs, and how FMOS is able to extend the results from lower redshift of one particular star-formation tracer, Hα.

1.1 Cosmology

1.1.1 Dark Energy

Observations of Supernovae at different redshifts (Riess et al., 1998; Perlmutter et al., 1999) revealed, through the relationship between their distance (determined given knowledge of the Supernovae's intrinsic brightness) and recession velocity (from the measured redshifts), that the Universe has entered into a stage of accelerated expansion. This effect is not yet fully understood, though it has been parameterised in General Relativity in terms of a cosmological constant. This term has an energy, and hence density associated with it and has been enigmatically labelled Dark Energy. To oppose the natural infall of matter due to gravity, Dark Energy exerts a negative pressure with an equation of state measured to be $w \sim -1$ ($w = \frac{p}{\rho}$, where p denotes pressure, and ρ, density) (Percival et al. (2010) provide a measurement of $w = -0.97 \pm 0.1$ for a constant dark energy equation of state.[1]). Observations of anisotropies within the Cosmic Microwave Background (CMB) from the Wilkinson Microwave Anisotropy Probe (WMAP) also invoke the need for Dark Energy in some form, to reconcile the observations indicating that the geometry of the Universe is very close to flat. This requires the density of the universe to be very close to some critical density, of which matter (baryonic and dark matter) only accounts for around 30%. Recent observations[2] indicate that baryonic matter contributes to $\sim 4\%$ of the make-up of the Universe, dark matter $\sim 22\%$, while the remaining $\sim 74\%$ is attributed to Dark Energy.

Many modified theories of gravity have been put forward that try to explain this phenomenon physically, invoking scalar fields (eg. Wetterich, C. (1995); Amendola (2000)), that couple to matter with an associated energy density, higher order curvature terms (Capozziello et al. (2005), for example) that remove the need for the cosmological constant, and even extra dimensions (eg. Dvali (2000)). However, within the framework of science, these theories must be able to be proven or discounted with observations to give them enough weight to move, or adjust, the framework of the understanding of gravity away from the standard concordance

[1] This measurement is from combining WMAP5 likelihood constraints with measurements of the Baryonic Acoustic Oscillation peak in different redshift slices from the Sloan Digital Sky Survey (SDSS) Data Release 7

[2] http://lambda.gsfc.nasa.gov/product/map/dr3/params/lcdm_sz_lens_wmap5.cfm

cosmology, underpinned by the foundations of General Relativity. This is a huge driving force behind today's observational cosmology, and one way that different models can be distinguished from each other is in how they predict large scale structure to develop.

1.1.2 Redshift Space Distortions

A redshift measurement is the most convenient way to measure of the distance of a galaxy from us. If the movement of the observed galaxy is purely defined by the Hubble flow then the redshift is directly related to the distance. Since the redshift is actually a velocity measurement of the galaxy, then this simple assumption breaks down when large-scale structure affects the flow of matter. First, the galaxy motion is influenced by coherent infall of matter into over-dense regions, then at smaller scales, random, position-independent peculiar motions of galaxies within virilised clusters dominate.

These redshift space distortions are measured by comparing the distances between galaxy pairs, called the two-point correlation function $\xi(S)$. This gives a measurement of the excess probability of a galaxy residing at a given distance with respect to another, compared to a homogeneous distribution of points. Separating the distances into the components parallel to, π, and perpendicular to, σ, the line of sight allow the peculiar motions of galaxies, distorting the distance measurements made using redshifts, to be confined to the parallel component. The angular correlation function, $\xi(\sigma,\pi)$, when plotted then shows the effects of these redshift distortions along one axis only. For true distance measurements, independent of the galaxy motion, the contours of the correlation function would be symmetrical about both axes. The imprint of coherent infall at large scales is observed as a flattening in the π direction (traditionally plotted along the y-axis), whereas on smaller scales the peculiar velocities of galaxies produce an elongation along this axis. These two effects can clearly be seen in Figure 1.1, which is Figure 2 from Peacock et al. (2001) and shows the measured angular correlation function from the 2dF Galaxy Redshift Survey (2dFGRS, Colless et al. (2001)).

Quantifying the extent of the flattening of the angular power spectrum due to this coherent infall provides a measure of the redshift distortion parameter, β, which is related to the growth rate parameter, f according to Equation 1.1, where Ω_m is the matter density parameter, or the ratio of the matter density (dark matter plus baryonic) compared to the critical density needed for a flat Universe; D is proportional to the fractional

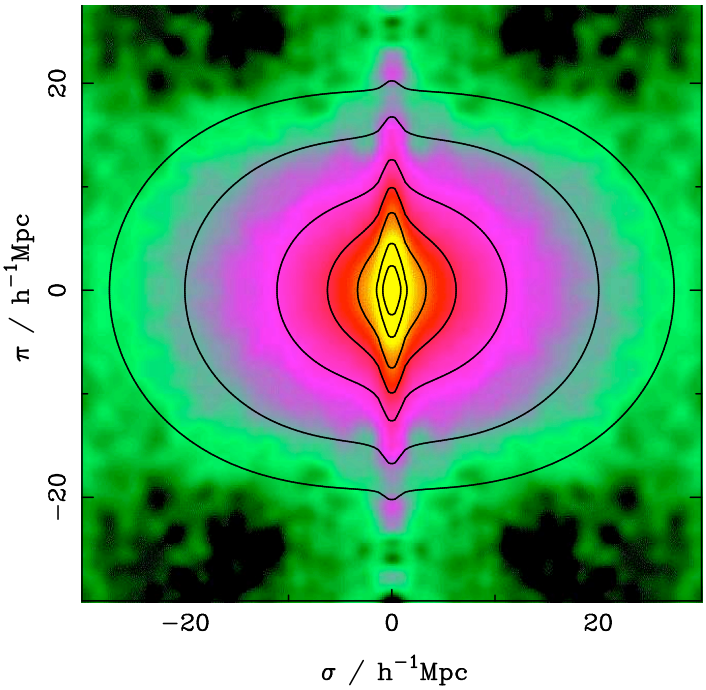

Figure 1.1: Peacock et al. (2001), Figure 2. This displays the measured angular correlation function measured from $\sim 140,000$ galaxy redshifts from the 2dF Galaxy Redshift Survey (2dFGRS, Colless et al. (2001)). The contours show the model predictions with a flattening parameter $\beta = \Omega_m^{0.6}/b = 0.4$ (see text). The flattening and elongation at large and small angular scales, caused by coherent infall and galaxy peculiar motions respectively, can clearly be seen.

over-density; a is the cosmological scale factor and b is the galaxy bias. The galaxy bias describes how galaxies trace the underlying density field and can be measured by comparing the ratio of root-mean-square fluctuations in the galaxy and mass distributions on linear scales and Marinoni et al. (2005) have analysed the galaxy bias up to redshift $z \sim 1.5$ using the VIMOS-VLT Deep Survey (VVDS).

$$f = \frac{d\{lnD\}}{d\{lna\}} \approx \Omega_m^{\gamma} = b\beta \tag{1.1}$$

The relationship between the growth rate parameter and the matter density is the key to revealing the nature of so called dark energy. The parameter, γ is dependent on the cosmological model, and for the cosmological constant model, for which $\Omega_{TOT} = \Omega_m + \Omega_\Lambda = 1$, the predicted value is $\gamma = 0.55$ (Guzzo et al., 2008).

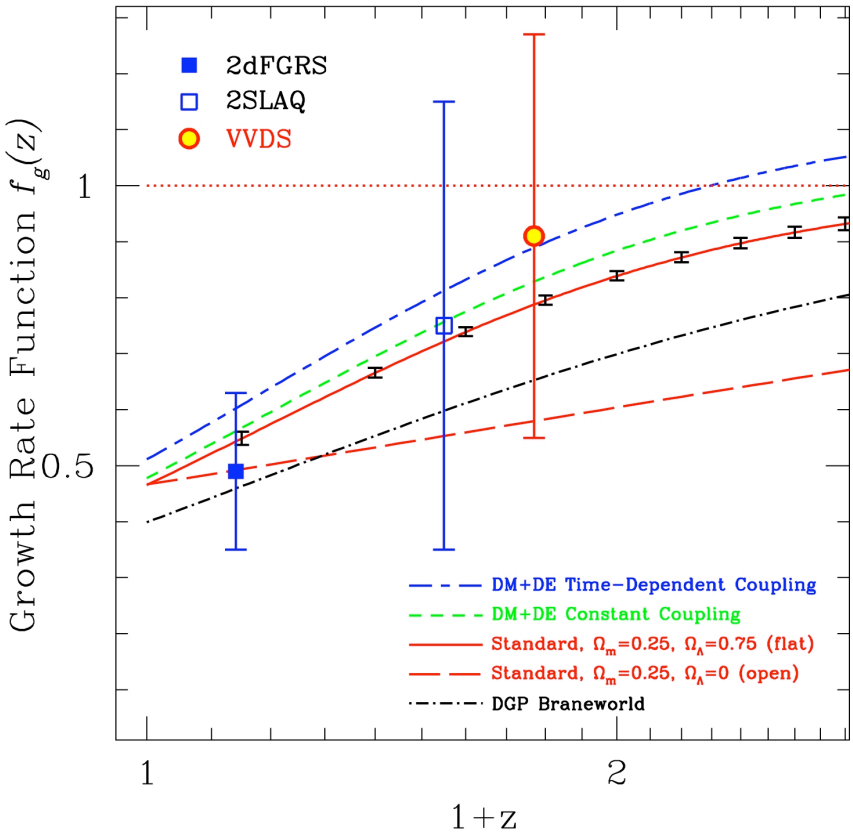

Figure 1.2: Guzzo et al. (2008), Figure 2. This figure shows the measurements of the growth rate parameter from 2dFGRS (Hawkins et al., 2003) (Blue filled squre), the VVDS Wide suvey Guzzo et al. (2008) (Red circle), and 2dF-SDSS LRG and QSO (2SLAQ) survey of luminous red galaxies Ross et al. (2007) (Blue open square). The lines show the predictions made by various models described in the legend. The blue and green dashed curves describe models in which dark energy is coupled to dark matter.

Guzzo et al. (2008) show how measurements of the growth rate parameter can place constraints on cosmological models. Figure 1.2 is Figure 2 from this paper, showing the measurements of the growth rate parameter from redshift space distortions at three different redshifts (see figure caption for details). Overplotted are predictions made by various models, including the standard cosmological constant, flat model (solid red line). What this plot shows is that to accept or reject any of these theories we need to either place tighter constraints on f, by increasing the survey volumes at these points, or push to higher redshifts. This is where FMOS comes in.

FMOS provides high multiplicity of targets over a wide field of view in the near infrared. This makes it perfect for a large area redshift survey. Targeting galaxies at $1.4 < z < 1.7$ places Hα, Hβ and [OIII] within

the observable wavelength range when in low-resolution mode (see below) allowing secure spectroscopic redshift assignments in this range.

1.2 Galaxy Evolution

Large-scale simulations of the growth of structure of dark matter, starting from small primordial fluctuations, growing with time due to gravitational interactions, agree well with observations of large-scale structure. Intuitively the formation of galaxies is expected to follow this hierarchical trend with matter falling into the potential wells of the underlying dark matter. The most massive galaxies are then expected to form at later times from mergers between smaller galaxies. This proved not to be the whole story however, when observations indicated that the rest frame K-band luminosity (so essentially the mass) of starforming galaxies decreases with redshift (Cowie et al., 1996), suggesting that the most luminous, most massive galaxies form their stars earlier than less massive galaxies. Observations of other galaxy properties are also found to follow this "downsizing" trend, with evidence pointing to the downsizing due to the quenching of star formation (Faber et al., 2007; Bundy et al., 2006).

The task of understanding the formation and evolution of galaxies, relative to the hierarchical growth of dark matter structure, requires an understanding of the processes of gas cooling leading to star formation and the resulting feedback. The links between gas cooling, accretion from gas reservoirs onto galaxies and feedback processes such as supernovae and AGN, as well as the relative importance of mergers in the assembly of present day galaxies, all contribute to produce the galaxy population of the present day. Attempts to model galaxy formation due to the growth of density perturbations include using semi-analytical prescriptions (Bower et al., 2006; De Lucia & Blaizot, 2007; Monaco et al., 2007; Menci et al., 2006) or smooth particle hydrodynamics (SPH) (Nagamine et al., 2006; Cen & Ostriker, 2006). Observational studies are integral to the calibration of these models, quantifying the effects of any of the feedback processes, environment dependencies or merger rates.

The high multiplicity and wavelength range of FMOS opens up the possibility of answering questions currently posed about the evolution of galaxies in the redshift $1 < z < 2$ Universe. In particular, the evolution of star formation in this epoch and how it is related to AGN activity can be investigated through the targeting of emission line galaxies. Setting the scene on what questions are currently being asked, and answered,

reveals where FMOS can make an impact, as well as how best to target these galaxies in the first place, as they are the perfect galaxies for the large area redshift survey.

1.2.1 Cosmic Star Formation Rate

Many independent measurements of the global averaged star formation rate (SFR) density agree that the global star-formation rate has been decreasing from redshift $z \sim 1$ to the present day, as first indicated in Lilly et al. (1996). Since then, many different studies, using many different methods for determining SFR, have tried to constrain how star formation in the Universe has evolved from higher redshifts to the present day, when the SFR peaked and how it evolved before this epoch. This has required the use of many different forms of SFR indicators, from UV light emitted directly from the young, hot, short-lived stellar population, to measurements in the far-infrared that measures the emission from dust that has absorbed UV radiation from dusty, star-forming regions and re-processed the radiation, emitting it at longer wavelengths. The main difficulties in compiling these many studies has been to understand, not only the selection effects imposed on each selection, but also in the treatment of obscuration of each measurement, and the fitting of the luminosity functions that are used to integrate properties over the whole population and past the survey detection limits.

Hopkins (2004) compile many different measurements covering the redshift range 1-6, carefully correcting to a consistent cosmology, and taking account of luminosity-dependent obscuration and errors involved in fitting the parametric fits to observed luminosity functions. Their Figure 2 is shown in Figure 1.3, with colour coding described in the caption. The full list of references for the compiled measurements are included in Appendix E, including information of the SFR estimator and redshift of measurements, taken from their Table 2. Figure 1.3 displays the observed increase in SFR at low redshift and indicates that the SFR has started to level by redshift 1 and may be falling between redshift 3-6. The large scatter between measurements made with different estimators obscure the details of the evolution above redshift 1.

Star Formation Rate indicators

Many different tracers of star formation are used to estimate the star formation rate (SFR) in observed galaxies. The driving factors determining which tracers are used are the redshift range of the targets and which tracers are easily observable in that redshift range. The stronger recombination lines, such as Hα are

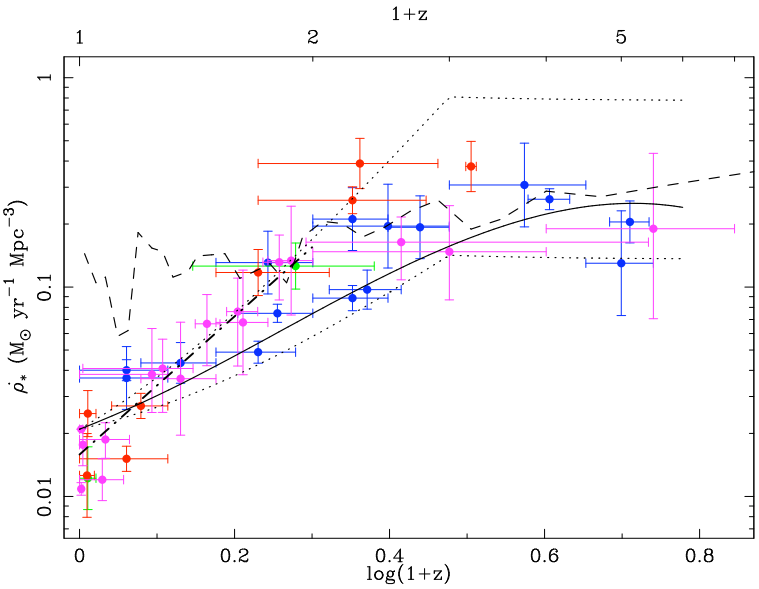

Figure 1.3: Hopkins (2004), Figure 2. This figure shows the Evolution of the cosmic SFR density with redshift, with points colour-coded according to the SFR indicators used in the measurements, as follows. Blue: UV; Green: [OII]; Red: Hα and Hβ; Pink: X-ray, FIR, sub-mm and radio. These are only the measurements for which luminosity-dependent obscuration corrections could be applied.

observable using optical spectroscopy at low redshift but move into the near-infrared above redshift $z \sim 1$. Some forbidden lines (eg. [OII]) are observable to slightly higher redshifts. All these tracers have one factor in common, and that is that they trace the light emitted from young, hot, short-lived stars, either directly or indirectly. The different tracers of star formation are summarised in Table 1.1, with a description of why they are useful as tracers of star formation, as well as some of the limitations associated with them.

Tracer	Rationale	Limitations
UV continuum	Direct tracer of ionising radiation emitted from young, short-lived stellar populations	Extinction from dust
Recombination Lines (eg. Hα)	Emission lines produced in nuclear HII regions from gas excited by radiation shortwards of the Lyman limit	Extinction from dust, stellar absorption at same wavelengths confuse the issue eg. for Hβ
Forbidden Lines (eg. [OII])	Also excited by high-energy UV radiation	Not directly coupled to the ionising radiation, line strengths more dependent on abundance and ionisation state of the gas.
Far-Infrared	Dust heated directly by ionising radiation and re-emitted in the Far-Infrared	Dependent on optical depth of dust.
Radio	Thermal radiation from HII regions; FIR:Radio correlation	Dependent on the Far-Infrared being a good tracer of SFR.

Table 1.1: Different Star Formation Rate tracers (SFR)

Kennicutt (1998) compiled a consistent set of SFR calibrations for different star-formation indicators which are widely used. In particular, the calibration for deriving the SFR from the observed Hα flux (Equation 1.2) is used in this thesis.

$$SFR(M_{\odot}yr^{-1} = 7.9x10^{-49}L(H\alpha)(ergs\ s^{-1}) \tag{1.2}$$

Each tracer introduces it's own bias into the SFR measurement and calibrating the measurements to provide SFRs that are consistent for different tracers is an active area of research. As can be seen from Figure 1.3, these factors produce large amounts of scatter between the global SFR estimates. One way of addressing this issue is to use one consistent SFR tracer over a large redshift range, and Hα is a viable option for this task. Measurements above $z \sim 1$ made with this tracer have previously been from small samples via narrow-band and spectroscopic surveys, though this is now changing, with the High-Z Emission Line Survey (HiZELS, see below).

With a large redshift survey targeting emission line galaxies for measurements of RSDs, FMOS can provide a large sample of star-forming galaxies, with Hα and Hβ measurements that allow for accurate extinction corrections on a source-by-source basis.

Understanding how star formation is affected by environment and merger rate, for example, and how these different factors vary with redshift will allow us to gain an understanding of the reason for the rapid decline in SFR since redshift $z \sim 1$, as well as when and how galaxies have formed and evolved into the populations we are able to observe. The large sample afforded by FMOS should help to address some of these questions at $z \sim 1.5$. HiZELS is already addressing them successfully at $z \sim 1$ and $z \sim 2.2$.

HiZELS

The High-Z Emission Line Survey (HiZELS) is a narrow-band imaging survey using WFCAM on UKIRT (Best et al., 2010). The survey is to cover a total of 6.2 square degrees over six different fields (including the UDS) using three narrow band filters with central wavelengths at 1.211, 1.619 and 2.121μm (NB_J,NB_H,H_2(S1)), which are situated within the J, H and K-bands respectively. These filters are used to select Hα emitters at redshifts of $z \sim 0.84, 1.47, 2.23$ from the narrow-band:broad-band colours. The exten-

sive multi-wavelength data available in the observed fields are also used to filter out narrow-band emitters not associated with Hα. This survey provides an Hα flux-limited survey of Hα emitters down to a limit of $1\text{x}10^{-16}$ erg s^{-1} cm^{-2}.

The sample selected from the NB$_J$ filter currently provides the largest sample of Hα emitters out of the three selections. They are the most fully characterised, with high quality photometric redshifts and spectroscopic data available in the COSMOS field to test the robustness of the selection from the narrow-band excess (Sobral et al., 2009), (S09). Geach et al. (2008) present results from the H$_2$(S1) selected sample and comparison of the measured Hα luminosity functions at $z \sim 0.84$ and $z \sim 2.2$ shows strong evolution in the shape of the luminosity function, with the counts of the more luminous Hα emitters decreasing from $z \sim 2-1$ (S09).

Examining the details of the luminosity function reveals that mergers dominate the bright end of the luminosity function in the NB$_J$ sample, whereas the disk population dominates the fainter end. Comparing to the Hα luminosity function measured at lower redshifts, it seems that the evolution in the shape of the luminosity function, parameterised in terms of a Schechter function (Equation 1.3), is dominated by evolution in Φ^* at low redshifts and by L^* at high redshifts. These two parameters determine the overall normalisation of the function and the characteristic luminosity, above which the spatial density drops sharply, respectively. The other parameter in the Schechter function, α, sets the faint end slope of the luminosity function.

$$\Phi(L) = \left(\frac{\Phi^*}{L^*}\right)\left(\frac{L}{L^*}\right)^{\alpha} exp\left(-\frac{L}{L^*}\right) \tag{1.3}$$

S09 take this to indicate that at higher redshifts ($z \gtrsim 1$), evolution in the rate of mergers and hence the merger-induced star-formation activity starts to dominate. The higher luminosity limit in the H$_2$(S1) filter selected sample (due to the objects being at higher redshift) means that the faint end slope is less well constrained by this Hα luminosity function. Including the sample from NB$_H$ should bridge the gap, indicating how the faint end slope in the luminosity function is varying between $z \sim 0.84-2.2$.

This large sample of star-forming galaxies detected within a thin redshift slice provide the opportunity to examine how SFR varies with mass and environment (Sobral et al., 2010b) (S10), as well as the clustering properties of the population (Sobral et al., 2010a) (both these studies focus on the NB$_J$ selected sample).

S10 shows that star formation mostly occurs in the field, and that any star-forming galaxies in denser environments are associated with merger activity. Stellar mass is the primary predictor of star-formation activity at $z \sim 1$, with sSFR decreasing with increasing mass, but the environment, while initially enhancing the median SFR of (lower-mass) star-forming galaxies is ultimately responsible for suppressing star-formation activity in all galaxies in group and cluster environments.

Extinction properties of these sources have been examined in Garn et al. (2010) by comparing $24\mu m$ SFRs with the Hα luminosity using the calibration of Rieke et al. (2009) for converting $24\mu m$ flux densities to SFRs. Garn et al. (2010) find a positive correlation between extinction and SFR, as seen in galaxies at $z \sim 0$. They conclude that there is no evidence in a change in dust properties over this redshift range. Further work, using a sample of $\sim 90,000$ galaxies from the Sloan Digital Sky Survey (SDSS) Data Release 7 shows that this correlation is fundamentally caused by the extinction properties of a galaxy being related to the mass of the galaxy (Garn & Best, 2010).

Spectroscopic targeting of the NB_J sample has been integral in determining the rate of contamination from other emission lines in the selection, but also in determining the AGN contamination. By spectroscopically targeting HiZELS NB_H selected sources with FMOS, not only can the extinction properties of star-forming galaxies be examined at $z \sim 1.5$, using the flux ratio of Hα to Hβ which are both visible using low-resolution mode, but the AGN fraction of the selection can be determined using the BPT diagnostic (Baldwin et al., 1981). This uses flux ratios of [NII]:Hα and [OIII]:Hβ, lines close to each other in wavelength and so relatively unaffected by differential extinction, to determine the source of ionising radiation. Narrow-line AGN occupy a separate region of the plot to the tightly located star-forming sequence, with a continuous distribution of objects with contributions from both factors joining the two regions.

1.2.2 Clustering

Galaxy clusters trace the densest and most massive dark matter halos and as such can provide constraints for structure formation and cosmology (Gladders et al., 2007). The observed velocities of galaxies within clusters are too high for them to remain gravitationally bound without the presence of dark matter, and observations of hot intra-cluster gas emitting bremsstrahlung and atomic line emission in form of X-rays, do not account for the amount of matter required to keep these structures bound. The inference is that they

reside in massive dark matter halos and as such they provide evidence for dark matter.

Wide area broad-band imaging data can be used to detect clusters, with one of the most successful methods being that of the red sequence method (Gladders & Yee, 2000). The red sequence method uses the observational result that all clusters seem to contain a population of early-type galaxies, called the red-sequence, that lie along a linear colour-magnitude relation, and were formed at high redshift. Kodama et al. (1998), for example, investigate the evolution in the colour-magnitude relation for early-type galaxies in clusters in the redshift range $0.31 < z < 1.27$. Their results indicate a redshift of formation of the early-type galaxies to be $z_f > 2-4$. The red sequence method then finds over-densities of red sources from 2-band colours, with the bands chosen to sample the 4000Å break. This method was used to detect ~ 1000 clusters over $0.35 < z < 0.95$ in the Red-sequence Cluster Survey (RCS, Gladders et al. (2007); Yee et al. (2007).

Not only do galaxy clusters provide constraints on large-scale structure formation and evolution, but they provide valuable targets for studies of galaxy evolution and how it is affected by environment. There is a relation between colour and environment, with red galaxies predominantly found in high density regions and blue galaxies predominantly found in the field (Dressler, 1980). Large-scale redshift surveys have enabled this color-density relation to be investigated out to $z \sim 1.35$ and its evolution traced (Cooper et al., 2006, 2007; Cucciati et al., 2006). Investigating the evolution of this relation indicates the importance of the local environment on the evolution of galaxies. Cooper et al. (2007) found that the color-density relation observed locally was in place at redshift one, though the relation was shown to weaken with increasing redshift. The weakening of the relation suggests that star formation is preferentially quenched in over-dense regions rather than the local overdensity determining the colour of galaxies when they form (the "nature vs. nuture" question, with nurture found to be the dominant factor). This is most likely due to the disruption of galaxies by mergers or ram-pressure stripping of dust. This relationship is partly weakened at high redshifts by the presence of a population of massive blue galaxies in higher density regions with no counterpart at low redshift (Cooper et al., 2006). This relationship can be probed directly by targeting objects at different positions relative to a cluster core, where the density increases from that of the field to the highest densities at the core, Kodama et al. (2001) is one such study.

JKCS041

JKCS 041 is a possible galaxy cluster in the CFHTLS Deep-1 field. It's detection is reported in Andreon et al. (2009) with a photometric redshift estimate of $z_{phot} \sim 1.9$. With the current highest redshift cluster detection (at the time of writing) at 1.753 (Henry et al., 2010), derived from the spectroscopic redshift of the brightest galaxy member, JKCS 041 would be the highest redshift cluster detected to date, if the photometric redshift estimate is accurate.

The cluster was detected as an over-density of sources of similar colour, from the J- and K-band photometry released in the UKIDSS Early Data Release (Dye et al., 2006) using a version of the red sequence method (Gladders & Yee, 2000). This colour is consistent with the presence of the 4000Å break falling within the region of the the J- and K-bands, and the over-density of sources in the colour space indicates that there are more objects than usual in a small redshift range.

There is an X-ray detection at the position of the observed over-density and is shown in blue in Figure 6.1. Andreon et al. (2009) find a best-fitting spectral model to the observed X-ray spectrum, with a temperature of $7.6^{+5.3}_{-3.3}$keV for a plasma model with redshift fixed at 1.9. This temperature, in turn, provides an estimate of $R_{500} = 0.52$Mpc (the radius within which the density is 500 times the critical density at the cluster redshift), and a mass within this radius $M_{500} = 2.9^{+3.8}_{-2.4}$ x $10^{14} M_{\odot}$. These estimates all depend on the X-ray source being associated with the observed over-density and being situated at redshift 1.9.

1.3 UKIDSS-UDS

The catalogue created for this thesis to test selection mechanisms for emission line galaxies, and later for targeting with FMOS, is taken from the UKIDSS-UDS field. The United Kingdom Infrared Telescope Deep Sky Survey (UKIDSS)[3] is a set of five large near-infrared surveys, of which the Ultra Deep Survey (UDS) is the deepest tier. This patch of sky is covered in the optical by Subaru, as part of the Subaru/XMM-Newton Deep Sky Survey (SXDS) (Furusawa et al., 2008) and the mid infrared with the Spitzer SWIRE survey (Surace et al., 2005) and the deeper spUDS (Spitzer UDS) survey (Dunlop et al., 2007). It covers approximately a square degree in area and given the depths reached in the near infrared and optical, as well

[3]The UKIDSS project is defined in Lawrence et al. (2007). UKIDSS uses the UKIRT Wide Field Camera (WFCAM; Casali et al. (2007)) and a photometric system described in Hewett et al. (2006). The pipeline processing and science archive are described in Irwin et al (2008) and Hambly et al. (2008).

as the extensive broad-band photometric coverage, provides a perfect data set for testing different selection mechanisms with FMOS. The data in this thesis is taken from the Third Data Release Plus. The multi-wavelength imaging data available in this field is summarised in more detail at the start of Chapter 2.

1.4 FMOS

1.4.1 Near-Infrared Spectroscopy

Until fairly recently the redshift range $1.4 < z < 2.5$ has eluded spectroscopic investigation. It is at redshift $\sim$ 1.4 that the last of the nebular emission lines, [OII] has been shifted into the near-infrared where the quantum efficiency of optical CCD detectors is unable to reach, and the sky background increases in brightness. Termed the 'redshift desert', since there were no features observable in the optical to constrain spectroscopic redshifts, there is a lot of catching-up to be done to bring the understanding of galaxy evolution up to the quality available at lower redshifts, and to bridge the gap between low-redshift studies and higher redshift populations, for which features in the rest-frame UV have shifted into the optical.

Spectroscopy in the Near-Infrared is made difficult by the bright atmospheric emission lines that dominate the sky background spectrum. In fibre-fed systems specifically, the sky subtraction leaves systematic sky-line residuals in the absence of advanced methods of sky subtraction (such as PCA fitting).

1.4.2 The Instrument

The instrument consists of three components; the Prime focus unit optimised for the Infrared; the fibre positioning system, called Echidna; and two cooled infrared spectrographs, IRS1 and IRS2.

Four hundred fibres collect light from separate objects over a 30' diameter field of view, at the F/2 prime focus of the 8m Subaru telescope. Two hundred fibres each are fed into two separate spectrographs that have identical light paths (shown in Figure 1.4). These spectrographs employ a method to suppress the OH emission lines that dominate the sky background spectrum in the near-infrared, and so increase the sensitivity of the spectra. This is achieved using the OH suppression mirror, onto which the dispersed light is imaged at high resolution. This mirror is etched at the positions of the OH emission lines thereby removing them from the spectrum. The light is then either passed through another grating to degrade the resolution to

∼500 so that the entire spectrum can be imaged onto the detector, or sections of the spectra can be imaged at a higher resolution (R∼3000). At high resolution only a third of the whole wavelength range can be imaged onto the detector at any one time.

The fibres are configured by Echidna, with the user supplying a list of targets that the fibre positioning software assigns fibres to, and produces a file to be supplied to Echidna for field configuration. The field is positioned by allocating guide fibre bundles (7 available to each side of the FMOS field of view) to chosen guide stars, and adjustments are made by choosing coordinate calibration stars throughout the field that are imaged onto a CCD camera in the Echidna Focal Plane Imager. For more details, see Chapter 4, section 4.2.2.

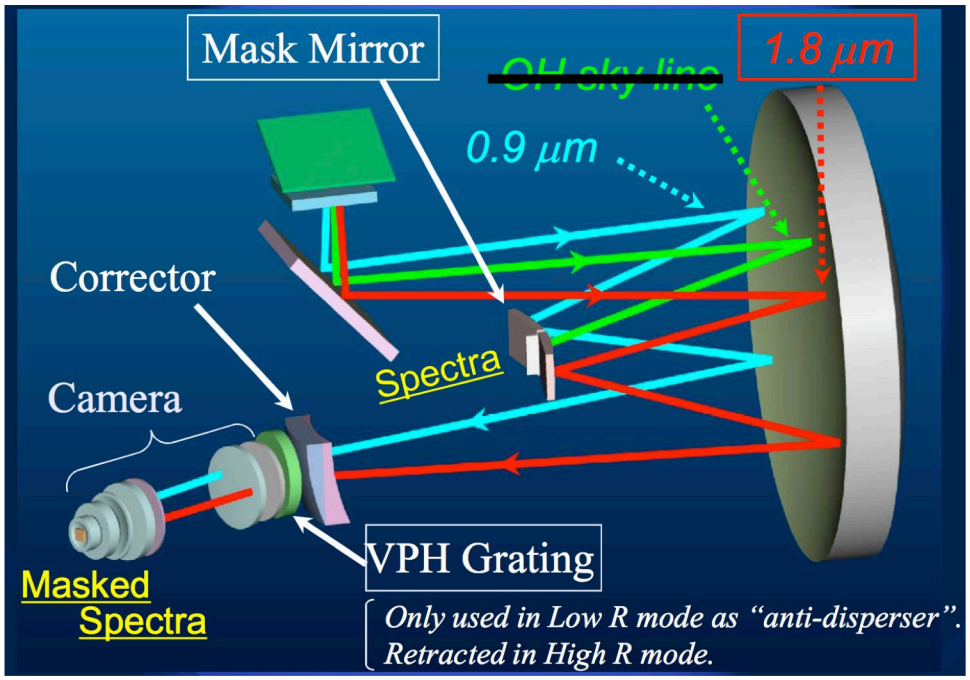

Figure 1.4: The optical layout of a spectrograph. [1]

1.4.3 Science

Further to the areas of science already touched on in this chapter at high redshift (measurement of RSDs to constrain the growth rate parameter, targeting of star-forming galaxies at $z \sim 1.5$ to obtain measurements of Hα and Hβ to provide extinction corrected SFR estimates, and true AGN distinction) FMOS provides opportunities for studies of objects closer to home. The wavelength coverage of FMOS is well suited to

1. Image Credit - © STFC

studying dusty environments with high excitation lines, such as high mass star forming regions in our own Galaxy. Analysis of these regions is important to understand the effect of environment on star formation. FMOS can also be able to perform follow-up spectroscopy on Brown Dwarfs, enabling the determination of effective temperatures, spectral types and surface gravity measurements (Lucas & Bandyopadhyay, 2004).

1.4.4 Commissioning

In late 2007, all of the mechanical components were shipped to Hawaii, assembled and mounted on the telescope. Since May 2008, engineering observations have been carried out to check the basic performance of the instrument. It was in two of these engineering runs, in October 2009 and December 2009 that the science verification data, presented in Chapter 5 was taken in the UDS.

Kimura et al. (2010) summarise the basic instrument parameters as follows.

- The configuration accuracy of the fibres by Echidna is less than 0.15", much smaller than the projected fibre diameter of 1.2". The accuracy of the auto-guiding using guide-fibre bundles is typically less than 0.18".
- The total system efficiency is measured to be $7 \pm 3\%$ in the H-band, slightly lower than the measurements using an image of a defocused bright star, indicating that the losses occurring at the input surfaces of the fibres are not negligible.
- The observations made with IRS1 indicate that the noise background is approaching the limit of the detector, showing that the thermal background is being effectively blocked. IRS2 has shown a high thermal background due to a sub-optimal blocking filter. At the time of writing this is due to be fixed, though the data taken with IRS2 in October 2009 and December 2009 were subject to this high thermal backgound.
- The limiting magnitudes for an hour long exposure with S/N=5 per pixel are J=20.1 mag and H=19.8 mag in low-resolution mode. The emission line flux of 1 x 10^{-16} erg cm^{-2} s^{-1} is detected with a S/N=5 in both J and H.

Observations in October 2009 revealed that the fibre configuration is not stable for long periods, due to a misalignment between the FMOS wide-field corrector and the telescope axis. This effect is now taken into

account by re-configuring the fibres after every 30 minutes of exposure.

1.5 Thesis Layout

In Chapter 2, I describe the steps used to produce a band-merged catalogue of objects in the UDS field with imaging data from Subaru in the optical, UKIDSS in the near-infrared and Spitzer IRAC (InfraRed Array Camera) bands in the mid-infrared.

Chapter 3 touches on the possible selection methods of emission-line galaxies for an RSD survey using broad-band imaging data. Chapter 4 introduces my reduction pipeline used to reduce engineering data, obtained with FMOS in October and December 2009 of objects in the UDS field. In Chapter 5 the performance of the instrument and implications for the target selection are investigated using the commissioning data. In Chapter 6, observations of possible cluster member galaxies of JKCS 041 are presented, where we target the 4000Å break to determine the cluster redshift, using ISAAC long-slit spectroscopy. In Chapters 7 and 8 you can find my Conclusions and details of further work.

Chapter 2

UKIDSS Ultra Deep Field

2.1 Introduction

In this chapter, the multi-wavelength imaging data available in the UDS field is described, as well as the steps used to produce a K-band selected, band-merged catalogue. This includes the method used to deal with the problem of source confusion in the deep Spitzer spUDS images. This catalogue is used in Chapter Three when determining photometric redshifts for investigating different methods for selection of objects at $1.4 < z < 1.7$.

Throughout this chapter, unless otherwise stated, magnitudes are in AB, BCD frames are the Basic Calibrated Data frames available from the Spitzer Science archive and CBCD frames are Calibrated BCD frames in which many artifacts have been mitigated. Ch1 and ch2 frames refer to $3.6\mu m$ and $4.5\mu m$ Spitzer IRAC frames, respectively.

2.2 Multi-Wavelength Imaging Data

2.2.1 Subaru

The optical data is taken from the Subaru/XMM-Newton Deep Sky Survey (SXDS) which provides images in the B,V,R,i, and z bands. Details of the source catalogues and image products can be found in Furusawa et al. (2008). The survey consists of five pointings covering 34' x 27' field of view, overlapping with the UKIDSS, UDS field. The astrometry is calibrated using $\sim$200 stars from the 2MASS point source

catalogues. The RMS uncertainty of the coordinates across the field of view are in the order of 0.2". The photometry is calibrated to give AB magnitudes using the magnitude zero points in table 2, Furusawa et al. (2008). The zero points are measured from overlapping, previously calibrated data. The RMS uncertainty in the zero points is quoted as 0.03 - 0.05 mag.

2.2.2 UKIDSS

J, H and K band imaging used in the photometry are from the United Kingdom Infrared Telescope Infrared Deep Sky Survey (UKIDSS). This is actually a set of five large near-infrared surveys, of which this thesis is concerned with the Ultra-Deep Survey (UDS), Third Data Release Plus (DR3+). Details of previous UKIDSS data releases can be found in Dye et al. (2006) (Early Data Release); Warren et al. (2007b) (First Data Release); Warren et al. (2007a) (Second Data Release). Hewett et al. (2006) details the photometric system used by UKIRT. The Third Data Release includes H-band imaging for the first time.

The UKIDSS astrometry and photometry is calibrated using 2MASS (Two Micron All Sky Survey) stars in the field. The error in Ra and Dec coordinates estimated from internal consistency between multiply imaged stars is approximately 50 mas. The photometry is calibrated such that the photometric zero points used will reproduce Vega magnitudes of 2MASS stars given a suitable aperture correction. The specified absolute systematic accuracy is 0.02mag in each band (Dye et al., 2006). The zeropoint offsets used to convert UKIDSS Vega magnitudes to AB magnitudes are from Hewett et al. (2006).

The source-merged catalogue available from the WFCAM science archive[1] for the UDS data is K-band selected, as the K-band image is deeper for most galaxy colors. The UDS frames were not stacked by the UKIDSS pipeline, but were fully stacked and mosaiced before source extraction. The UDS source extraction uses SExtractor (Bertin, 2006) as the standard UKIDSS pipeline software was found not to produce optimal source catalogues from the data (Foucaud et al., 2007).

For the band-merged catalogue produced here, the source extraction was re-run from the K-band image as described in Section 2.3.1. The DR3+ image products used to produce the catalogues consist of stacked, mosaiced images with approximate seeing of ~ 0.7", and 5σ depths of: J$\sim$22.9, H$\sim$21.5 and K$\sim$21.8 in Vega magnitudes.

[1] http://surveys.roe.ac.uk/wsa/

2.2.3 Spitzer

SWIRE

The SWIRE (Spitzer Wide-area InfraRed Extragalactic survey) (Surace et al., 2005) XMM-LSS field also overlaps with the UDS field, providing near-infrared IRAC data at 3.6μm, 4.5μm, 5.8μm and 8.0μm for most of the UDS sources. Astrometric calibration is performed by first using the known pointing history of the telescope, then requiring the observed image data to coincide with 2MASS astrometry. The accuracy of the registration of any given star is accurate to $\sim$0.3" . The photometry is calibrated using selected calibration stars within the field and the point source photometry is calibrated to an accuracy of 3%. The photometric calibration is performed on the BCD frames within an aperture of 10 native pixel radius (12"), with a background annulus with inner and outer radii of 12 and 20 pixels. The wings of the point spread function (PSF) of the instrument extend into the background annulus and as such, a small amount of the source flux is being subtracted in the background subtraction. This effect is calibrated for this particular aperture but when using other sized apertures a correction has to be applied to account for the diffrerences. The calibrated photometric zeropoints are thus correct for apertures with 12" diameter (Reach et al., 2005).

Performing aperture photometry on SWIRE IRAC image products is complicated by the required corrections due to the IRAC flat field. This has been derived from the high surface brightness zodiacal background, which peaks redward of the filters, unlike most of the bluer sources of interest. These corrections are array-location-dependent and have to be applied to the original BCD images before mosaicing, or a correction mosaic has to be generated. This is the largest source of error in performing point source photometry on IRAC image mosaics, with peak-to-peak corrections of order 10 to 20% (Handbook, 2010).

SpUDS

The UDS has also been targeted with Spitzer to much deeper limiting magnitudes with spUDS ($\sim$23(AB) in 3.6μm, Dunlop et al. (2007)). This presents the issue of confusion in the deepest two bands (3.6 and 4.5μm) which is discussed in more detail in Section 2.4. The 3.6 and 4.5μm images are used here, rather than the SWIRE data, as they provide the opportunity to probe how deep you would need to be in the IRAC bands for them to be of use for target selection with FMOS.

The warm stage of the Spitzer mission is underway at the time of writing, and data is still being taken

with these two bands, allowing the possibility to cover new fields with Spitzer coverage.

The full broad-band coverage in the UDS is summarised in Figure 3.5 which shows the profiles of each of the filter transmission filters.

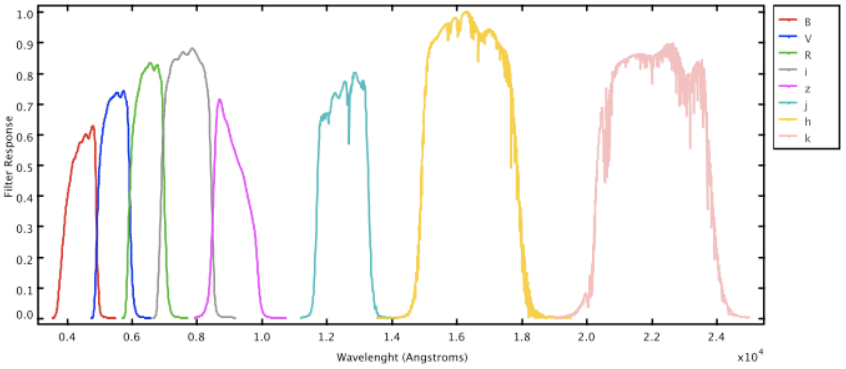

(a)

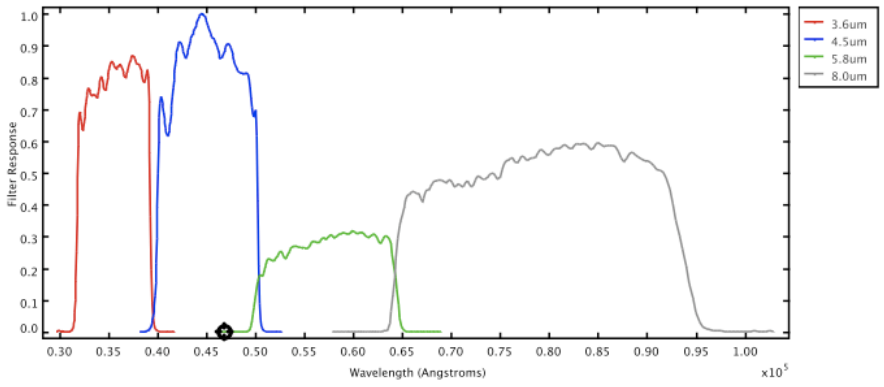

(b)

Figure 2.1: The filter transmission curves in the optical to mid infrared, with Subaru and WFCAM filters plotted in panel (a) and the Spitzer IRAC filters plotted in panel (b)

2.3 Optical to Near-Infrared photometry

The catalogue is selected from the K-band UDS image. This process starts with source extraction using SExtractor. There are catalogues available from the WFCAM science archive that have been selected from this image[2] (see Foucaud et al. (2007) for details of the Early Data Release (EDR) UDS catalogue) but these

[2]http://surveys.roe.ac.uk/wsa/

were not used for two reasons. First, when matching photometry between different bands with the final goal being to determine photometric redshifts, the photometric apertures, seeing and zeropoints must be matched as accurately as possible. This is not possible when matching between catalogues with differences in astrometry and deblending thresholds. The aim with this photometry was to extract the sources from all the optical and near-infrared images using SExtractor (Source Extractor) (Bertin, 2006) in dual image mode. This means that the objects are detected and object profiles characterised in one image (the K-band image in this case) and then the objects are extracted from the other images at the same positions, with the photometric apertures sampling the same physical regions of the objects.

The second reason is that the method used here to perform photometry on the confusion-limited Spitzer IRAC images requires priors in position and shape of the objects from a shorter-wavelength, higher resolution image. The initial parameters used to make these priors come from the SExtractor output from the K-band image.

2.3.1 K-band selected catalogue

Source Extraction

Sources are first detected and characterised using SExtractor (Bertin, 2006). This package is designed to detect objects and perform photometry for large-scale galaxy surveys.

SExtractor first calculates the background level in the image, then filters the image to enable the preferential detection of sources rather than noise. This filtered, background-subtracted image is used to isolate connected groups of pixels that lie above a detection threshold that is set by the user. Once groups of connected pixels are identified they are deblended to assign the pixels to their appropriate source if multiple sources are overlapping within the group. The aggressiveness of the deblending can be tuned by the user by setting various thresholds that in effect determine how much flux a secondary peak needs to contain before it is considered a separate source (DEBLEND_MINCONT) and how finely the profile of the pixel group is sampled (DEBLEND_NTHRESH).

The filter greatly affects the sensitivity and deblending characteristics of the resulting catalogue. A number of different filters are supplied with SExtractor, the results of which were compared, by eye from the segmentation images (images that highlight groups of pixels and assign them a flag according to which

object they are assigned to), and to the source catalogue available from the WFCAM science archive. The filter chosen was the gauss_1.5_3x3.conv filter which was found to suitably filter the noise.

The performance of the detection depends strongly on how accurately the noise properties of the image are characterised. For images that have been made up from stacked, jittered frames the noise properties can vary across the image according to change in coverage and differences in illumination across the detector. These are taken into account by weighting the extraction using the confidence images provided by the observatory.

Characterising the catalogue

The limiting magnitude of the K-band image was determined by placing 2" diameter apertures at random places over the image. Any apertures containing sources were discounted using the segmentation image (see above for a description). The standard deviation of the background counts gives the true error in determining the background flux within this sized aperture whatever the structure in the background noise and, at a value of ~ 460 gives a 5σ, point-source limiting magnitude of 23.5 (AB) (within the 2" aperture, or $\sim$23.8 (AB) total magnitude).

To determine the completeness of the catalogue, artificial point sources were added to the original image using the IRAF task ADDSTAR before re-running the source extraction. This task adds representations of the PSF, modelled with the DAOPHOT task PSF, to random points within the image. One thousand stars were added with magnitudes distributed randomly between 11 and 25. Any sources added to the position of a previously detected object or a masked position were discounted from further analysis. The fraction of objects detected was then determined by running the source extraction on the image and the catalogue matched to the original star catalogue. This was repeated 10 times and figure 2.2 shows the histogram of sources added, and that of un-detected sources. At a magnitude of 24.1 ± 0.1 (AB), 50% of the point sources are recovered (dashed line on the plot).

2.3.2 Photometry

There are a few different options available when performing photometry in different bands with the aim of accurate object colours and some of these options are listed below:

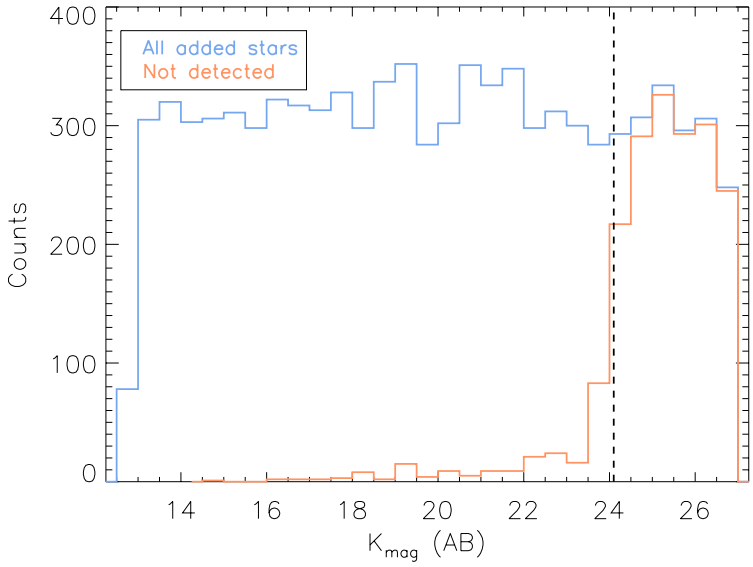

Figure 2.2: The magnitude range of artificial stars added to the image (blue histogram) with the distribution in magnitude of undetected stars (orange histogram). The dashed line shows the 50% point source completeness limit at 24.1 magnitudes (AB).

- Perform aperture photometry in a large enough aperture to encompass all of the object flux. *This is not optimal since the use of a larger aperture, encompassing low signal to noise regions of the object, will produce noisier flux estimates.*

- Perform photometry in a smaller aperture applying a point source aperture correction to produce an estimate of the total flux. *Convenient if the objects of interest are unresolved or only partially resolved but the aperture correction assumes that the source profile follows that of a point source.*

- Match the point spread function (PSF) of all images and perform aperture photometry in smaller aperture without an aperture correction. *A small aperture may mean that you are only sampling part of the object profile but the matched PSF should ensure that you are sampling the same physical region, or the same fraction of the object's flux in all bands.*

- Employ SExtractor's MAG_BEST option which supplies an estimate of the object's total flux.

In this case the third option was chosen. The optical and near-infrared images are all degraded to 1" seeing to match the image PSFs before performing photometry in a 2" diameter aperture. The small aperture size ensures high signal to noise flux estimates and negligible contamination from neighboring objects. This

method was chosen since the images are all very deep and fairly crowded. Within this sized aperture, most of the objects cannot be assumed to be point sources and so PSF matching was considered a more accurate method for correcting differences in seeing between the images than applying an aperture correction.

To use SExtractor in dual image mode, the SXDS images must first be resampled into the pixel grid of the K-band UDS image. This requires accurate matching of astrometry.

Astrometry

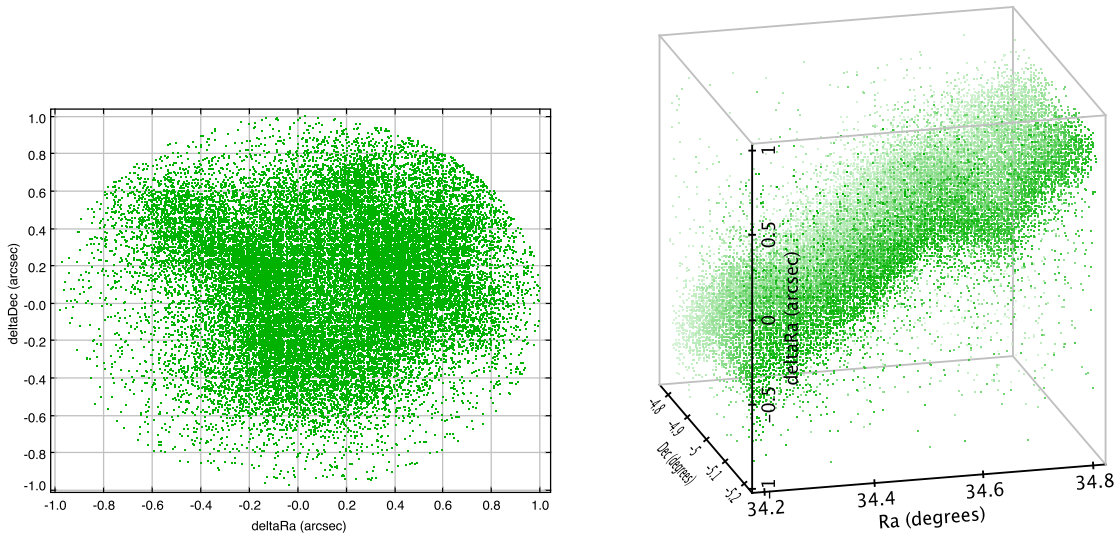

(a) (b)

Figure 2.3: The differences in astrometry between the central Subaru pointing and the UKIDSS K-band image. Found by matching catalogues obtained from the two images. (a) Shows that there are systematic differences in right ascension and declination (Ra and Dec) while (b) shows how the difference in Ra varies across the image.

There are systematic differences between the Subaru and UKIDSS image astrometry across the field. This is shown in Figure 2.3, where this figure is produced by matching a catalogue extracted directly from the Subaru B-band central image with the K-band catalogue. It was found that systematic offsets were found between the separate SXDS pointings, with the central pointing producing the largest offsets, shown above. As such, the UKIDSS astrometric frame is chosen as the most stable and used through the rest of the detection.

These differences in astrometry were measured and modeled by Chris Simpson[3] and have been modeled similarly here, as follows. For each source, the offset in that region of the image is calculated from an average of all offsets within a 5 arcminute radius. This smoothes over any mis-matched objects or differences in deblending thresholds between the two catalogues. For each object, the predicted position within the UKIDSS astrometric frame can then be determined.

Before correcting the astrometric errors, the SXDS images are resampled into the UDS pixel grid and astrometric frame using the IDL procedure HASTROM, a procedure that registers images to the same astrometric frame, as defined in the image headers. This procedure does not match the header astrometry perfectly so these differences are modelled as above. The differences in astrometry between the original SXDS images and those introduced by HASTROM can then be removed by using the modelled astrometric shifts at the object positions as tie points in the IDL procedure TRI_WARP. The results of this resampling and warping are illustrated in Figure 2.3.

PSF matching

The different SXDS pointings are each convolved to the same PSF so that the FWHM is matched in each band for each pointing but each pointing has a different PSF. The J, H and K band images also all have slightly different seeing. To match the seeing in all of the images, they are all degraded to 1" seeing. For the SXDS images, the original model PSFs are modelled as gaussian with FWHM as given in Furusawa et al. (2008). The PSF of each of the UDS images are modelled using the IRAF DAOPHOT package. The kernel required to convolve the images to the same PSF was determined by using the IRAF task PSFMATCH using a model gaussian PSF with FWHM 1" as the reference PSF.

Overlapping regions between different SXDS pointings allows this correction to be tested within the chosen 2" diameter aperture for the photometry. Figure 2.4 shows clear systematic differences between the photometry in the images before matching the PSFs for images with matched astrometry (orange histogram), while after convolution to 1" seeing any systematic offset is negligible (blue histogram).

[3]http://www.astro.ljmu.ac.uk/ cjs/SXDS/uds/matching.html

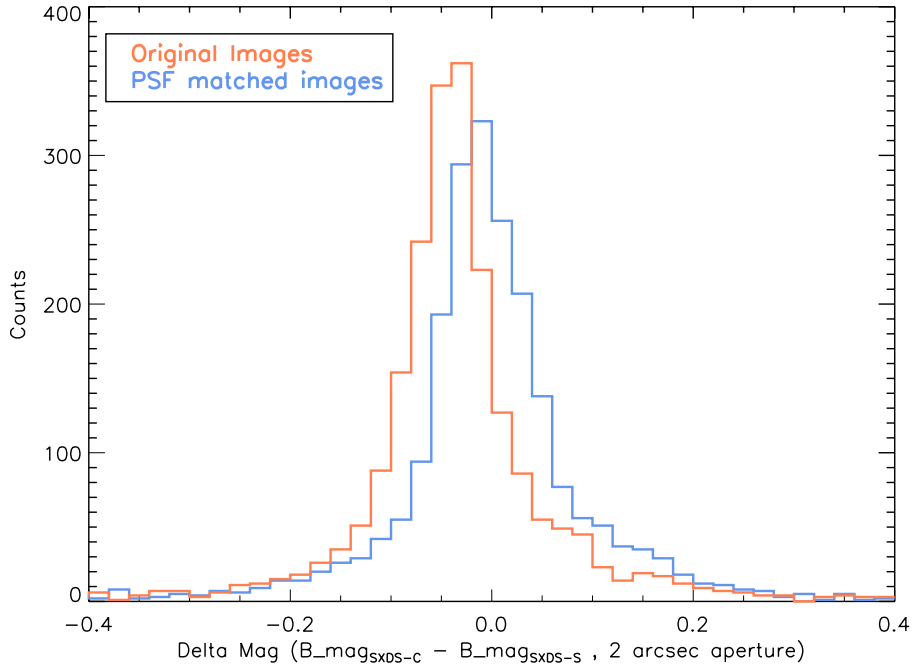

Figure 2.4: Differences in object magnitude from the SXDS B-band Central and Southern pointings. The orange histogram shows the photometry differences between objects detected in the overlapping region of the central and southern pointings before PSF matching. The blue histogram shows the photometry differences after the images have been degraded to 1" seeing.

Photometric Errors

Fluxes are estimated by subtracting the expected background flux from the measured flux within an aperture of some shape and size. The photometric errors, in the simplest scenario with un-correlated background noise and negligible systematic errors, are therefore estimated by combining the estimated background noise and the Poisson noise from the object in quadrature. The error in the estimated background or sky value is often taken from the standard deviation of the pixel values within an annulus centred on the object in which the background value is estimated. If the images have been interpolated at any point, however, then the pixel values are likely to be correlated over some characteristic scale. In the case of the UDS images, the observing strategy employs a jitter to enable sub pixel-scale resolution and in the case of the Subaru images, they are resampled and interpolated to the same astrometric solution of the UDS images (see above). A simple standard deviation is then not sufficient to describe the error and you have to worry about off-diagonal terms in the covariance matrix to correctly characterise the noise in the image.

In the case of the UDS images, they are background limited and this correction is important.

The final photometric errors were calculated according to Equation 2.1, where F is the flux, N the number of frames contributing to a stack, g the gain in $e^{-}ADU^{-1}$, $\sum C_{ij}$ is the sum of the terms of the covariance matrix, A the area of the aperture, and σ the error in the background estimate.

$$\Delta m = 1.0857 \frac{\sqrt{A\sigma^2 \sum_i C_{ij} + \frac{F}{Ng}}}{F} \tag{2.1}$$

Photometric Zeropoints

Stars occupy fairly well-defined regions in colour-colour space and so can be used to check the accuracy of the photometric zeropoints of the catalogue, as plotted for various colour combinations in Figure 2.5. The only bands with obvious systematic offsets are the z' and J-bands (see panels 2.5(d-f)) whereas no systematic offsets are seen between the optical and H- and K- bands (panels 2.5(k) and (l) respectively). The zeropoint offsets were estimated by eye to be +0.1$\pm$0.05 and -0.15$\pm$0.05 in the z' and J-bands respectively.

2.4 Dealing with the confusion limit in Spitzer Images

The depth reached by the spUDS images ($Mag_{3.6\mu m} \sim 24$(AB)) make them deeper than the K-band images used here. They are, however unsuitable for defining the source catalogue from since the large PSF of Spitzer coupled with the depth of the images introduces a new problem, that of source confusion which is displayed in Figure 2.6. Objects which were distinct in the K-band image but separated by ≤ 2 arcseconds now overlap in the IRAC images and reliable aperture fluxes can no longer be easily obtained. To tackle this problem, the superior resolution of the UDS K-band image has been used to set priors on position and shape of objects, which are then fit to the IRAC images to obtain fluxes using a method similar to that employed in creating the GOODS-MUSIC catalogue (Santini et al., 2009). To produce a band-merged catalogue including IRAC and MIPS photometry they developed an algorithm, convPhot (De Santis et al., 2007) using the Hubble ACS z-band images as a prior for the position and morphology of the sources. To produce the band-merged UDS catalogue here, the prior is produced from parametric fits to the object profiles in the K-band.

The steps involved in the process are as follows and are displayed in Figure 2.7:

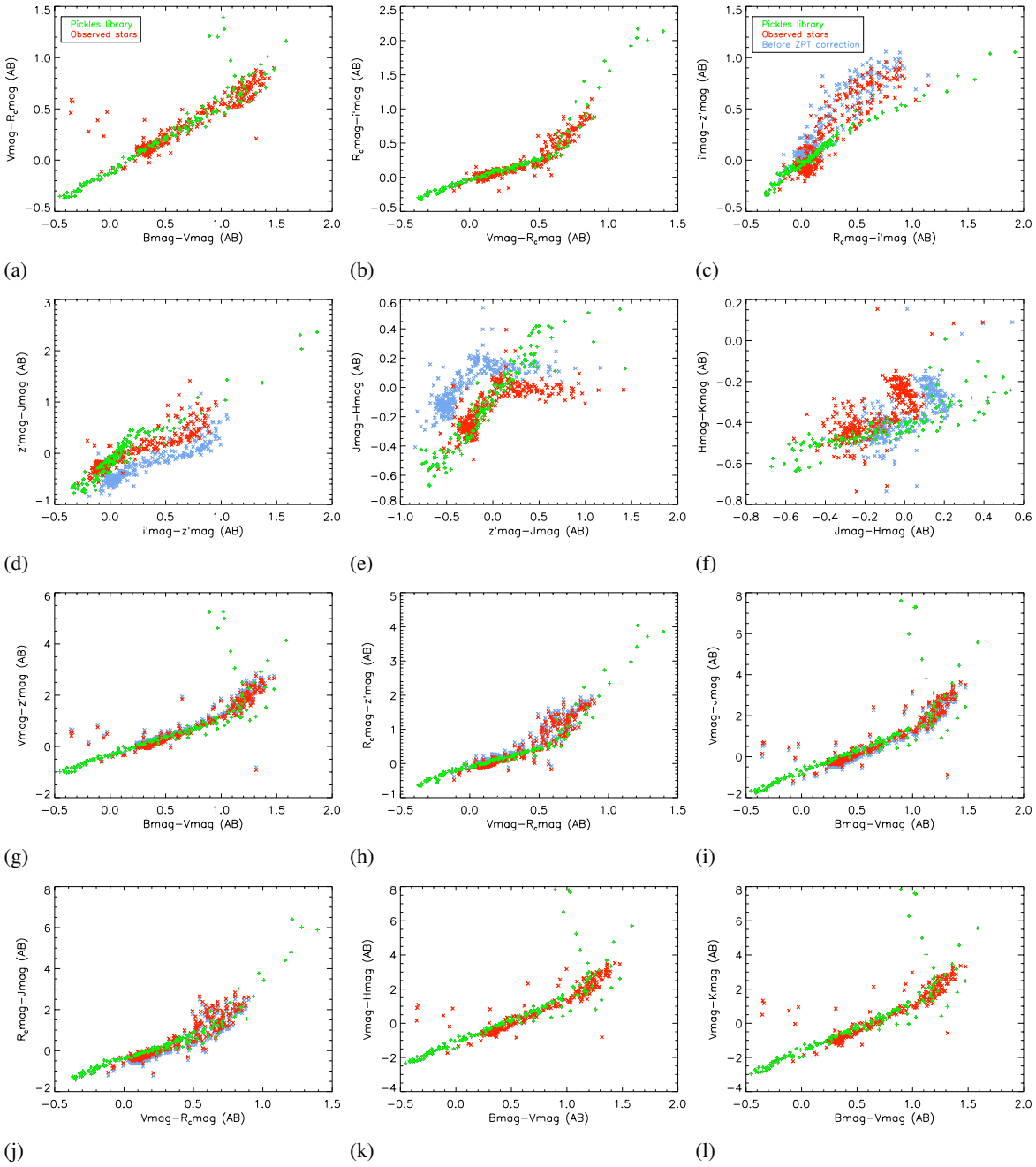

Figure 2.5: Observed stellar colours (green symbols) plotted alongside the stellar colours from the Pickles stellar library (Pickles, 1998) (red symbols). The blue symbols show the stellar colours before correcting for systematic offsets in the z' and J-band zeropoints.

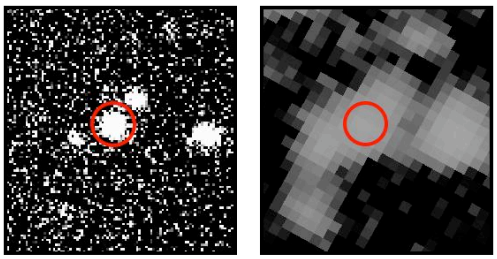

Figure 2.6: *Confusion in spUDS images.* The left hand panel shows an object in the K-band image with a 2" aperture in red. The right hand panel shows the same object in the IRAC 3.6μm image with the same aperture. Now the aperture contains flux from the two adjacent objects as well as the object of interest.

- Extract sources from the K-band image using SExtractor (Bertin, 2006).
- Construct a PSF of the K-band using the IRAF Daophot task, PSF.
- Using the Segmentation image to determine which pixels belong to which objects, each object is then fit with a bulge-disk decomposition using the IRAF package GIM2D (Simard et al., 2002).
- Construct a PSF for each of the IRAC mosaics, being careful with the normalisations (see details below).
- A kernel was then constructed using the IRAF task PSFMATCH that is then used to convolve the model profiles to the resolution of the IRAC images.
- Calibration of differences in astrometry between the UKIDSS and Spitzer images.
- Fit the normalisation of the simulated objects to the IRAC images using an Expectation-Maximisation algorithm (E-M algorithm).
- Colour corrections can then be applied to the IRAC colours as explained in the IRAC data handbook (Handbook, 2010).

2.4.1 IRAC mosaics

IRAC mosaics were built using MOPEX (Makovoz, D. & Khan, I., 2005), a custom built program for mosaicing Spitzer data. The CBCD images have already been corrected for several artifacts and are mosaiced as they stand.

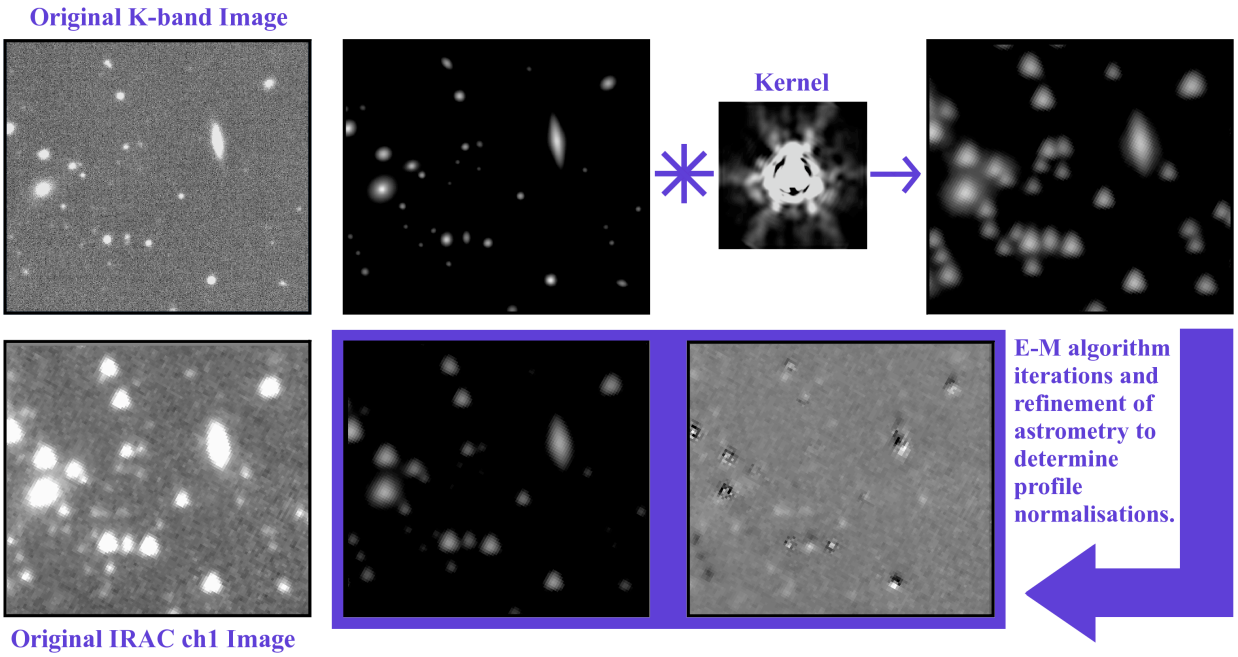

Figure 2.7: *The steps taken to produce IRAC photometry free from the effects of confusion.* Starting with the K-band UDS image, priors in object positions and profiles are determined by parametric fitting. These are then normalised to unit flux and convolved with the appropriate kernel to reduce the resolution to that of the IRAC images. Overall object normalisations are then determined for each object using an iterative Expectation-Maximisation (EM) algorithm, fitting to the IRAC images.

The different stages in mosaicing are:

- Background matching
- Astrometric registering and re-sampling CBCD images to common astrometric frame.
- Remove outliers from multiple images covering the same area. This corrects for cosmic ray hits/hot pixels in individual images.
- Combine images.

The different channels were mosaiced to the same astrometric frame, with 0.6" pixels that sub-sample the native 1.22" pixels of the CBCD images.

2.4.2 Parametric fitting to objects in UDS K-band image

The GIM2D package

The IRAF package, GIM2D (Simard et al., 2002) has been designed to produce parametric fits to large samples of objects, and is used here to fit to the profiles of the K-band objects. It fits a simple bulge+disk profile to the object profiles with a maximum of twelve parameters: the total flux, bulge fraction, photobulge semi-major axis effective radius, photobulge ellipticity, photobulge position angle of the major axis on the image, the photodisk semi-major axis exponential scale length, the photodisk inclination, photodisk position angle on the image, subpixel x and y offsets of the galaxy centre, background residual level and Sérsic index of the bulge. When fitting to the image, each model profile is convolved with the supplied psf. The complicated topology of the 12-dimension parameter space is sampled and the global minimum in χ^2 is found by use of the metropolis algorithm. The algorithm was allowed the full range in each of these parameters when fitting so as not to introduce any bias into the fits.

The package uses the segmentation image produced by SExtractor to determine which pixels belong to which deblended source and which to the background. For each object a thumbnail image is extracted from the original image and segmentation image. I used the option to re-calculate the background value and σ which then uses the pixels with flag 0 in the segmentation image as the background pixels. There is the option to leave a buffer zone around the object pixels to ensure that any low surface brightness extremities of the objects do not contribute to the calculated background.

The program then outputs an image of the object profile which is the result of the convolution of the theoretical profile, described by the best-fit parameters above, with the supplied image psf. Each iteration of the algorithm is documented in a log file and the residuals left by the fit are output as a residual image tile.

2.4.3 IRAC psf

The Spitzer PSF is under-sampled in the IRAC images and the pixels vary in sensitivity across their surface. These two effects together mean that the realisation of the PSF differs depending on where on a pixel the centre falls. When the BCD images are later mosaiced, the shape of the PSF will also be determined by the projection of the local dither pattern employed while observing. This means that modelling the psf by fitting to stars in the image, as with the Daophot PSF task, is not sufficient.

The Spitzer Science Centre[4] supply accurate Pixel Response Functions (PRFs). These PRFs combine the information of the instrument PSF, the detector sampling and the pixel sensitivity by providing realisations of the PSF as it is detected when its centre falls at different positions within its peak pixel. These realisations are also supplied for 25 subsections of the detector array on a 5x5 grid.

These PRFs are used to construct a model PSF (Figure 2.8) for the final mosaic, preserving the normalisation required to match the calibration of Spitzer data within the calibration aperture (explained in Section 2.2.3). The steps used to create these model PSFs are described below.

- The PRFs are first normalised to contain unit flux within an aperture with a radius of 10 native pixels and a background annulus with inner and outer radii of 12 and 20 pixels respectively. A correction is applied to take account of the differences in flux measured at different pixel phases (position of the centre of the star within a pixel).
- A sample of stars was created, selected to be unsaturated, with $K_{AB} < 15$. A model PSF was built for each of these stars by inserting the appropriate PSF realisation into a blank CBCD frame at the position that the star would appear. These model CBCDs were then mosaiced in the same way as the original CBCDs.
- The stars are then assigned to a 3x3 pixel grid according to their position in the final mosaic image and the stars from each section are centered on a pixel and averaged to model the mosaic PSF and its variation across the image.

PRF normalisation corrections

The IRAC core PRFs supplied by the Spitzer Science Centre need to be normalised to unit flux within the calibration aperture. The individual realisations are only 25x25 pixels, however, so this is not big enough to find the full correction including the contribution from the background annulus. The extended PRFs are therefore used, which display the PRF for the whole extent of the detector (256x256 pixels) but only for a star centred on the detector. The ratio of the sum within the calibration (12" diameter) aperture to the flux obtained by including background subtraction is calculated by performing photometry on these extended PRFs.

[4] http://ssc.spitzer.caltech.edu/

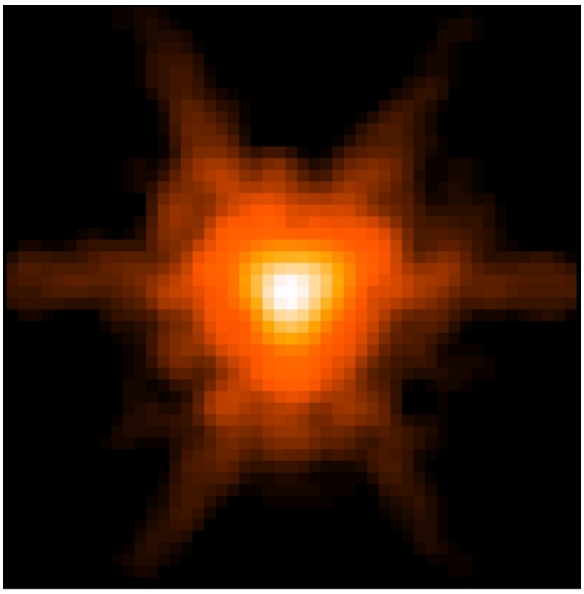

Figure 2.8: The IRAC CH1 mosaic PSF, shown in a logarithmic scale (PSF for central region of mosaic).

To apply this correction to the core PRFs, a little bit of care is needed. First, since the flux within a 10 pixel aperture is different depending on the pixel phase of the PSF (where within the central pixel the centre of the PSF falls), one single phase needs to be chosen for calculating the sum within the aperture.

The CBCD calibration is such that it is equally likely for the flux to be high or low compared to the true value. Therefore, to find the true flux of a star observed at pixel phase $p = \sqrt{(x-x_0)^2+(y-y_0)^2}$ within the calibration aperture, a correction must be applied:

$$C(p) = 1 + 0.0535 * [\frac{1}{\sqrt{2\pi}} - p] \tag{2.2}$$

The normalisation of the PRFs will therefore follow the calibration if the zero phase realisation of the PRF is chosen and a correction factor applied with $p = 0$. The overall normalisation applied to the core PRFs is:

$$\frac{PRF\,sum, phase = p}{PRF\,sum, phase = Zero} * \frac{ExtendedPRF\,flux}{ExtendedPRF\,sum} * C(0) \tag{2.3}$$

Model Stars

The mosaic PSF was modelled by using a selection of stars in the image. For each star, an artificial star is produced using the following steps

- First, the CBCD frames in which the star is detected are determined.
- The true star center is compared to that determined using the OFILTER centering option within the IRAF task, PHOT, and calibrated using the IRAC PRF realisations that are centered at different points within the central pixel. This was the only centering option that was able to center on the PRFs in a way that could be calibrated. The other options were prone to failing.
- Photometry is performed on each CBCD tile using the IRAF PHOT task. Centering was used with the OFILTER option to determine the true star centres.
- A model frame was made for each tile with the PRF realisation added at the correct centre position.
- These tiles are then mosaiced using the same MOPEX parameters as used for the original mosaic.

2.4.4 Creating IRAC image profiles

The object profiles output from GIM2D need to be convolved to the resolution of the IRAC images. This is done by creating a convolution kernel from the K-band and Spitzer PSFs, using the IRAF task psfmatch. The object profiles and K-band psf are first normalised to unit flux and the normalisation of the IRAC psf is carefully set to correspond with the calibration of the cbcd images, as described in the previous section. The objects are then resampled to their correct position within the IRAC pixel grid.

2.4.5 Fitting model profile normalisations

Expectation-Maximisation algorithm

An iterative approach is used to fit the normalisation of the object profiles in the IRAC images, using an Expectation-Maximisation algorithm (E-M algorithm). The algorithm is explained in more detail in Appendix A.

Essentially, the final normalisation of an object is determined by fitting the contribution of the flux from all the overlapping objects at each pixel. The estimate of the object normalisation is scaled according to the ratio between expected flux (from the scaled, modeled profile) and the measured flux. This ratio is scaled according to the relative contribution of the object across its profile. This new estimate is then used in the next iteration.

Array-location dependent photometric corrections.

As mentioned in Section 2.2.3, the IRAC flat field has been derived from the high surface brightness zodiacal background. This peaks red-wards of the filters, and so for bluer sources, a colour correction has to be applied which is location dependent since there is a variation in the effective filter bandpass with angle of incidence. These corrections have been measured and are supplied by the Sptizer Science Centre[5] as images the same size as the BCD products that apply multiplicatively to the BCD images.

To apply these corrections to the final mosaic, a separate file is made corresponding to each CBCD image contributing to the mosaic, with the CBCD header file copied into the header of the correction image. These correction images are then mosaiced using the same parameters as for the science mosaic. The resulting correction image is then multiplied by the science mosaic.

Astrometry Refinements

After finding the first estimate of profile normalisations a second refinement of the astrometry can be performed using the simulated image. Centering is performed, within the IRAF task PHOT using the OFILTER centering parameter, at the positions in both the mosaic and the simulated image. The average difference in astrometry for each source is defined by averaging the astrometry differences within a 20" radius centred on each source. These then define tie-points to be supplied to the IDL procedure WARP_TRI to warp the original mosaic image that is then used to adjust the normalisations by running through EMalgorithm again. This procedure is displayed in Figure 2.9.

Error Estimates

The error estimates are determined directly from the residual image (image-fitted profile) according to Equation 2.4. The residuals are weighted according to the shape of the profile at each given pixel.

$$\sigma_{flux} = \sqrt{\frac{\Sigma_{i,j} profile(i,j) * (img(i,j) - profile(i,j))^2}{\Sigma_{i,j} profile(i,j)^2}} \tag{2.4}$$

[5] http://ssc.spitzer.caltech.edu/irac/calibrationfiles/locationcolor/

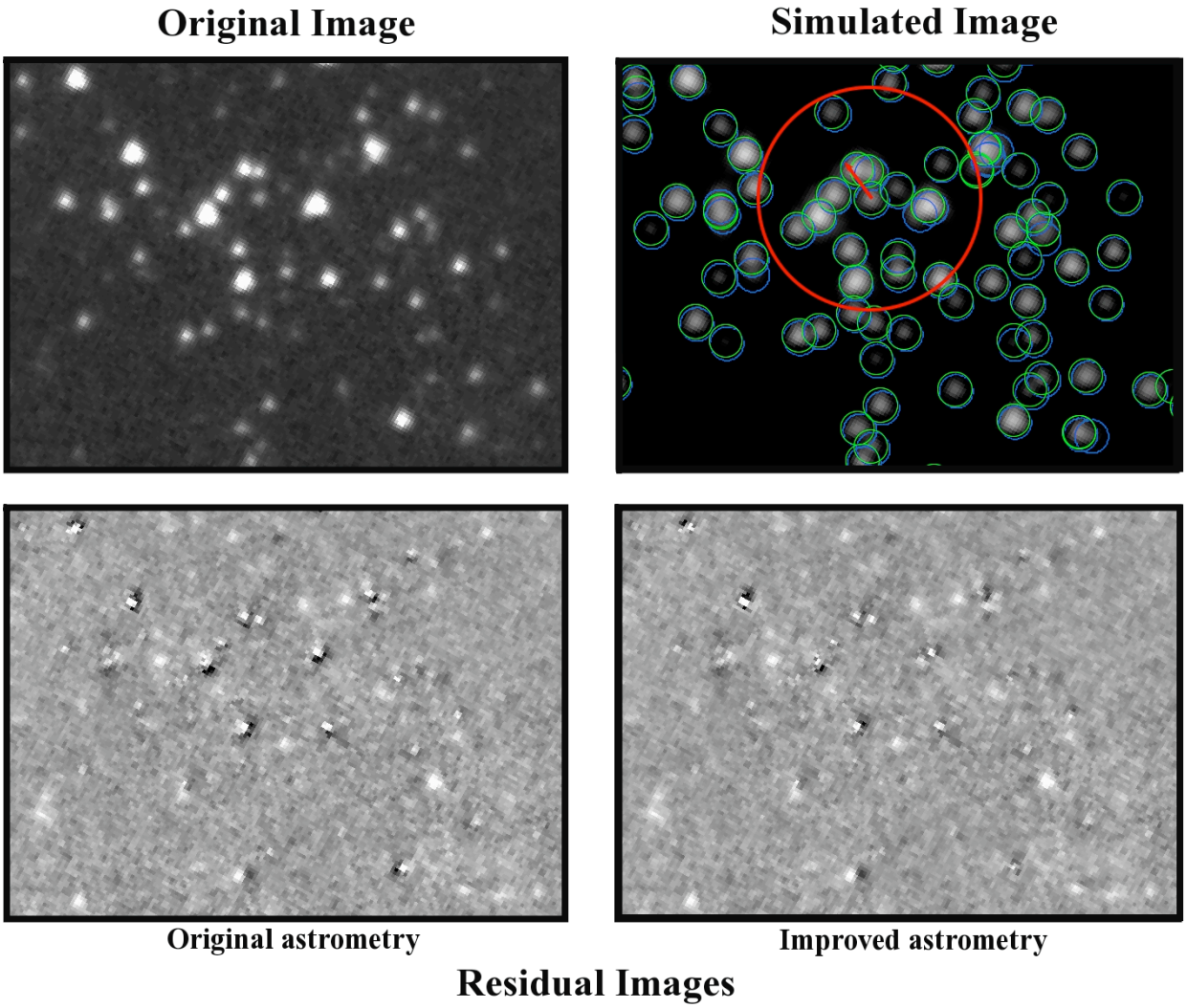

Figure 2.9: Displaying the method used to refine the astrometry corrections. Photometry is performed at the positions of objects in both the original image (top left) and the simulated image (top right). The blue circles in the simulated image show the original object positions estimated from the K-band astrometry and corrected for large scale offsets (see text). The green circles show the newly centred positions. Taking each object, the offsets between these centres are averaged within a 20" radius (size of red circle). The arrow shows the direction of the required shift that needs to be applied to the original image to match the position in the simulated image for the object at the centre of the red circle. The original image is then warped to match the positions of objects in the simulated image. The two residual images below show the pattern of residuals before (bottom left) and after (bottom right) this correction is applied. There is a visible systematic pattern in the before panel that has been improved by applying this correction.

2.4.6 Results

To test the normalisations obtained by this method, one can compare them to aperture photometry performed on the mosaics. This requires the calculation of an aperture correction to be applied to this photometry, since the normalisations of convolved image profiles should provide total object fluxes. Even if the aperture were the same size as the calibration aperture, one could not assume these fluxes to be accurate as a mosaic will have different sampling within the pixels compared to the CBCD frames in which the calibration aperture is defined.

Mosaic Point Source Aperture Correction

To calculate the mosaic aperture correction, stars are chosen from the mosaic with flux $1000 < flux(\mu Jy) < 4000$. This selection ensures that the star is not saturated and lie above $\sim 10\sigma$. Photometry is performed on the stars in each of the CBCD frames where they are observed, within a 3 native pixel radius and a sky annulus with inner and outer radii or 12 and 20 pixels respectively. The flux is then multiplied by the aperture correction factor of 1.112 (Handbook, 2010) for this sized aperture. Finding the mode and standard deviation of these values provides a measure of the total flux of the star and the error in the measurement. A smaller aperture than the calibration aperture (10 pixel radius) was chosen to minimise the likelihood of the aperture containing bad pixels or cosmic rays. The number of different observations of the star at different positions on the detector takes account of the pixel phase corrections, since the calibration is such that there is equal probability of measuring flux higher or lower than the true value.

The same stars were measured within a 2" aperture with the same sized background annulus from the mosaic. A clipped mode of the distribution of ratio values of aperture to total flux is found, with it's corresponding standard deviation, to be: $0.78184380 \pm 0.010784788$.

Comparing normalisations to aperture photometry

Aperture photometry was performed on the CH1 mosaic in a 2" radius aperture with a background annulus the same size as the calibration annulus. A small sized aperture was chosen to mitigate the effects of crowding and confusion somewhat (to minimise the contribution of neighboring object flux to the aperture). The photometry was corrected to total using the mosaic point source aperture correction (obtained as described

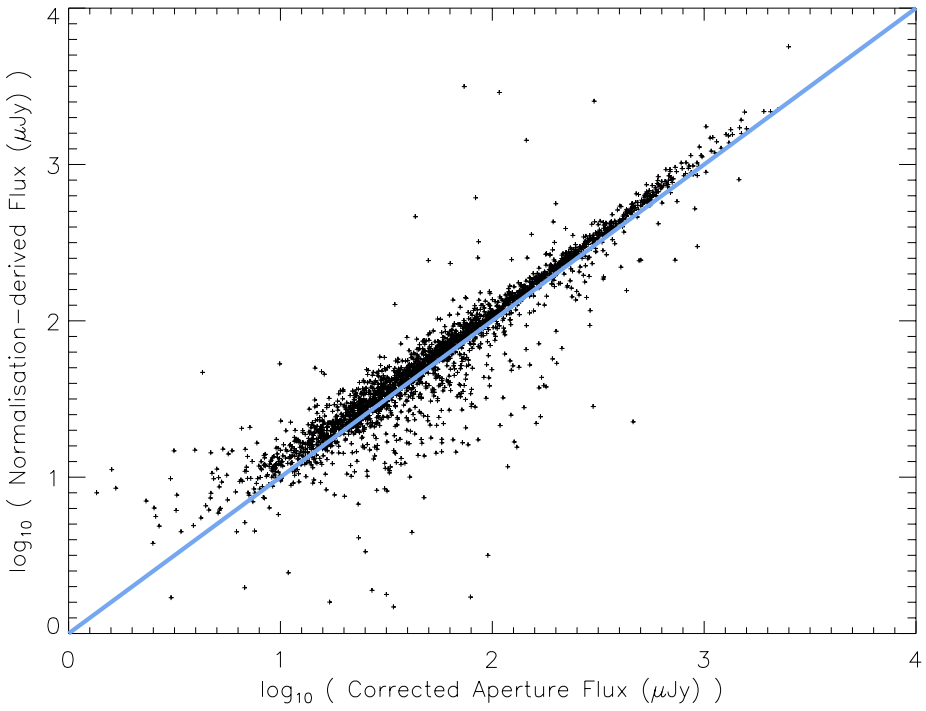

Figure 2.10: Testing the fluxes derived from the profile normalisations against aperture photometry (2" radius aperture) performed on the mosaic. A point source aperture correction has been applied to the photometry to scale the flux to the total flux (see text).

above).

Good agreement was found when comparing the aperture photometry to the fluxes derived by the prior method described above (Figure 2.10) for objects not identified as stars. The profile normalisations provide systematically higher fluxes than the aperture photometry. This is most likely due to the calculation of the aperture correction being derived from point sources whereas these objects are partially resolved.

Chapter 3

RSD Target Selection

Selection of Galaxies for a redshift survey designed to measure Redshift-Space Distortions (RSDs) requires a high redshift completeness for the observed objects and high survey efficiency of the target fields. The final survey selection function will depend on the sky subtraction strategy to be employed, as well as the physical surface density of observable targets in the redshift range of interest.

A high redshift completeness requires the objects to be in the correct redshift range with strong emission lines that can be used to secure a redshift. An important limiting factor to consider when designing the selection function is the availability of multi-wavelength data there over the required area from which to pre-select the targets. Proposed survey regions that are considered here are the Spitzer Wide-area InfraRed Extragalactic survey (SWIRE, Surace et al. (2005); Lonsdale et al. (2003)) and the Canada-Frace-Hawaii Telescope Legacy Survey (CFHTLS[1]), and the available broad-band imaging data in these regions are summarised in Sections 3.3.2, 3.3.3.

In order for the results from FMOS to be competitive, the result needs to be constrained at a redshift of $z \sim 1.5$ where Hα can be detected in the H-band. Not only are multiple line redshifts possible for the targets (with Hβ and [OIII] then falling in the J-band), but this is a region in redshift that has not yet got a satisfactory constraint from measurements of RSDs (referring the reader back to Figure 1.2, that shows the measurements of the growth rate function at different redshifts). For the number of nights likely to

[1]Based on observations obtained with MegaPrime/MegaCam, a joint project of CFHT and CEA/DAPNIA, at the Canada-France-Hawaii Telescope (CFHT) which is operated by the National Research Council (NRC) of Canada, the Institut National des Science de l'Univers of the Centre National de la Recherche Scientifique (CNRS) of France, and the University of Hawaii. This work is based in part on data products produced at TERAPIX and the Canadian Astronomy Data Centre as part of the Canada-France-Hawaii Telescope Legacy Survey, a collaborative project of NRC and CNRS.

be available for the survey and the number of field observations that translates to after considering time overheads and weather, achieving a 70% redshift completeness would allow a constraint to beat the 10% constraint afforded by WMAP.

Current tests of colour selections based on UKIDSS B-R_c-i colours have so far afforded a low completeness rate and do not allow a selection of only H-band candidates[2]. This colour selection is based on the available broad-band data in the RCS (Red sequence Cluster Survey, Yee et al. (2007)) fields (with g',r',i' photometry extending over $\sim$1000 square degrees), originally aimed towards a Baryonic Acoustic Oscillation (BAO) redshift survey. Here, we are concerned with measuring redshift space distortions, for which the area of the survey is not so important and other, smaller surveys can be considered as target fields. There is a relatively unexplored possibility of using Spitzer IRAC photometry from the SWIRE survey to select high redshift sources (above $z \sim 1.5$) placing Hα into the H-band.

As a short aside, there are a couple of considerations that should be noted for the use of Hα emission to determine galaxy redshifts. The first is the existence of galactic outflows in star-forming galaxies caused by the injection of energy into the inter-stellar medium by supernovae. Their existence has been inferred from the difference in redshift inferred from spectral features associated with different galaxy components (for example in Lyman-break selected galaxies (Shapley et al., 2003)), as well as the appearance of lines that require a higher ionisation temperature than provided by massive stars alone, yet with no evidence of an AGN their existence is attributed to shock heating of the gas by these outflows. If the features associated with stars are used to infer the systemic redshift of the galaxy then low-ionisation lines associated with the neutral gas, and high ionisation lines associated with the ionised gas were measured to have systematic velocity offsets (to that of the stellar features) of order $\sim$-100 to -200km/s in the average spectra of the Shapley et al. (2003) lyman-break selected galaxies. This indicates that the spectral features are coming from material that is moving towards us (in the rest frame of the high-redshift galaxy) and so is being emitted from the near side of an outflow. At $z \sim 1.5$, these outflow velocities produce a systematic blueshift of order $\Delta z < 0.002$ which is actually the order of the expected accuracy of the determined redshifts in low-res mode, and so should not pose a significant problem.

The second consideration is the presence of Balmer absorption lines. The Hα emission lines are produced in ionised HII regions by the recombination of ionised Hydrogen. These HII regions have been

[2]Results presented at the FMOS meeting, Oxford, 2010 by Totani, T. and Sumiyoshi, M.

ionised by hot, young O- and B-type stars which dominate the UV-continuum shape in galaxies, when they are present. In the atmosphere of slightly cooler F- and A-type stars, there are absorption features, including Balmer absorption lines. As the dominant stellar population shifts from hot O- and B-type stars to cooler, longer lived stars, with stronger intrinsic absorption, these absorption features become more dominant in the UV continuum, reaching a maximum equivalent width at about 200Myr-1Gyr after a starburst event Kauffmann et al. (2003). There are two effects here that will decrease the detectability of Hα. The first is the decrease in the hot ionising continuum that ionises the HII regions in the first place (with the death of the short-lived, hot stars), and the second is the fact that the absorption features are coincident with the emission (being caused by the same electron transition). Although these two spectral features occur in physically distinct regions within the galaxy (stellar atmospheres and the ISM), and so the intrinsic Hα emission from the HII regions is not affected by the absorption features, they will act to decrease the signal to noise of the detected Hα line (peak of line = line peak flux + continuum flux). In the objects we are targeting, given the desired exposure time of 1 hour, we will not see significant continuum and the resultant signal to noise of any detected Hα will be dominated by the sky noise. As such we will likely only successfully detect very strong intrinsic Hα emission from objects whose UV continuum is still dominated by hot O- and B-type stars.

3.1 Photometric Redshifts

3.1.1 Template Fitting Method

There are two main techniques used to calculate photometric redshifts, both of which involve comparing the observed spectral energy distribution (SED) with that expected for galaxies at different redshifts. The first method minimizes the chi-squared fit between the observed SED and a set of synthetic or empirical galaxy spectra shifted to a range of redshifts and convolved with the filter response functions (Hyperz (Bolzonella, M. et al., 2000) and Le Phare (Ilbert et al., 2006), for example). The second method uses a training set of SEDs with known redshift, either to calibrate the results from a chi-squared fit or to train an artificial neural network (ANNz, for example, (Collister & Lahav, 2004)).

χ^2 - fitting method

Le Phare (Ilbert et al., 2006) is a set of Fortran routines extensively used to produce photometric redshift estimates (see, for example Ilbert et al. (2006, 2009); Rodighiero et al. (2010) for use of the routine; Abdalla et al. (2008); Hildebrandt et al. (2010) for testing). It takes as input a photometric catalogue and the broad-band filter response functions. The template spectra chosen by the user are shifted to different redshifts at specified redshift intervals, reddened according to the chosen internal reddening law, and then depressed with the Lyman-alpha forest before being convolved with the filter response functions to obtain the expected flux through the filter. The chi-squared value (Equation 3.1.1) between the observed and template SEDs is then minimized and the optimal redshift for the best-fitting template SED assigned to the object. In Equation 3.1.1 $F_{obs,i}$, $F_{temp,i}$ and σ_i are the observed and template fluxes and their uncertainties though filter i respectively and b is a normalisation of the template spectrum.

$$\chi^2(z) = \sum_{i=1}^{N_{filters}} [\frac{F_{obs,i} - b * F_{temp,i}(z)}{\sigma_i}]^2 \tag{3.1}$$

Large spectral features that are detectable above the photometric errors help to constrain a redshift estimation. The 4000Å break is the main feature in the redshift range of interest that can be constrained within the wavelength coverage of the UDS data set. This break is caused by both the Balmer break, at 3646Å , and the accumulation of many metal absorption lines, extending over a large wavelength range, that increase the opacity of stellar photospheres and is therefore stronger in older, metal rich populations. There are many factors affecting the shape of galaxy SEDs, including age, metallicity, dust reddening and spectral type. These can sometimes affect the shape of the SED in very similar ways, producing degeneracies in redshift-colour space. One such degeneracy that can directly affect a redshift estimation is that between dusty, low-redshift, starforming galaxies and redshifted passive galaxies. Another such degeneracy is that between age and metallicity (Worthey, 1994). These degeneracies can produce catastrophic errors in the identification of the photometric redshift, which cannot be detected without comparison to a spectroscopic redshift. It has been shown that sampling the galaxy SED over a larger wavelength range can help to

break these degeneracies (Bolzonella, M. et al., 2000). Checking the absolute magnitudes of objects at the redshift estimates can also prevent some of the catastrophic errors (rejecting solutions for which the absolute magnitude is too bright).

Le Phare also has features allowing the user to add in prior information about the redshift distribution and calculating systematic offsets in the photometric zeropoints (see Ilbert et al. (2006)).

Template Library

The quality of the spectral template library used to fit to the object SEDs has a large impact on the reliability of the redshift estimates. The library needs to be representative of the full range of real objects, although too many spectra with very similar colours can lead to a poorer photometric redshift estimate when degeneracies are introduced into the template set.

The approach of Ilbert et al. (2006, 2009) is to use a small number of representative templates, interpolating between the spectra of different spectroscopic types to cover the colour:redshift space, without introducing too many degeneracies. This approach differs from that used in Bolzonella, M. et al. (2000) where the templates of Bruzual & Charlot (2003) are used with the photometric redshift code HyperZ. For this template set each galaxy model is reproduced at a range of ages, with a range of possible extinction. This second approach is useful when physical properties of the galaxies are of interest (eg. mass, age etc.) but these parameters can only be extracted with caution if the wavelength space is well sampled. For this exercise, the templates of Ilbert et al. (2009) are used, which consist of a set of templates produced by Polletta et al. (2007) and supplemented by 12 additional templates using the Bruzual & Charlot models (Bruzual & Charlot, 2003) (BC03) with starburst ages ranging from 0.03 to 3Gyr. These starburst templates are extended beyond $3\mu m$ rest-frame wavelengths using the bluest Polletta et al. (2007) template. The set of templates is then expanded by interpolating between some of the base Polletta et al. (2007) templates to more finely sample the colour-redshfit space but without introducing too many degeneracies. The resulting template set includes 31 templates in all.

The BC03 starburst models were also allowed to be extincted with the Calzetti et al. (2000) extinction law, with values of E(B-V) ranging from 0 to 0.5.

3.1.2 Preparation of Catalogue

As detailed in the previous chapter, a K-band selected catalogue has been produced in the UDS field, incorporating data from the Subaru B, V, R_c, i' and z'-bands, the UKIDSS J H and K-bands and Spitzer IRAC ch1 and ch2. The Subaru images were registered into the same astrometric frame as the near-infrared images, and all the optical and near-infrared images were convolved to a matched PSF with 1" FWHM.

The IRAC photometry was taken from the deep spUDS images that suffer from confusion. This was addressed by using prior information of the shapes and positions of objects from the K-band.

Photometric zeropoints were tested by comparing stellar colours with those from the Pickles spectral library (Pickles, 1998). Systematic offsets were corrected for the z' and J-band zeropoints. It is important to correct any systematic offsets of this kind as otherwise they can produce artificial features in the object SEDs that will be fit to by the template set and throw off the photometric redshift estimate. The errors were all added in quadrature with a minimum zeropoint error of 0.05 to account for any residual systematics.

Stars were identified as described in Appendix B and not assigned photometric redshifts.

3.1.3 Results

Spectroscopic redshift comparison

Figure 3.1 shows the comparison of photometric redshifts obtained with Le Phare to the known spectroscopic redshifts for the full spectroscopic sample, and also divided according to the class of the best-fitting models. The scatter in the photometric redshift estimates are estimated using the width of the distribution in $\Delta z/(1+z_{spec})$ where $\Delta z = z_{phot} - z_{spec}$ (determined from the width of the best-fitting Gaussian to the distribution), for the objects with $|\Delta z| < 0.15(1+z_{spec})$. The fraction of objects not satisfying this constraint is given as the catastrophic failure rate. The scatter and failure rate are summarised in Table 3.1.

One of the most obvious results is that those objects that are best fit with those templates expected to have a lot of star formation (BC03 starburst templates) show the highest fraction of catastrophic errors. Those objects where the Lyman-α break has been confused with the 4000Å break (z_{spec} ~2.5-3.5 but assigned z_{phot} values < 0.5) belong to this subset. Referring the reader to Figure 3.5 this may not be surprising given that any 4000Å break is weak in these galaxies.

The spiral templates show that the photometric redshift estimates are systematically lower than the

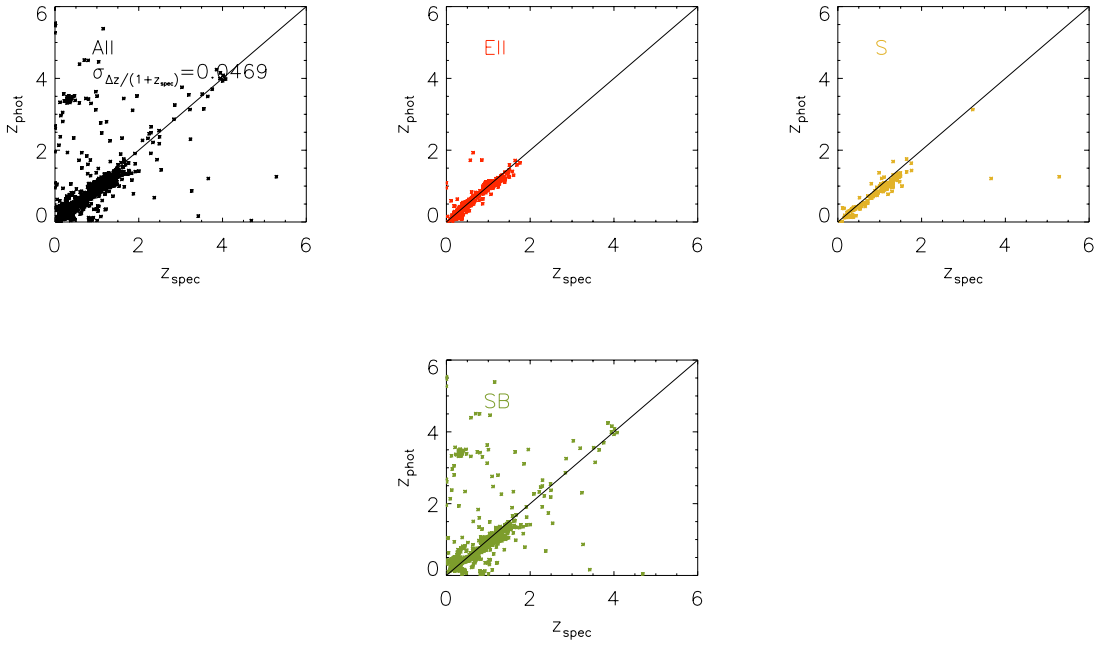

Figure 3.1: Photometric redshifts vs. spectroscopic redshifts.

Template	Scatter $\sigma_{\Delta z/(1+z_{spec})}$	Catastrophic faliure rate (%) $\lvert\Delta z\rvert > 0.5(1+z_{spec})$
All	0.0469	13.7
Elliptical	0.0214	6.9
Spiral	0.0525	7.6
Starburst	0.0327	17.9

Table 3.1: Scatter and Catastrophic failure rate of photometric redshift estimates, determined by comparison to a sample of spectroscopic redshifts.

spectroscopic redshifts by ~ 0.05. This is what causes the large scatter value given in Table 3.1, whereas the intrinsic scatter for this subset of objects is small, as it is for the Elliptical templates. As a template set, the photometric redshift estimates determined from different best-fitting templates do not show consistent systematic trends with redshift. These systematic trends must be inherent in the template set themselves, or introduced when including extinction as a free parameter, not an issue with systematic differences between photometric zeropoints. When the objects with best-fitting Elliptical templates are used to try to estimate any systematic differences in the filter zeropoints, no significant differences were found.

Photometric redshift distribution

The comparison of photometric to spectroscopic redshifts as an indicator of accuracy in the photometric redshift estimates is limited by the selection function of the spectroscopic sample. In this case the sample is selected from a mixture of X-ray and radio-loud AGN (Omar Almaini, private communication) as well as some red K-selected galaxies above $z = 1$ (Ross McLure, private communication). They do not represent typical K-selected galaxies. Scatter and catastrophic failure rate determined for the spectroscopic sample does not necessarily apply to the photometric sample. Another indicator of accuracy of the photometric redshift estimates is in the photometric redshift distribution.

Figure 3.2 shows the distriubution of photometric redshifts for the whole of the UDS field. Overplotted in blue are the secondary solutions for any sources with a secondary peak greater than 10% of the primary peak in the probability distribution. The distribution of the whole sample shows peaks at $z_{phot} \sim 2$. These are likely to be objects at $z_{spec} < 1$ for which the Lyman-α break has been confused with the 4000Å break, as in the example shown in Figure 3.3. These catastrophic failures do not affect the redshift range of interest around $z \sim 1.5$ so should not affect our selection mechanisms but they need to be considered when we look at the whole redshift distributions of any chosen selection mechanism.

A further test of the accuracy of the photometric redshifts at the redshift range we are interested in is looking at the distribution of photometric redshifts of the HiZELS objects that are selected from the nbH filter, putting them at approximately $z \sim 1.45$ (Figure 3.4). These show a sharp peak at $z_{phot} \sim 1.45$ and a small fraction ($< 7\%$) of catastrophic failures. Although the redshifts of these objects cover a small range determined by the width of the filter, they are representative of the objects that we are trying to target, being

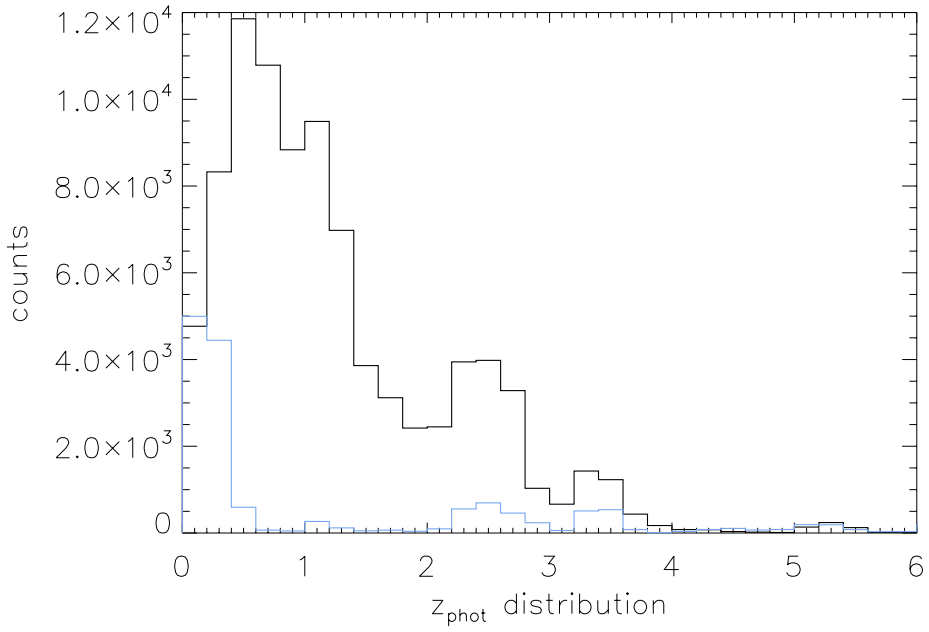

Figure 3.2: The photometric redshift distribution of the objects in the UDS. Over-plotted in blue is the distribution of secondary solutions (see text) showing that the peak at $z_{phot} \sim 2.5$ is mostly due to $z_{spec} < 0.5$ objects.

emission line galaxies themselves.

3.2 A redshift survey with FMOS

As a guide, we require about 30000 redshifts to constrain the linear growth rate of large scale structure at a redshift of 1.5. This number is estimated using a Fisher matrix calculation to estimate the error on the derived growth rate parameter (Edward Macaulay, private communication) and provides a constraint tighter than that provided by WMAP. The forecasted constraint on the growth rate supplied by this survey is ~ 4 times smaller than that supplied by the VVDS (see Figure 1.2, calculations and estimates supplied by Edward Macaulay). Of the predictions for the different models of the Universe shown in this figure, the constraint provided by FMOS potentially has the power to rule in or out; DGP Braneworld, a standard open Universe and Dark Energy - Dark Matter time-dependent coupling. Measurement of the growth rate parameter primarily relies on the number of galaxies for which you have redshifts, and not on the area covered. There is a minimum area requirement to make sure you average over cosmic variance (so as not to

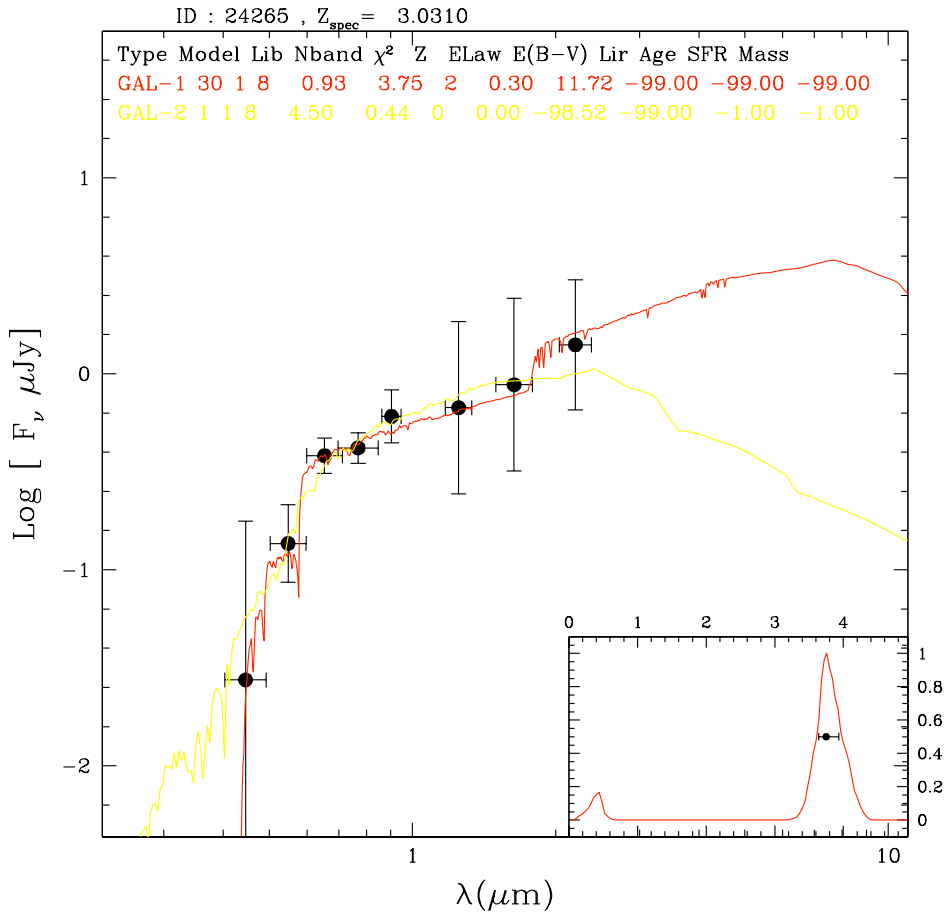

Figure 3.3: An example where the photometric redshift solution has confused the Lyman-α break for the 4000Å break. The red spectrum shows the solution with photometric redshift 3.75, placing the 4000Å break between the V and R_c filters, whereas the secondary solution, with photometric redshift 0.45, places the Lyman-α break between these filters (yellow spectrum). It can be seen that the confusion comes from the influence of the 1.6μm bump in the K-band filter, reddening the K-J colour in a way similar to the 4000Å break.

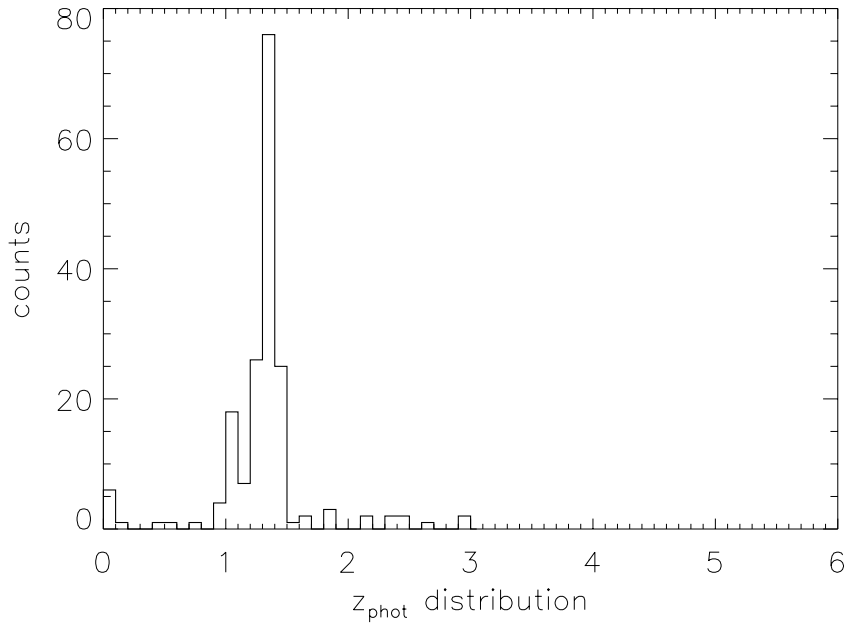

Figure 3.4: The photometric redshift distribution of HiZELS objects selected from the nbH filter

only measure the coherent infall into one particular over-dense region, for example). With the size of super clusters being of order 10Mpc, the minimum area of the survey should be of order 20x20 degrees. Above this minimum, the area of the survey does not significantly affect the results, it is more dependent on the number of objects you gain redshifts for as this determines the level of noise in the measured angular correlation function. The main requirement for your targets is that they are selected by a uniform method over your entire field. This ensures that the bias of the galaxies in your selection is uniform, since the actual measured quantity from the angular correlation function is also dependent on the galaxy bias. If FMOS has 60 nights, observing an average of 4 fields a night with 200 objects or 2 fields with 400 objects (1 hour integration) this makes 48000 objects (this is an average taking into account likely loss of $\sim 30\%$ time due to bad weather, as well as loss of time each night due to overheads). To be able to recover these 30000 redshifts this means that the redshift recovery efficiency needs to be as high as 62.5%. Is this kind of efficiency possible?

For the most efficient FMOS survey, we require the minimum surface density of targets to be 200 objects per FMOS field-of-view (FoV) (for which density we could employ cross-beam switching for sky subtraction, see Section 4.2.1 for a full description, but essentially half of the fibres are allocated to sky observations at any one time). This is a surface density of $\sim$1000 objects per square degree. If the surface

density of chosen sources is any lower than this then either the selection efficiency has to be higher or FMOS will need more time to accumulate enough redshifts. With a limiting surface density defined by 200 and 400 objects per FMOS FoV (according to the mode of sky subtraction chosen), we require an area of 48 and 24 square degrees respectively to reach 48000 targets. What this means is that for any selection mechanism chosen, the minimum surface density of targets we can consider is $\sim$ 1000 objects per square degree. For this surface density we would then require 48 square degrees of imaging data that was used to make the selection. If the surface density of objects is higher than 2000 objects per square degree then the tiling mechanism of FMOS pointings would be more complicated, but assuming that you could target all of the available objects with an efficient tiling strategy, then the area of the supporting imaging data required would scale with the number density of available targets.

These considerations are important and are the driving arguments of the following consideration of different selection mechanisms.

There are two different factors that need to be considered when creating the selection function; whether the objects fall in the correct redshift range where spectral features can be observed by FMOS; whether the spectral features are bright enough to be observed in an hour long integration. This second consideration is dependent on the amount of star formation in the system, where star formation is the dominant factor in the emission line strength, as well as the amount of dust or extinction in the system.

For this section, I assume that an emission line with flux 1x10^{-16}erg s^{-1} can be observed in an hour long integration with signal to noise of 5.

3.3 Target Selection

The catalogue and photometric redshift estimates for the UDS field can be used to test different approaches for selection of targets for the redshift survey, as well as how imaging depths and broad-band coverage would affect the selection.

The CFHTLS filters along with the IRAC ch1 and ch2 filters are shown in Figure 3.5 plotted over the 4 different model galaxy spectra that have been redshifted to $z = 1.5$. These templates are empirical SEDs representative of local Elliptical, Sbc, Scd and Im galaxies compiled by Coleman et al. (1980) and extended to higher wavelengths using the GISSEL synthetic models of Bruzual & Charlot (2003).

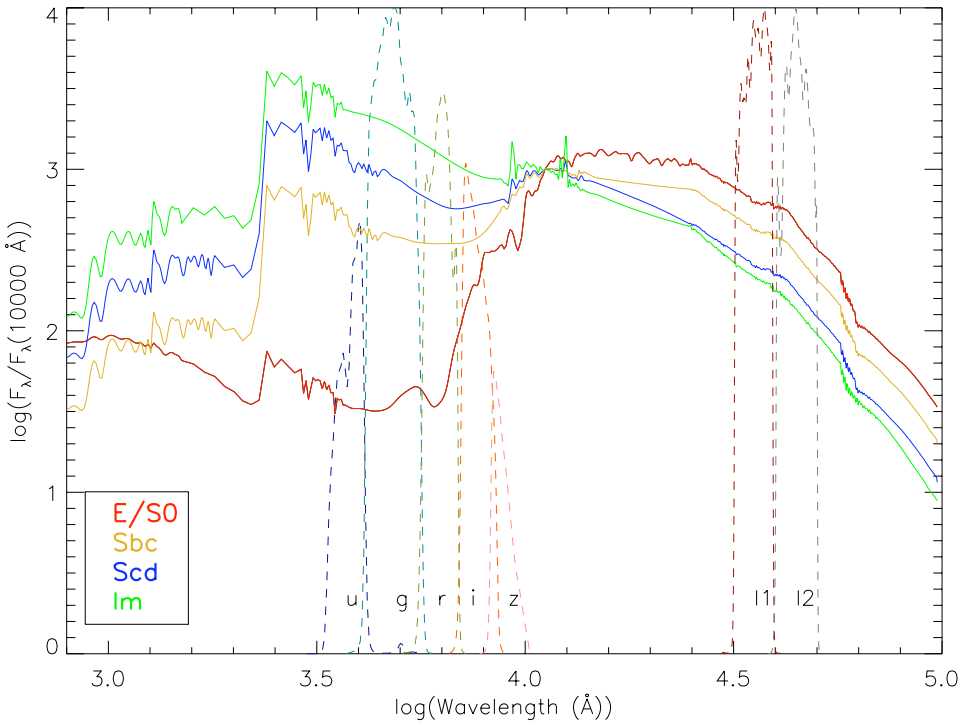

Figure 3.5: The CFHTLS and IRAC ch1 and ch2 filters plotted over the SEDs of the four CWW empirical galaxy templates (Coleman et al., 1980).

As described above, the three main spectral features that affect the fitting of photometric redshifts are; the Lyman-alpha break at $\lambda_{rest} = 1216$Å , seen in this figure at log(λ)$\sim$3.34; the 4000Å break, most obvious in the elliptical galaxy spectrum spanning 3.8 <log(λ)< 4.1; and the 1.6μm stellar bump, seen here in between the two IRAC filters at log(λ)$\sim$4.6.

This figure displays why it is difficult to select star-forming galaxies at redshift $z \sim 1.5$ from optical data alone, and why the wiggle-Z selection of FUV drop outs (Drinkwater et al., 2010) successfully targets emission line galaxies. In the wavelength range covered by the optical filters at this redshift, it is the old stellar populations that have the most distinctive broad-band spectral feature; the 4000Å break. The strongest spectral feature in the irregular and disc-like galaxies is the Lyman-α break but this is not covered by optical filters. In fact, the 4000Å break is not completely bracketed by the filters. To determine the most accurate photometric redshifts, one wants to be able to sample the SED long-wards and short-wards of the distinctive spectral feature, with filters in-between that track the feature as it passes with redshift. In the CFHTLS filter set, the z-band filter sits within the range of the 4000Å break at $z \sim 1.5$. This is where we require a filter

within the near infrared.

The IRAC ch1 and ch2 filters can help since, not only are they situated long-wards of the 4000Å break, but they also bracket the $1.6\mu m$ stellar bump. This feature has been successfully used to select high redshift galaxies (Sorba & Sawicki, 2010). This feature is not strongly dependent on the age of the stellar population and so a selection based on the ch1-ch2 colours would not discriminate against young populations, where we would expect to find emission lines.

There are two different approaches that can be used to determine a target sample, these are; using photometric redshifts to target the correct redshift range, possibly with a magnitude cut in the rest-frame UV band to preferentially select highly star-forming galaxies; use various colour-colour cuts to define a sample. The second option is attractive since there are various well-studied selection mechanisms, such as the BzK selection (Daddi et al., 2004) that has been shown to successfully split high and low redshift galaxies from each other, as well as the actively star-forming and passive galaxy populations. This approach may, however, not be optimal in this situation where a narrow redshift range is required. The selections often work best at separating low from high redshift objects by bracketing the 4000Å break with two filters, a finer sampling of the break would, however, be required to introduce finer redshift splitting. This finer sampling is, in effect, what photometric redshifts supply. Here, your redshift recovery would be limited by the scatter in photometric vs. spectroscopic redshift determinations, the flux in Hα as well as the catastrophic failures scattering objects in or out of the redshift range of interest. The scatter and catastrophic failure rate would be mostly limited by the depths and coverage of the SED in the region.

In the next section, I test the photometric redshift accuracy attainable with certain coverage and depth combinations afforded in different possible target fields, using the photometric redshifts attained for the sources in the UDS field. These are compared to possible colour-colour selection mechanisms.

3.3.1 Scenario One - The Ideal

First I will lay out an (almost) ideal situation; we have the full wavelength coverage and depth afforded to us in the UDS field over a wide enough area. This situation should show the upper limit to how well we could do in any target field as well as display the limits to the precision of using the photometric redshifts as a proxy for the spectroscopic redshift in later analysis.

Photometric redshifts

First, if we were to target a section of photometric redshift space, what would we expect to be observable with FMOS? First, we shall just look at what objects are likely to fall within the correct spectroscopic range.

For those objects for which we have spectroscopic redshifts in the range $1.4 < z_{spec} < 1.7$, most are of red galaxies, expected to have a strong 4000Å break that should increase the reliability of photometric redshifts. Looking at the redshifts within this range, the photometric redshifts are systematically lower than the spectroscopic redshifts by a mean of ~ 0.07. These systematic offsets that vary with redshift can be corrected for using the spectroscopic redshift sample. The spectroscopic redshift sample is also strongly peaked at the lower redshift range, so the fraction of objects chosen with $1.4 < z_{phot} < 1.7$ that lie within the spectroscopic range will not give a fair representation of the likely success rate of the photometric redshifts. Instead, the width of the distribution and catastrophic failure rate give us a better indication.

For those objects with $1.4 < z_{spec} < 1.7$, the catastrophic failure rate ($|\Delta z| > 0.15(1+z_{spec})$) is found to be 16% of the whole sample of 106 objects. The standard deviation of the distribution of Δz for the remaining objects is 0.1. The catastrophic failure rate is dependent on the types of objects targeted as well as the template set that you use. Given that these objects are not selected according to SFR and are not representative of the type of objects we will be targeting, this figure is not a robust estimate of the true catastrophic failure rate for the whole range.

Inverting the selection to see how many objects fall into the correct redshift range if targeted according to $1.4 < z_{phot} < 1.7$, a total of 24 objects out of 46 (as now only 46 of the entire sample have photometric redshifts in the desired range, as opposed to 106 objects with spectroscopic redshifts in the desired range) are within the correct redshift range. This indicates a success rate of $\sim 50\%$, but as ever, it must be stressed that this spectroscopic sample is not optimal for testing this selection mechanism.

A more representative sample is provided with the HiZELS nbH-selected sample (Figure 3.4). These objects are selected from a narrow-band filter and as such are expected to have spectroscopic redshifts within a small range. The catastrophic failure rate of the HiZELS sample, assuming all objects are at a redshift of 1.47, is 30% of the 163 objects and the standard deviation of the distribution in Δz for the remaining objects is 0.11. This is a more representative sample of objects given that they are emission line objects at the approximate redshift of interest. The intrinsic spread in true, unknown spectroscopic redshifts of the sample

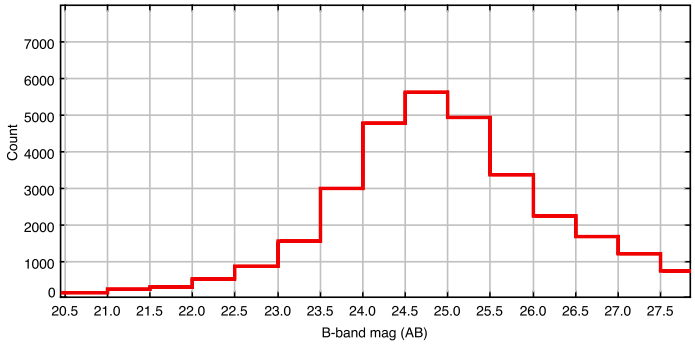

Figure 3.6: Distribution of B-band magnitudes for all objects within $1.4 < z_{phot} < 1.7$.

will make this estimate of the catastrophic failure rate a little high (since we expect the catastrophic failure rate to be higher for these star forming galaxies than for objects with a significant old stellar population producing a strong 4000Å break), though it is a good estimate for the ideal target population.

Observable Hα from B-band flux

Now we must consider how best to select objects with strong emission lines. This problem has been tackled by Sumiyoshi et al. (2009), who performed a calibration between the star formation rate of the best-fitting model obtained from χ^2 fitting to the broad-band photometric data in the UDS, to an estimated Hα flux. The calibration is performed on data in the SDSS using a smaller filter set at a different wavelength range, then the calibration is applied to the UDS data. Given the lack of coverage of the 4000Å break over the redshift range of interest (one of the main features expected to correlate to the emission flux as it provides information about the age of the stellar population), the large systematic errors in their photometric redshift estimates for the higher redshift objects, and the lack of observed Hα to test the results, an alternative, simpler approach to optimising the selections towards emission line objects at $1.4 < z_{spec} < 1.7$ will be used here.

The observed B-band magnitude of galaxies in the redshift range of interest traces young stellar populations, and hence likely star-forming galaxies, through the rest-frame UV. The GALAXEV (Bruzual & Charlot, 2003) package provides a tool which we can use to determine the observed B-band magnitude for star-forming galaxies with a limiting Hα flux of 1.6E-16 erg s^{-1} cm^{-2}, by using the rate of ionising photons

predicted by the stellar population synthesis model. A range of composite stellar populations with different e-folding times for the decline in star-formation-rate (τ) are produced (for a description, see Appendix C). The rate of ionising photons (Q_{ion}) then provides an estimate of the Hα luminosity according to Equation 3.2 (Wild et al., 2009), where 0.45 is the fraction of ionisations that lead to the emission of an Hα recombination photon (case B, Te = 1 x 10^4K and Ne = 1 x 10^4cm^{-3} Storey & Hummer (1995)), and $E_{H\alpha}$ is the energy of an Hα photon.

$$L_{H\alpha}[ergs^{-1}] = 0.45 * E_{H\alpha} * Q_{ion}[s^{-1}] \tag{3.2}$$

This luminosity can then be scaled to the limiting flux, using the luminosity distance of the object at the chosen redshift. The scaling factor determines the total stellar mass of the object and the observed B-band magnitude. To take account of how extinction affects the B-band magnitude compared to the Hα emission, extinction with values of E(B-V) ranging from 0.05 to 0.25 are applied to the models. The Calzetti et al. (2000) extinction law is applied to the continuum emission, while the value of $k(\lambda)$ at Hα is taken from the Milky Way extinction law (Seaton, 1979).

The optical depth of dust that obscures emission lines is a lot higher than that of the dust obscuring the continuum (Calzetti, 1997). This is thought to be because the line emission originates from stars that reside in much dustier environments. They are young, massive stars, whereas the bulk of the continuum reddening affects the light from older stars, residing in different locations from the dust. The Calzetti et al. (2000) extinction law is measured from a sample of external starburst galaxies and the overall extinction curve includes effects from light that is scattered into the line of sight by the dust. The light from emission lines does not suffer this effect, given the dusty, high optical depth environments, close to the emitting object, in which they are extincted. As such it is appropriate to use the results from the extinction measured within our own galaxy which does not include the scattering into the line of sight.

Calzetti (1997) suggest using $E(B-V)_{star} = (0.44 \pm 0.03) * E(B-V)_{gas}$ whereas here I use the value measured by Garn et al. (2010) of $E(B-V)_{star} = (0.5 \pm 0.14) * E(B-V)_{gas}$. This value was measured from the nbJ HiZELS sample using estimates of the extinction at Hα for $z \sim 0.84$ galaxies from comparisons of SFR determined from bolometric infrared luminosity estimates determined from stacked 24μm flux.

First, ignoring the effects of dust and extinction, taking a range of τ and ages of formation, the results are displayed in columns 5 and 6 of Table C.1. The results are summarised in brief in Table 3.2.

Extinction E(B-V)	0	0.1	0.2	0.3	0.4	0.5
Brightest B-mag	23.1	23.1	24.1	24.5	25.0	25.4
Faintest B-mag	23.6	23.8	24.8	25.3	25.8	26.3
Mean	23.3	23.4	24.3	24.8	25.2	25.0

Table 3.2: Summary of observed B-band magnitudes for different composite stellar populations at $z = 1.5$ produced using Bruzual & Charlot (2003), for a limiting Hα flux of 1E-16 erg s^{-1} cm^{-2}

Table C.1 shows that, for quite moderate stellar galaxy masses (Bundy et al. (2006) define massive galaxies as those with stellar mass $M_* \gtrsim 5x10^{11} M_\odot$), we can reach the H$\alpha$ flux limit, but that without the presence of dust, we expect the integrated B-band magnitudes to be very bright for these galaxies (mostly $B_{AB} < 23.5$), see Table 3.2. There is a question here of how these integrated B-band magnitudes compare to the 2" aperture magnitudes in the catalogue being used, and also how the integrated Hα flux limit compares to the flux collected by an FMOS fibre. Using a point source aperture correction of 0.2 ± 0.03mag for the B-band image as a minimum aperture correction for the expected flatter source profiles of the partially resolved objects, to compare to the catalogue photometry the faintest object from this table would be $B_{AB} \sim 23.776$ if it were a point source, and fainter if not. The aperture correction to be applied to the Hα flux produces a bigger effect, however. The fibre diameter serves as a much smaller aperture (1.2" diameter). For a point source with 1" Gaussian seeing, the differential aperture correction between the two apertures increases the brightness of the integrated B-band magnitude for an observed Hα flux limit of 1.6E-16 erg s$^{-1} cm^{-2}$ by ~ 0.4mag, whereas for 0.8" Gaussian seeing, the brightness is only increased by ~ 0.25mag.

Introducing extinction by dust into the mix, the lower limits to observable B-band magnitudes are much fainter. We do, however, require larger galaxy masses to provide the limiting Hα flux and the fraction of these at each redshift depends on the galaxy type-dependent mass functions. All we can really see from these simple toy models is that putting a limit in B-band magnitude at ~ 24.5 is not too faint to select star-forming galaxies, given that they are likely to be reddened by dust, an important consideration given that the most highly star-forming galaxies are observed to be the dustiest (Garn et al. (2010), for example); that the star-forming galaxies that we expect to be observable with FMOS can produce B-band magnitudes fainter than this lower limit for physical stellar masses; and that we expect the density of galaxies with

higher extinction that are observable with FMOS to be very low, given the high masses required (for the star formation histories explored here) to produce the limiting Hα flux, and the rapid decline in number density at these masses (Bundy et al., 2006). Therefore, allowing sources with fainter B-band magnitudes into our selection will likely dilute the success rate.

To test these inferences made from the above models, we can look at the B-band magnitude distribution of HiZELS nbH sources (Figure 3.7). These can be seen to peak at a B-band magnitude of 24, with a steep fall-off in number counts above 24.5. These magnitudes are not aperture corrected and so do not compare directly to our toy-model scenario but still indicate that a B-band magnitude cut would be a sound one to increase the probability that the object targeted is an emission-line galaxy. It should be emphasised at this point that the models assume that the Hα emission is driven solely by star formation with no contribution from a central AGN. The shape of the continuum as well as various line luminosities would be affected by the presence of an AGN.

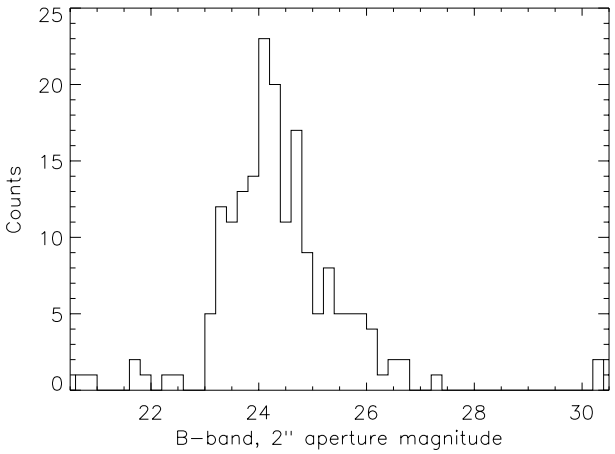

Figure 3.7: Distribution of B-band magnitudes of HiZELS nbH sources

Colour-colour selections

As to how well colour-colour selections can perform compared to these photometric redshifts, here we will test a few; the BzK selection (Daddi et al., 2004); a similar B-z-ch1 selection (Bz1). These selection methods are chosen for their ability to separate low redshift from high redshift galaxies by bracketing the 4000Å break. Selections involving the B-band also allow the possibility of dividing the population crudely

into passive and star-forming populations, though this does not take into account the effect of dust in star-forming galaxies producing redder colours.

Each selection region has been optimised to produce the highest fraction of objects with $1.4 < z_{phot} < 1.7$ having B-band magnitude less than 25 (AB). An additional requirement must be met for the selection, that the number density of sources must be at least 400 objects per FMOS field-of-view, or, approximately 2000 objects per square degree. The gradients and intercepts of the bounding lines of the colour selection region are then allowed to vary to find the selection maximising the fraction of objects with $1.4 < z_{phot} < 1.7$ and B-band magnitude brighter than 25 (AB).

The results are shown in Figure 3.8. For the BzK and Bz1 selections, this figure shows that the BzK selection should produce a success rate of $\sim 20-25\%$ for objects with $B_{mag} < 24.5$. The selection efficiency of each of the selection criteria is very similar, though the number density of BzK selected sources is much lower. It has, in fact, reached the number density limit imposed before finding a maximum in the success fraction. Given that this doesn't give any information of how the selection varies with different limits, the characteristics of a selection chosen by eye is used for comparison (Figure 3.9). This selection improves the success rate for $B_{mag} < 24$ at the expense of fainter sources. Given the improvement of number density and the fact that objects bright in B are more likely to be emission line galaxies, this selection would be more appropriate.

The two selections perform similarly, indicating that in the absence of K-band imaging, Spitzer would provide a suitable anchor filter longwards of the 4000Å break. An example of where this might be useful is with the addition of IRAC ch1 and ch2 data from a Sptizer warm mission covering the CFHTLS fields, which have deep optical photometry.

The results for the BzK selection are consistent with those that indicated in Sumiyoshi et al. (2009). This selection does not try to estimate the observed Hα flux, as is calibrated by these authors at low redshift against a sample of SDSS galaxies, explaining the higher success rates shown here for galaxies fainter in the B-band. This independently suggests that for fainter B-band magnitudes, the populations with bright enough Hα luminosity decrease in size, possibly due to the shape of the mass function, with number densities of the most massive galaxies decreasing rapidly, yet these are the ones that can produce enough Hα flux in the presence of large amounts of dust (see Section 3.3.1 and Appendix C).

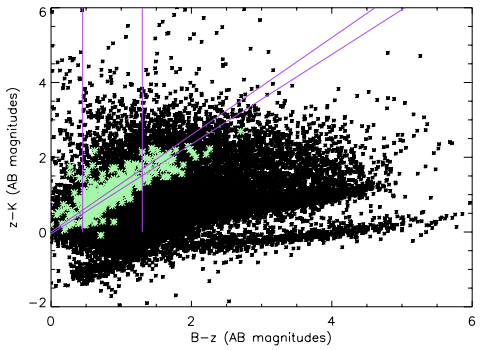

(a) The selection region in B-z-K colour-colour space

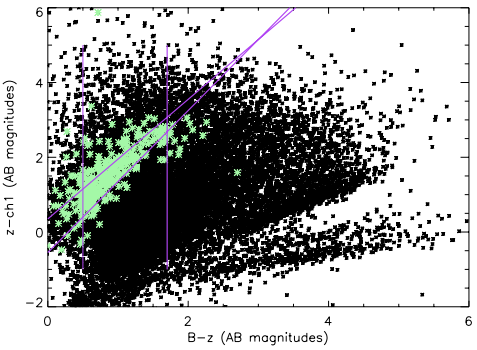

(b) The selection region in B-z-ch1 colour-colour space

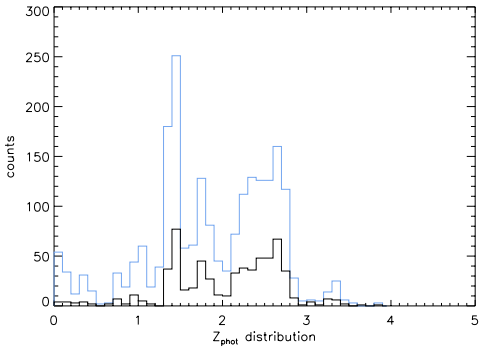

(c) The distribution of the photometric redshifts

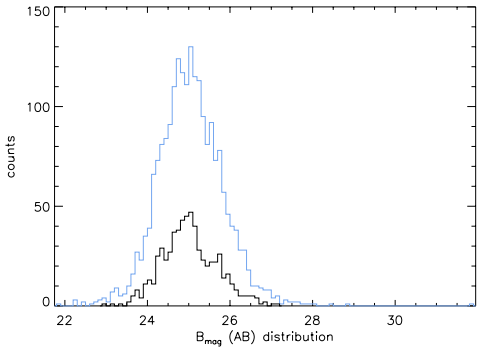

(d) The distribution of B-band magnitudes

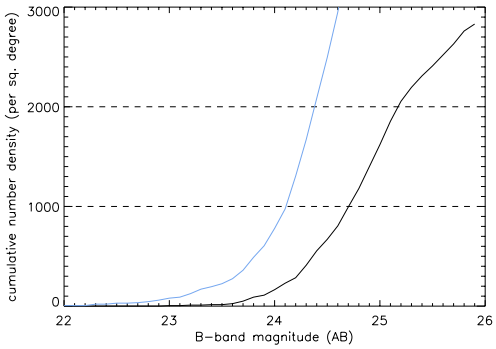

(e) The source number densities

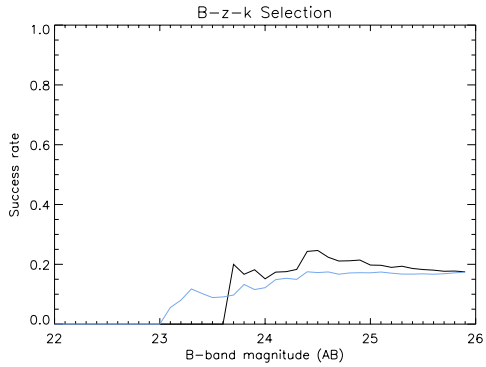

(f) The fraction of objects with z_{phot} within the chosen redshift interval

Figure 3.8: Optimised B-z-K and B-z-ch1 selection. For plots (c)-(f) the blue line corresponds to the B-z-ch1 selection and the black line corresponds to the B-z-K selection. (a) Shows the region in B-z-K colour-colour space chosen to optimise the success rate of observing objects within the range $1.4 < z < 1.7$ for B_{mag}(AB)< 25, with number density high enough to obtain at least 400 objects per FMOS field-of-view. The green points are the objects with photometric redshifts within the range of interest. (b) Shows the region in B-z-ch1 colour-colour space chosen with the same criteria. (c) Shows the distribution of z_{phot} values for all of the objects falling into the respective colour selection regions. (d) Shows the distribution of B_{mag} values for all of the objects falling into the respective colour selection regions. (e) Shows the source density of all of the selected objects plotted against B-band magnitude, with the densities for 200 and 400 objects per FMOS pointing overplotted (dashed lines). (f) Shows the fraction of all objects with photometric redshifts falling in the range $1.4 < z_{phot} < 1.7$ plotted against B-band magnitude.

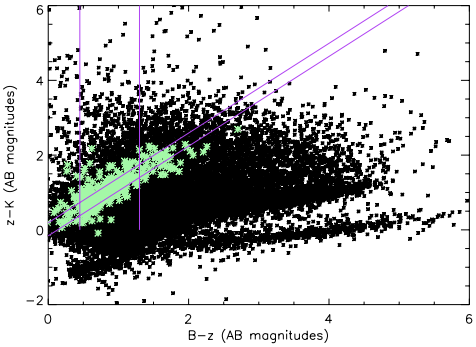

(a) The selection region in B-z-K colour-colour space, chosen by eye

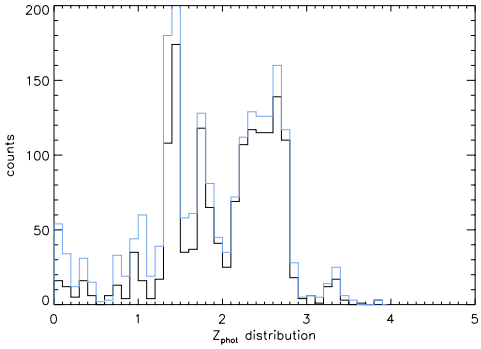

(b) The distribution of the photometric redshifts

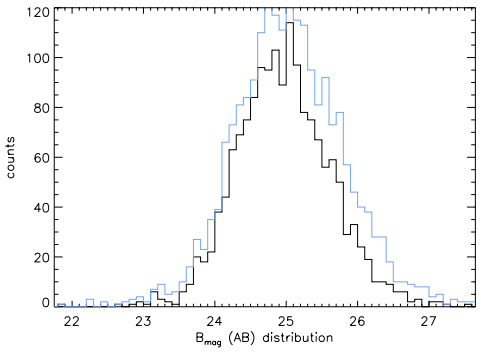

(c) The distribution of B-band magnitudes

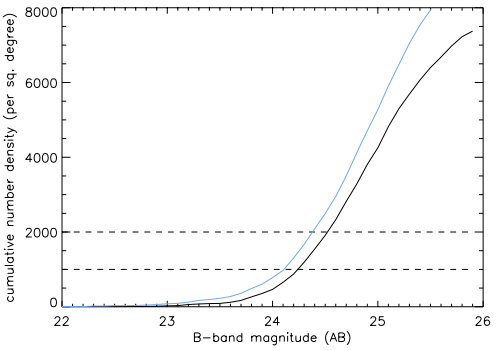

(d) The source number densities

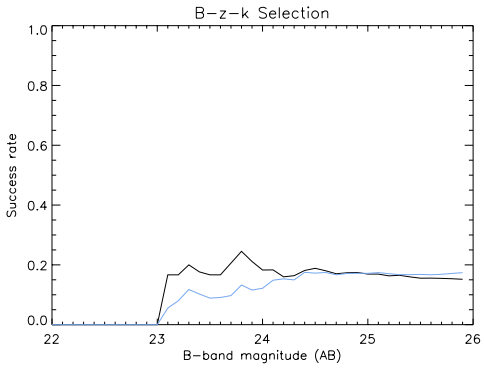

(e) The fraction of objects with z_{phot} within the chosen redshift interval

Figure 3.9: As for Figure 3.8 but only for the BzK selection, this time with the colour selection chosen by eye. The corresponding quantities from the Bz1 selection are still over-plotted in blue as a comparison

3.3.2 Scenario two - Using the SWIRE fields

In the case of photometric redshifts, it is well documented that the inclusion of near-infrared filters reduces the scatter and catastrophic failure rate of the photometric redshift estimates at redshifts $z >\sim 1.2$. The difference between photometric redshifts and other colour selections is that photometric errors can scatter objects in and out of colour selection regions in a way that is understood, and the effects can be modeled with knowledge of the data. With photometric redshifts, you cannot tell directly from the data that the estimate is catastrophically wrong, and without a fully representative sample of spectroscopic redshifts, you cannot even predict accurately the probabilities. So you need filters longwards of the 4000Å break for the photometric redshifts to be usable.

Table 3.3 details the coverage and depths of broad-band photometry in the various SWIRE fields as detailed in Surace et al. (2005) while Figure 3.10 displays the positions of the fields on the sky. The depths quoted for the UKIDSS-DXS (Deep Extragalactic Survey, Lawrence et al. (2007)) are the current depths covered in some of the fields, and the final depths aimed for, and reached in some fields. The Spitzer IRAC depths all reach ~ 21 mag (AB) with the SWIRE survey so the depths quoted in Table 3.3 are only for those fields with deeper Spitzer data.

Survey	Field	Available Bands - 5σ Limiting magnitude (AB)										
		B/U	V/g	R	i	z	Y	J	H	K	IRAC ch1	IRAC ch2
SWIRE	Lockman Hole	KPNO U Partial Coverage	g'	r'	i'			UKIDSS-DXS J (8.8/11 deg)		K		
			25.0	24.6	24.1			21.8-23.2		21.1-23.1	22.8	22.07
	ELAIS-N1	U_WFC	g_WFC	r_WFC	i_WFC	Z_WFC		""		""		
	ELAIS-N2	24.2	24.8	24.2	23.6	22.5						
	XMM-LSS		CFHTLS-W1					""		""		

Table 3.3: The multi-wavelength broad-band coverage of those SWIRE fields with supporting optical and near-infrared imaging, as detailed in Surace et al. (2005).

Catalogues

To be able to test the accuracy of photometric redshifts given the wavelength coverage and depths within the filters available for the different SWIRE fields, the catalogues must be altered. The two most important factors are; modelling which objects would not be detected given certain filter depths, and how the photometric errors will differ. The second point is easier to address and just involves scaling the errors such that they reproduce the given 5σ limiting magnitudes. Any objects now reduced to 1σ detections are recorded

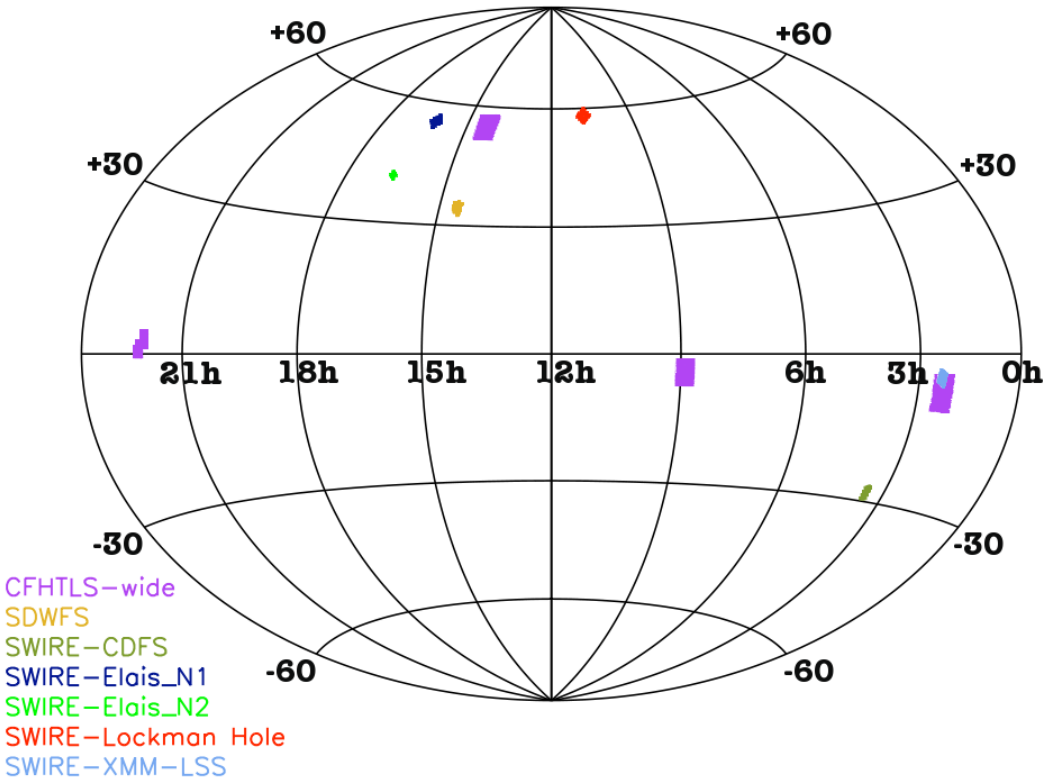

Figure 3.10: The positions of the various SWIRE fields, and the CFHTLS fields on the sky.

as undetected.

To reproduce a catalogue selected from the K-band with the given limiting magnitude is achieved by reproducing the observed drop in number counts observed in the original UDS K-selected catalogue about the new limiting magnitude. This effectively randomly selects which objects are detected using random sampling in magnitude bins to reproduce the required fall-off. Any objects not selected from the K-band are removed from the catalogue. The histograms of K-band magnitudes for each of the new limits used for the subsequent tests, as well as the original UDS catalogue are displayed in Figure 3.11.

Four catalogues have been produced with different depths and coverage, summarised in Table 3.4.

Results

Figure 3.12 and Table 3.5 summarise the results of using photometric redshifts in the SWIRE fields for filter coverage detailed in Table 3.4. For each catalogue the results both with and without the IRAC 3.6 and 4.5

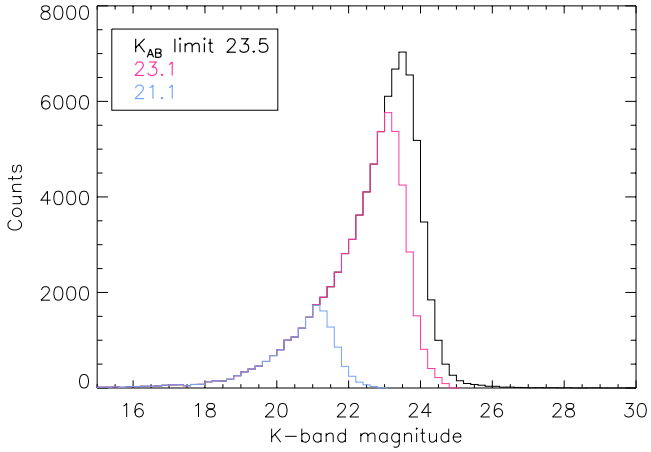

Figure 3.11: Histogram of K-band number counts for the two different K-band limiting depths tested (K_{lim} ∼23.1 in blue, and 21.1 in pink), as well as for the original catalogue (in black).

	Limiting magnitudes (AB) in filter									
Catalogue ID	B/u	V/g	R	i	z	J	H	K	ch1	ch2
1	24.18	24.18	24.16	23.59	22.47	23.2	N/A	23.1	21.	21.
2	24.18	24.18	24.16	23.59	22.47	21.8	N/A	21.1	21.	21.
3	N/A	24.18	24.16	23.59	N/A	23.2	N/A	23.1	21.	21.
4	N/A	24.18	24.16	23.59	N/A	21.8	N/A	21.1	21.	21.

Table 3.4: Artificial SWIRE catalogues

μm filters are shown (black and blue respectively) along with the cumulative number density of objects with their B-band or V-band magnitudes, depending on the filter coverage afforded by the catalogue.

Catalogue	fraction of objects at $1.4 < z_{spec} < 1.7$ from z_{phot} selection		total number of spectroscopic redshifts in photometric selection	
	without IRAC	with IRAC	without IRAC	with IRAC
1	0.51	0.48	51	42
2	0.40	0.36	25	28
3	0.34	0.42	94	48
4	0.23	0.42	73	31

Table 3.5: Fraction of objects selected from $1.4 < z_{phot} < 1.7$ that fall within $1.4 < z_{spec} < 1.7$ for the artificial catalogues with and without the IRAC bands. Here the IRAC spUDS images do not cover the whole area covered by UDS+SXDS so some of the objects with spectroscopic redshifts do not have deep IRAC photometry.

Taking each catalogue in turn, panels (a) and (b) show that, for the case of the broadest filter coverage and greatest depths in all the bands, the photometric redshift estimates perform well, with few catastrophic failures scattering into the range $1.4 < z_{phot} < 1.7$. The IRAC photometry does not drastically change the

results of the spectroscopic to photometric redshift comparison, but the number density indicates that more objects are occupying the photometric redshift range we are targeting. From Table 3.5 this increase in the number density is due to scatter into the photometric redshift range from other redshifts.

Panels (c) and (d) (Figure 3.12) show that the brighter K-band flux limit in catalogue 2 improves the photometric redshift estimates, but the number density of targets is too low. This result is echoed again in panels (g) and (h) for Catalogue 4.

Panels (e) and (f) show that the lack of z-band photometry causes problems for objects with spectroscopic redshift $z > 1$, scattering the photometric redshift estimates mostly to higher redshifts. The inclusion of the IRAC bands really helps matters at these redshifts, where the $1.6\mu m$ bump passes between the 3.6 and $4.5\mu m$ filters. The scatter of redshift estimates in the range of interest is much reduced, indicated in the number densities also. Although the number density of potential targets is lower for the catalogue including the IRAC bands, these are more realistic, as the higher density in the former catalogue is most likely due to scatter into the redshift range.

For both catalogues 2 and 3, inclusion of the IRAC bands improves the spectroscopic redshift recovery in the absence of the z-band photometry.

3.3.3 Scenario three - Using the CFHTLS fields

Given the improvement in photometric redshift estimates when including the IRAC ch1 and ch2 data, how would a photometric redshift selection from the CFHTLS-Wide fields fare with the inclusion of this data. It is a possibility for these fields to be covered by a Spitzer warm mission in the future, reaching SWIRE depths. Given the large area of available data in the optical (summarised in Table 3.6), could this improve the selection efficiency?

The depths of each of the Wide fields are very similar to those given in the first artificial SWIRE catalogue and the results of photometric estimates from this catalogue without inclusion of the J and K-bands is summarised in Figure 3.13. The fraction of objects with the correct spectroscopic redshifts for the photometric redshift selection $1.4 < z_{phot} < 1.7$ are 19.3% and 38.6% for the catalogues without and with Spitzer photometry respectively. This shows that the Spitzer bands improve the photometric redshift estimates greatly in the range of interest.

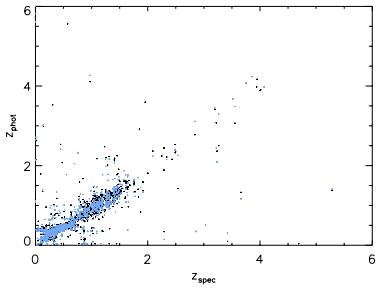

(a) Catalogue 1 - spectroscopic redshifts vs. photometric redshifts

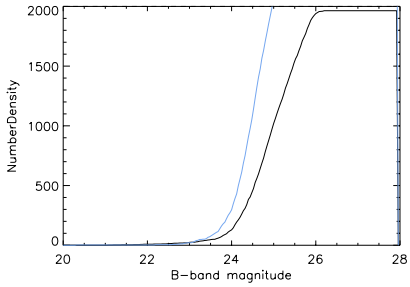

(b) Catalogue 1 - number density of sources at $1.4 < z_{phot} < 1.7$ with B-band density

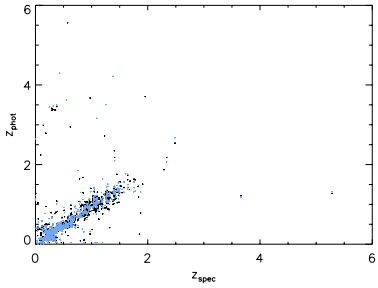

(c) Catalogue 2

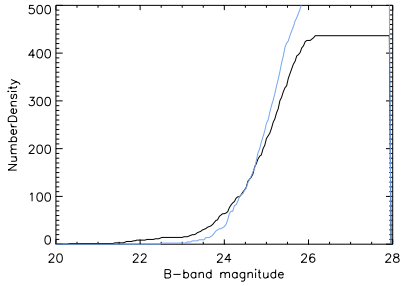

(d)

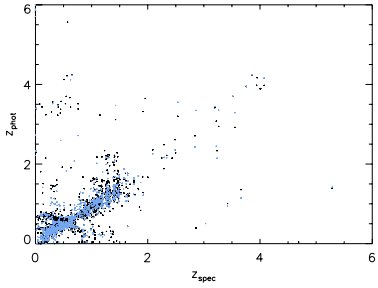

(e) Catalogue 3

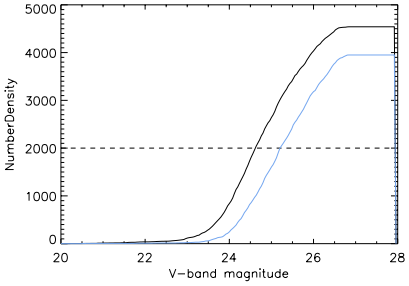

(f)

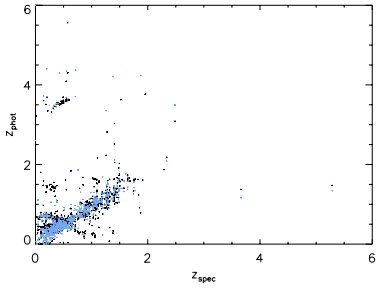

(g) Catalogue 4

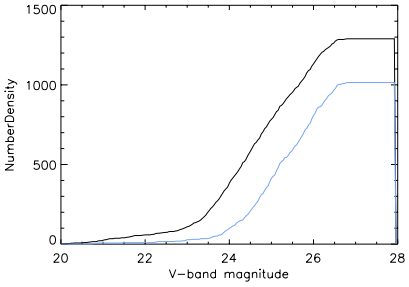

(h)

Figure 3.12: Left: The photometric redshift to spectroscopic redshift estimate comparison for different filter coverages and depths, as detailed in Table 3.4. Right: The corresponding surface density per square degree (number density) of sources with $1.4 < z_{phot} < 1.7$ plotted against B-band or V-band magnitudes, depending on the filter coverage in the catalogue. The blue points and lines refer to the results including IRAC photometry and the black points and lines display the results without using IRAC photometry.

Care has to be taken when looking at the number density of sources for this photometric redshift selection as the catalogue was selected from the K-band, not the z-band or i-band, where the selection might be made from for the actual fields. Plotting the number density against the z-band magnitude now shows that it rises steeply between 23 and 23.5 (AB), where it approximately reaches the ideal number density for beam-switched observations (Figure 3.13 (b)). With the 50% completeness for disc-type objects (rather than point sources) averaging at about 22.85 for the z-band, the actual number density at this magnitude is ~ 250 objects per square degree. The reason that the magnitudes of the objects in the catalogue extend to such faint limits is that they are only treated as non-detections when the magnitude errors reach 1.087 (1σ).

This demonstrates that, for targeting objects within the CFHTLS, photometric redshifts are greatly improved in the redshift range of interest by adding Spitzer IRAC data. Without this data, there are no anchor filters longwards of the 4000Å break to effectively select galaxies at $z \sim 1.5$. To select objects with photometric redshifts from this field, the z-band imaging needs to be deeper. If selecting from the z-band itself, the limiting magnitude needs to be at least 23.5 (AB) to provide a high enough number density of sources for targeting with FMOS.

Field	Filter Completeness									
	u		g		r		i		z	
	50% star	50% disc	50% star	50% disc	50% star	50% disc	50% star	50% disc	50% star	50% disc
W1	25.4	24.7	25.4	24.7	24.6	23.8	24.5	23.7	23.6	22.9
W2	25.4	24.7	25.4	24.7	24.8	24.0	24.5	23.7	23.7	22.9
W3	25.2	24.5	25.4	24.7	24.7	23.9	24.4	23.6	23.6	22.9
W4	25.3	24.6	25.4	24.7	24.5	23.7	24.5	23.7	23.6	22.8

Table 3.6: Limiting magnitudes in the CFHT filters for the different fields in the wide survey. The completeness values correspond to the mean values for 50% completeness for point sources and disc-like galaxies of the individual stacks contributing to the individual fields. The completeness for disk-like galaxies was estimated by taking galaxies from the image and varying their absolute scaling to provide a range of sizes and surface brightnesses representative of the objects in the field (http://www3.cadc-ccda.hia-iha.nrc-cnrc.gc.ca/community/CFHTLS-SG/docs/quality/photometry.html). Taken from the T0005 version release.

3.3.4 Discussion

When comparing photometric redshifts to colour selections, photometric redshifts produce better results, with the success rate of the BzK and Bz1 selections peaking at $\sim 20-25\%$.

When considering different target fields from which to draw the target population, I find that the depth and coverage afforded by SWIRE, for the regions with full depth in the UKIDSS-DXS image, and full set

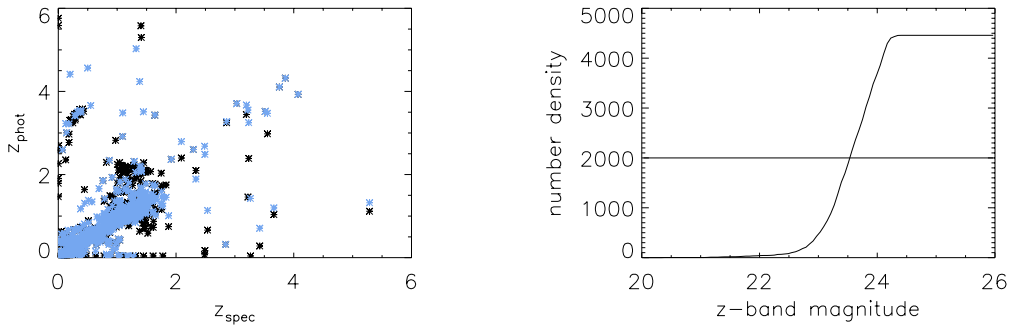

(a) (b)

Figure 3.13: (a) Comparison of photometric redshift estimates for similar filter coverage as in the CFHTLS field, with (blue points) and without (black points) Spitzer IRAC photometry. (b) Number density of sources in selected photometric redshift range for the catalogue including Spitzer photometry.

of optical filters, a success rate of photometric redshifts comparable to that afforded by the UDS is reached. Including Spitzer IRAC filters does not improve the photometric redshift estimates in this case. In the absence of the U/B-band and the z-band the IRAC bands do improve the photometric redshift estimates and a redshift success rate of $\sim 42\%$ is reached. This would allow the use of the Lockman hole field, which has no z-band imaging, though the selection mechanism for all fields should be consistent and so if this were the case then all fields should have targets selected without use of the z-band images.

Given the number density of sources from the catalogue with full K-band depth and full filter coverage reaches 1000 objects per square degree at a B-band magnitude of 25 (AB), an area of at least 60 square degrees would be required, assuming that half of these will give you a redshift in the correct range, which is optimistic given that the fraction of objects with emission line flux falling below the observable flux limit has not yet been truly modeled and accounted for. The SWIRE survey is therefore too small, though the wavelength coverage is good.

Looking at the CFHTLS survey, with the inclusion of IRAC ch1 and ch2 photometry a photometric redshift success rate of $\sim 38\%$ can be reached. Without deeper z-band data to select the catalogues from, however, the number density of sources is again too low.

These results rely on the assumption that the spectroscopic redshifts used for comparison to the photometric redshift estimates are representative of the population as a whole. The expected success (objects selected from a photometric redshift interval having their true spectroscopic redshift within the same in-

terval) will be dependent on the best-fitting model, this model-dependent photometric redshift quality is illustrated in Section 3.1.3. There is a large spectroscopic survey underway in the UDS field (P.I. O. Almaini), and results from this should help improve the testing of any photometric redshift estimates in this redshift range, as well as future redshifts obtained by FMOS in the UDS during GTO time scheduled in November 2010.

Chapter 4

FMOS Commissioning and Data Reduction

4.1 The Instrument

Near-infrared spectroscopy is plagued by the OH emission lines that dominate the sky background spectrum, as shown in Figure 4.1. In long-slit spectroscopy, nodding between observations allows near-complete subtraction of the sky, down to the poisson limit. For fibre spectroscopy, however, this accuracy is much tougher to achieve given the need to calibrate the differences between the individual fibres, at their observing positions. Incomplete sky-line subtraction distorts and sometimes prevents the observation of object emission lines that sit near by, especially when they are observed at a low resolution. Yet low resolution observations provide a wider wavelength range making redshift determinations based on multiple line detections more likely, and the ability to observe objects in a large redshift range. This is where FMOS' OH-suppression mirror comes in. Removing the OH-lines from the spectrum when it is focused at high resolution onto the mirror, the spectrum can then be re-dispersed back to lower resolution, providing a spectrum free from OH line contamination (Figure 4.1).

4.2 Observations

Two sets of observations were taken in the UDS field with FMOS, in October and December 2009. The observations were set up to include objects satisfying a number of different selection criteria. Within both observations, objects with known redshifts were observed as well as those selected from photometric red-

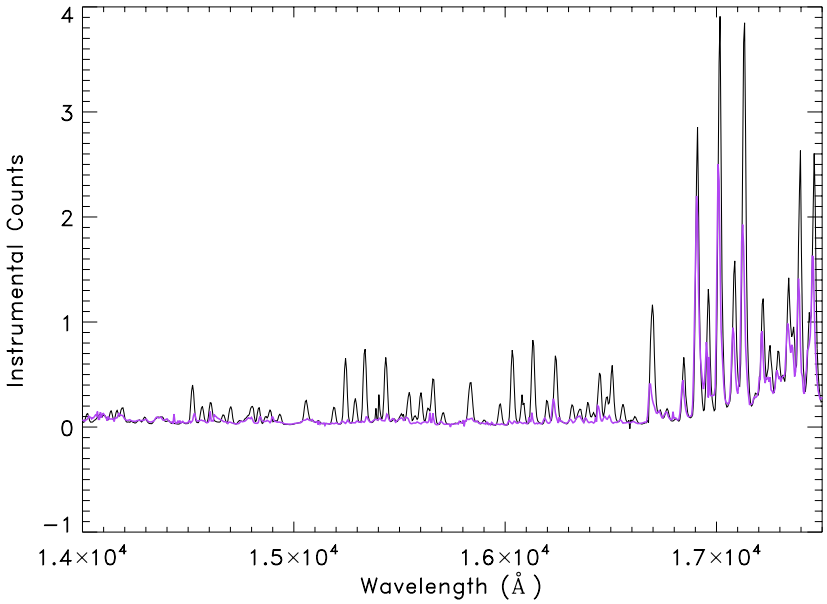

Figure 4.1: The sky spectra in the H-band showing the effects of the OH-suppression mask. The spectra are not flux calibrated and so are imprinted with the instrument response function. The black line shows a sky spectrum free from masking and the purple line shows a spectrum that is well masked at the low wavelength end, but only partially masked at the high wavelength end. These spectra were taken from the December IRS1 data-set, where the OH-suppression mask was still imperfectly aligned.

shifts, colour-colour cuts and narrow-band imaging. Those objects selected from narrow band imaging were a subset of objects detected by the High-Z Emission Line Survey (HiZELS, Best et al. (2010)).

Both sets of observations were taken with beam switching (described below) with a total of 2 hours on source in October (4 hours total) and 1.5 hours in December (3 hours total). IRS1 was employed in low-res mode for both sets of observations, while IRS2 was used in high-res mode, in the fourth position, allowing observations of the far-wavelength region of the H-band, in October and low-res in December.

The IRS2 observations in October were taken with one of the shutters (between camera and spectrograph) closed resulting in the throughput being halved. This was due to a need for a mechanical tilt to be applied to the grating inside the spectrograph to be able to align the sky spectrum with the mask. The grating is actually a mosaic of four smaller gratings, each of which can be tilted independently. At this observation run, two of these gratings could be aligned to the mask without tilting the full mosaic but two were limited in their motion and so the shutter was closed to cut out the light from these to gratings.

During these observations the OH-suppression mask was not perfectly aligned to the sky spectrum for

either spectrograph, and so sky subtraction is the limiting factor in the reduction of the data obtained. Also, there were problems in tracking the positions of the objects within the telescope focal plane, as they were found to vary gradually with time. This problem was identified from the October observations, where the fibres where gradually moving off source, rendering 2 of the frames un-usable. The total, on-source, integration time obtained in October was therefore reduced to 1.5 hours, with signal gradually decreasing between each fibre re-configuration (after 4 object plus sky frame pairs). This problem is due to a misalignment between the FMOS wide-field corrector and the telescope axis, and requires re-configuration of the field every 30 minutes, so with the December observations, this was performed after every beam-switched (15 minutes object plus 15 minutes sky) pair of frames.

4.2.1 Observing Modes

There are three observing modes that can be employed for any given observation; beam switch, cross-beam switch and point and stare. They are used for different methods of sky subtraction. A short description of each is given below:

- **Point and Stare -** With this mode, a certain number of fibres are dedicated to empty patches of sky (10-20%) distributed throughout the field. The rest of the fibres are allocated to objects, with a few centered on stars used for calibration and telluric corrections.

- **Beam Switching -** In this mode, all of the fibres can be dedicated to objects and calibration sources. The observations are then taken with a telescope nod, alternatively placing the fibres on empty sky and then on source. Successive frames can then be used for sky subtraction for sky emission has then passed through the same light path as that of the object. This method, however, halves the total integration time on-source. The sky measurements are also not con-current with the object measurements, and so the sky emission will vary within the object and sky frames.

- **Cross-Beam Switching -** For this mode the fibres are configured such that two fibres are allocated to each object. The telescope again nods between frames but one of the two fibres is always on-source, while the other fibre is allocated to sky. This mode allows the total integration time to be used on source but halves the number of objects that can be viewed in one configuration.

4.2.2 Fibre Configuration

Spine-to-Object (S2O) software is available from the FMOS website [1]. This software requires a list of science objects, with positions, apparent magnitude in R, and a priority. Objects fainter than $\sim$16 mag were observed, as bright objects leave ghost features on the detector, affecting other spectra. The software also requires a list guide stars that are bright in R (around 12-16 mag) that are on the same astrometric system as the science targets. These stars are centred on the guide fibre bundles (Figure 4.2) to the sides of the field and it is optimal to have stars allocated to guide fibres at each corner. Coordinate calibration stars of similar brightness to the guide stars are required throughout the field to correct for field rotation during the observations. Finally, stars for flux calibration and telluric correction should be included. These are allocated fibres and observed at the same time as the science objects. F, G and early K-type stars are numerous enough to be found in most target fields and can be selected from their near-infrared colours.

The software assigns fibres to the science objects and flux calibrator stars and guide fibres to the guide stars, given a field centre. Figure 4.2 shows the fibre configuration used in the October observations. The file output from the allocation software is used by echidna to align the spines to the correct positions within the focal plane for observations.

4.3 Data Reduction

The data obtained during commissioning was reduced by hand using the IRAF package APEXTRACT and custom written IDL procedures. The steps detailed in this section are common to the reduction of any fibre-fed spectroscopy. The studies performed with the precursor instrument to FMOS, CIRPASS (the Cambridge Infra-Red PAnoramic Survey Spectrograph) display these steps (Doherty et al., 2004, 2006). FMOS data, however, requires special treatment in how some of these steps are carried out.

The reduction process detailed below is for Beam-switched data and used to reduce the spectra acquired within the UDS field in October and December 2009.

4.3.1 Calibration Frames

The different calibration frames taken with each set of observations are as follows:

[1] http://www.naoj.org/Observing/Instruments/FMOS/

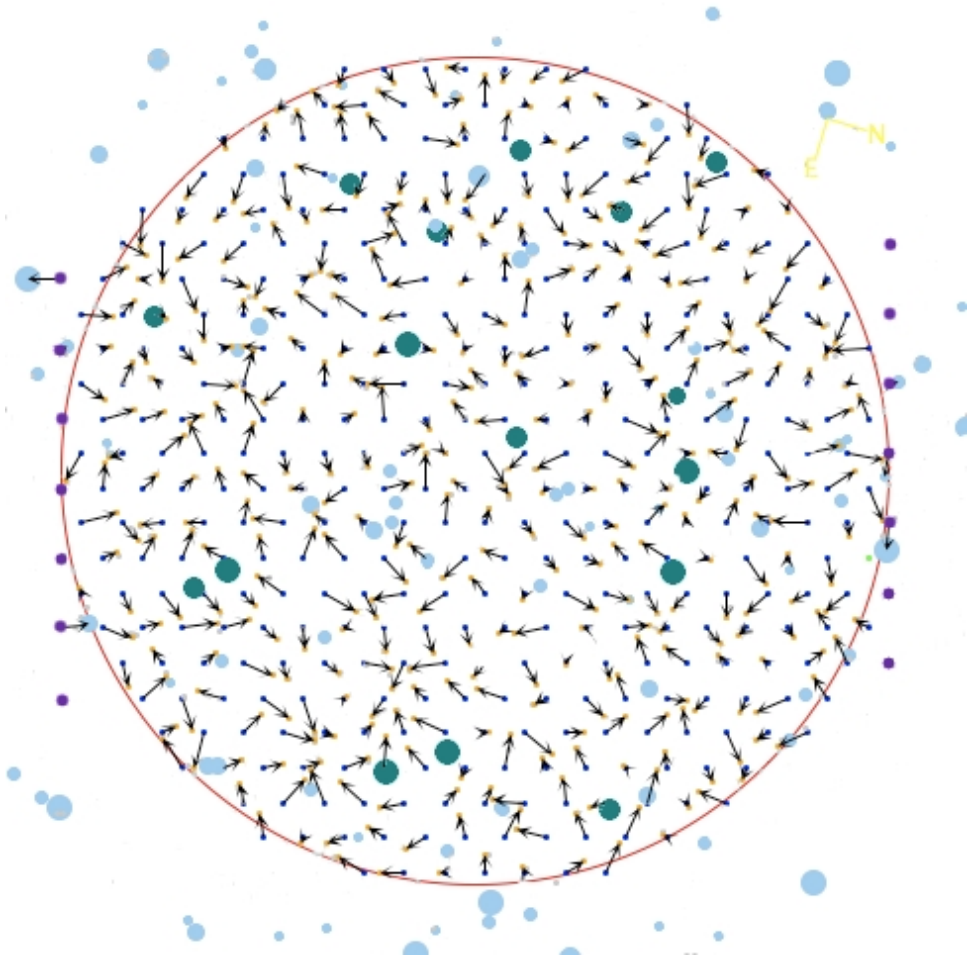

Figure 4.2: An example fibre configuration for the UDS field observed in October 2009. The red circle encompasses the FMOS field of view, the purple points either side of the field of view show the guide fibre bundles and the navy blue points within the circle show the positions of the fibres. The arrows indicate the direction of movement of the spines to reach the allocated object (yellow points). The light blue points are guide stars throughout the field and the dark green points are the calibration stars.

- Multiple flat-field images with the fibres illuminated by the dome-flat lamp, with accompanying frames taken with the lamp off to remove any dark current and scattered light not associated with the lamp. Multiple images are required to produce high signal-to-noise observations without saturating the detector pixels. These flat-field exposures should be taken with the fibres in their observation configuration to provide accurate fibre-to-fibre throughput calibration. This is because the flux collected by the fibre is a function of fibre angle and distance from the field centre. For both the October and December observations, these frames were taken with the fibres in their home position, however, and this has to be taken into account in the later flux calibration stages.

- Multiple arc calibration images, taken using a Th/Ar lamp for wavelength calibration.

A master dark is also available for IRS1, produced using multiple exposures, allowing the structure of the dark current to be removed from the individual frames, with suitable scaling to the observed integration time. This is not yet available for IRS2 since there is, at present a detector reset anomaly with non-repeated, non-linear behaviour of the detector pixel values at the beginning of a frame. Any dark frames must therefore be observed with the same integration time as that employed on source.

4.3.2 Dark subtraction

The detectors used in FMOS suffer from a high dark current that must be subtracted from the science frames. When using beam-switching, this can be done using the sky images as they are taken with the same exposure time. This method was used for both the IRS1 and IRS2 data presented here.

4.3.3 Bad Pixel Masks and Cosmic Ray removal

Pixels contaminated by cosmic rays were detected by comparing pixel values between the different images in an exposure sequence. Care was taken to ensure that the images being compared were either all sky frames or all object frames. This prevents any high pixels due to object flux being masked. A mean value and standard deviation was calculated for each pixel and if any single pixel in the different images was found to have a value greater than 1.5 times that mean, it was masked as a cosmic ray. This value was chosen to prevent masking within bright sky lines showing variation in flux between the different exposures.

This method performs significantly better than using LACOSMIC on these particular images since it uses information from multiple exposures on a pixel-by-pixel basis whereas LACOSMIC has to be tuned to work on the particular image which either resulted in too few detections or masking of sky lines.

4.3.4 Combining Frames

Individual object frames are combined using a weighting determined from the signal-to-noise present in the brighter calibration stars. This is necessary to correct for changes in seeing but more importantly in the October data set, to correct for loss in flux due to the object positions moving within the focal plane, away from the fibre positions. Each sky frame is weighted according to the weighting of its corresponding object frame to ensure optimal sky subtraction. The combined sky frame is then subtracted from the combined object frame.

4.3.5 Define apertures

Apertures are defined for each fibre from the flat-field image, using the APFIND and APEDIT tasks. The flat field image shows the positions of the individual spectra (Figure 4.3), and their shape across the detector, as well as the throughput variations from the fibres (from fibre-to-fibre and across the cross-section).

APFIND traces the shape of the spectra for each individual fibre in the dispersion direction by following the peak in the flux at the centre of the fibre trace at points across the detector. These points are then fit to with a chosen function. The extent of the spectrum for each fibre is then determined by fitting to the fibre profile in the spatial direction (vertical in Figure 4.3).

The shape of the trace is best fit with a fifth order chebyshev polynomial. The J and H-band mask mirrors were not always in exact alignment and so to aid the tracing of the apertures, one side of the image would be shifted in the spatial direction to improve the alignment on the image. The gap between the mirrors also hinders the tracing of the apertures, so this was filled using a section of the image with visible apertures. Figure 4.3 shows how the flat field has been adjusted to best define the individual apertures.

Each image from the observing sequence is treated in the same way before extraction of the spectra.

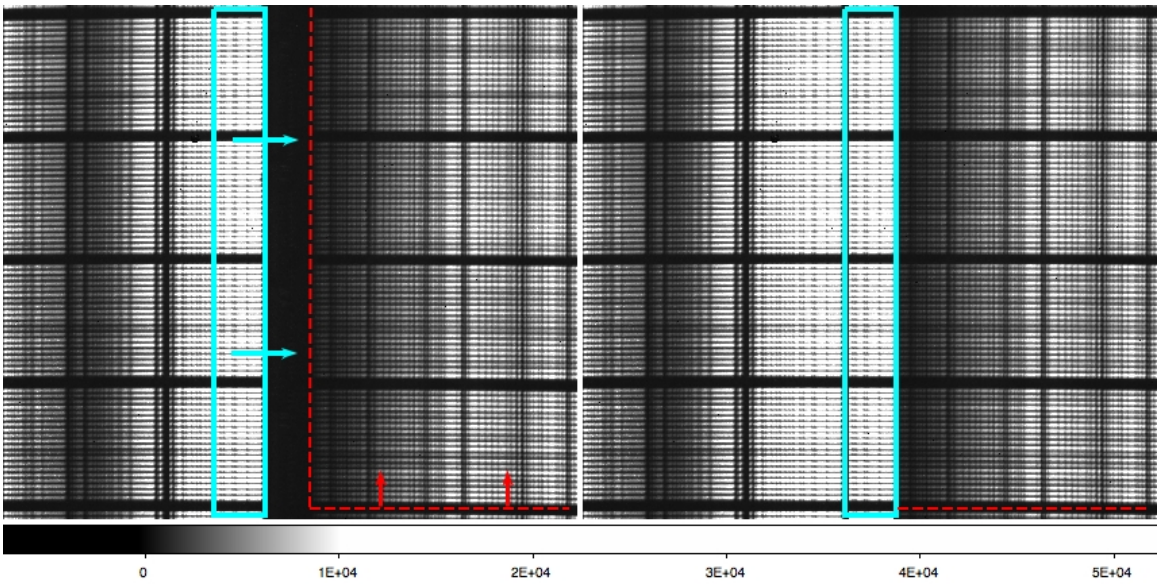

Figure 4.3: A section of the IRS1 flat-field image showing the alterations made to enable extraction of the apertures. The left hand side shows the image before alterations, and the right hand side shows the resultant image used to define the apertures. The blue box shows where a section of the flat field image was copied from to fill in the gap in the image between the two mirrors and the red dashed line and arrows show how the right hand side has been shifted upwards by three pixels to align the apertures either side of the gap.

4.3.6 Flat-fielding

Flat-fielding FMOS images requires careful treatment of the masked regions as well as regions inbetween the fibre traces. The flat can only be used to correct pixel-to-pixel variations in sensitivity in regions where the flat field image is bright enough and the poisson noise dominates over the noise from the detector dark current. One also has to be careful to remove the shape of the fibre profile in the spatial direction.

Since the spectra follow a curved path across the detector and adjacent spectra are quite close to each other (as can be seen in figure 4.3), a straightened version of the flat field spectra was used to normalise the flat. When extracting the spectra there are two options for the form of the output from the apextract package; multispec and strip. The multispec output provides a one-dimensional spectrum for each of the apertures and plots them row by row in an image whereas the strip output provides a two-dimensional, straightened spectrum for each aperture.

Each two-dimensional flat field spectrum is then normalised according to the following steps:

- A 2-degree polynomial is fitted to the average of two columns, ignoring any masked pixels in the fit

(so that any bad pixels do not skew the fit). Only two columns were averaged so as not to average over the mask features. The column is then divided by the fitted polynomial.

- Any pixels with flux less than 10% of the mean flux were set to 1 along with the bottom and top rows.
- The biweight mean for each row, for any pixels above the flux limit, is required to be 1. This removes any residual shape in the spatial direction.

To fix pixel-to-pixel variations in the science images, each spectrum needs to first be extracted to this straightened two-dimensional form before dividing by the appropriate flat.

4.3.7 Spectrum Extraction

The profile shape of the fibre spectra is fit using a Gaussian across the dispersion direction. This profile shape is then used to weight the rows according to their S/N defined by the Gaussian shape of the profile, before summing each column, producing a 1D spectrum. Any binning of the spectra in the dispersion direction is performed at this stage, so that each pixel in the binned 1D spectrum is a weighted average of all the column pixels that contribute.

4.3.8 Wavelength Calibration

At the beginning of each night, a set of wavelength calibration frames are taken using a Th/Ar lamp. A set of frames is also taken with the calibration lamp off. These two sets are combined separately and the dark frames subtracted from the calibration frames before the spectra are extracted and flat-fielded, as for the science data. The wavelength solution is then found using the IRAF tasks IDENTIFY and REIDENTIFY for the 1D spectra, assigning wavelengths to the emission lines observed from known line lists. This solution is then used to resample the 1D spectra in the dispersion direction onto pixels that are constant size in wavelength using DISPCOR.

4.3.9 The Fibre Flat

The transmission varies from fibre-to-fibre, with a possible wavelength dependency and this must be corrected in order to be able to accurately flux calibrate the spectra. These differences in fibre transmission

stem from slight intrinsic physical differences, slight misalignment and differences in fibre tensions. The largest variable effect is the light lost due to non-telecentricity of the fibre axis as the spines are tilted away from their home positions (up to 15% light loss at the maximum offset angle). To first order the variation can be removed by using a dome flat, with the fibres configured at the positions that they will occupy during observations. As noted above, the fibres were, in fact configured to their home positions when taking the dome flats in the October and December observing runs. This limits the accuracy to which these fibre-fibre variations can be corrected for and also the accuracy of the later flux calibration stages.

The average response of the instrument plus spectral shape of the flat lamp are first removed by fitting a high order polynomial to an average of the wavelength calibrated, extracted 1D spectra. This was done using the IRAF task RESPONSE as the task allows the user to interactively delete points from the fit. The points corresponding to dips in the transmission where the spectra are masked are not used in the fit. This polynomial fit is then divided through the extracted flat field spectra before fitting a spline to each individual spectrum. For this step, the mask features have been masked by eye and are again not used in the fit.

The final extracted spectra are then divided through by these fits to remove the fibre-to-fibre throughput variations, where the variations are allowed to vary with wavelength. Figure 4.4 shows the result of the correction of the throughput variations applied to the flat-field image itself.

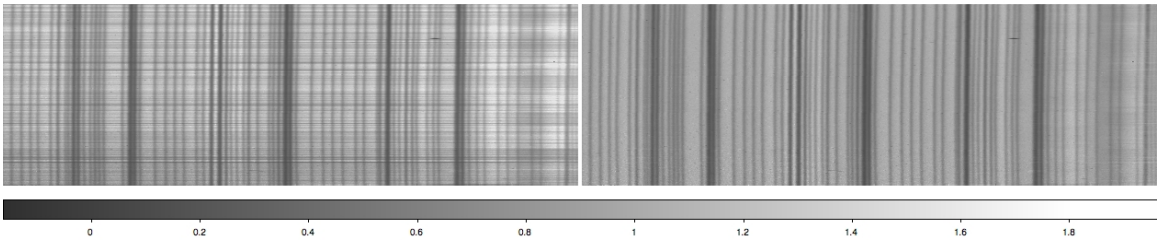

Figure 4.4: This shows a section of the fibre-flat image, each row is a different extracted 1D spectrum. The left-hand side shows the extracted dome flat before correcting for fibre-fibre throughput variations, and the right-hand image shows the result of these corrections, applied as described in the text.

4.3.10 Sky Subtraction

To first order, sky is subtracted by combining the object and sky frames separately before subtracting the sky frame from the object frame. For the long exposures (15 minutes) used on both sky and object, this subtraction is not optimal, as the sky emission is varying with time. The residual sky is removed in these

frames by taking a modal value at each wavelength from a number of the spectra and subtracting it from the observations. This is a similar method to that of producing a master sky spectrum from a subset of dedicated sky fibres, with the difference that object fibres are also used and the modal estimation employed to reject object flux.

This approach is used since the mask was not yet aligned with the sky OH-lines during these observing runs. This produces the unfortunate circumstance of the lines being clipped by the mask, to varying degrees, so the shape of the lines and the flux within the lines are not constant from fibre-to-fibre. This makes a scaling of a master-sky spectrum, averaged from many fibres, to the sky emission in individual fibres, impossible. It also means that, to follow the shape of the lines, the modal sky spectrum can only be estimated from a few adjacent fibres.

For the rest of the data presented here, 6 adjacent fibres were used to produce the modal sky estimate, rejecting any bright continuum sources of adjacent objects known to have very similar redshifts (eg. HiZELS objects, see Chapter 5).

The problem of accurate sky subtraction is one further discussed at the end of this chapter.

4.3.11 Flux Calibration and Atmospheric Absorption correction

The spectra need to then be corrected for the instrument throughput and atmospheric absorption before being flux calibrated. For each observation, stars are chosen and assigned fibres within the field of view. These stars are chosen to have colours representative of F, G and early K type stars as these spectral types are numerous and likely to be found within an FMOS pointing. They also have fairly featureless spectral shapes.

The Infrared Telescope Facility (IRTF) spectral library (Rayner et al., 2009) is a library of 210 cool stars observed in the wavelength range 0.8 to 5μm. Rayner et al. (2009) use the flux calibrated spectra to provide synthetic WFCAM J-H and H-K colours. For the data taken from the UDS field, the stellar photometry is compared to the library of spectral colours and a best-fitting spectral type chosen to represent that star. The steps are then to essentially fit to the shape of the star in the un-calibrated spectrum and divide the other spectra through by this shape. The spectra are then multiplied by the expected spectral shape derived from the best-fitting spectrum in the library.

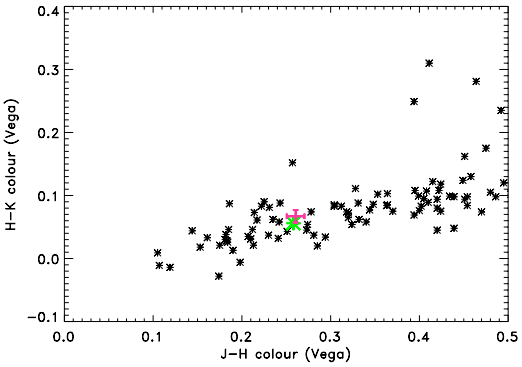

(a) Colour-Colour plot of the stars in the IRTF spectral library with the colours of the observed star plotted in pink, and the chosen library star plotted in green.

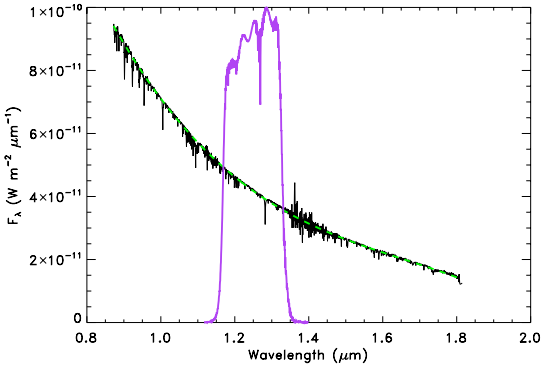

(b) The flux calibrated spectrum of the chosen library star with a fit to the continuum overplotted in green and the UKIDSS J-band filter response curve overplotted in purple.

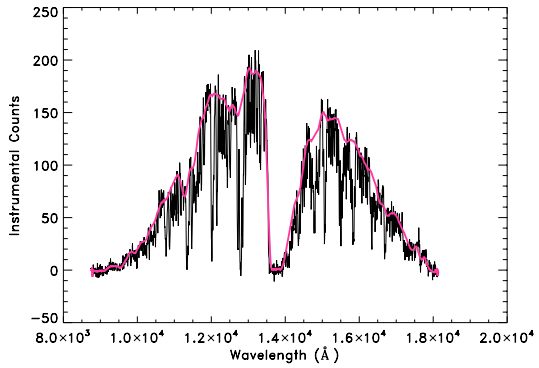

(c) The observed star to be used for flux calibration with the fitted shape over-plotted in pink.

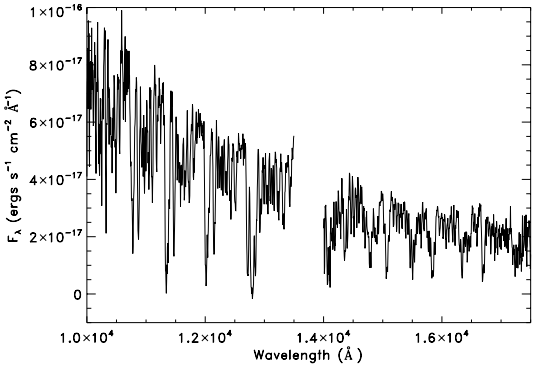

(d) The final flux calibrated stellar spectrum. The gap is at the position of the slit.

Figure 4.5: The different stages involved in flux calibration. First the J-H, H-K colours of the observed calibrator star are compared to the colours of the stars in the IRTF spectral library (a) and the star closest in colour is chosen to represent the true spectral shape of the star (b). The shape of the stellar continuum is fitted to in the library spectrum (b). The observed stellar spectral shape is also fitted to (c) being careful to use only sections where the mask is not cutting out the light. This shape is divided through the rest of the spectra to remove the atmospheric absorption features and the instrumental response function. The spectra are all then multiplied by the library spectral fit (b) and scaled according to the J-band magnitude of the observed star and that of the spectral fit when convolved with the J-band response curve. The resulting, flux-calibrated spectrum of the chosen star is shown in (d).

When dividing the spectra through by the observed spectral shape, the shape of the instrument throughput and any atmospheric absorption is being removed from the spectra. The mask features are also visible in the stellar spectrum, however, and have to be treated carefully. These features can clearly be seen in figure 4.5(c). This figure also demonstrates the possible difficulties in knowing what is a feature that needs to be removed and what is just due to the mask (for example, the dip visible at $\sim$15300 Å is due to a region with closely packed mask features and should not be fitted to, whereas the dip at $\sim$11000Å is due to atmospheric absorption). With data for which the mask is perfectly aligned, the mask line list can be used to define regions to exclude when fitting to the overall shape, but for this data the positions of the mask features were determined from the wavelength calibrated flat-field data. The pink line in figure 4.5(c) shows the spline fit to the data not influenced by the mask features.

Once the data has been divided through by the fitted stellar shape, they must then be multiplied by the expected shape of the spectrum. This is taken to be the shape of the star in the spectral library that is closest in J-H, H-K colour-colour space. The shape of this spectrum also has to be fitted to, to remove intrinsic absorption features present due to neutral hydrogen and metals. Any of these features present in the observed stellar spectrum have not been fitted to, as the scale of the features is similar to that of the mask features. Also the strength of the absorption can differ from star to star of the same spectral type due to differences in metallicity and temperature so be would unlikely to match between the library spectrum and the observed stellar spectrum. Figure 4.5(b) shows the spectrum of the chosen library star for that observation and the fitted shape over-plotted in green.

The final stage in the flux calibration is to scale the magnitude of the model spectrum to match that of the star in the WFCAM J-band filter. The final flux calibrated spectrum is shown in 4.5(d).

4.4 Noise Estimates

The noise in the spectra is estimated from the original frames, finding an estimate for the noise in the dark current from the empty region between the mirrors, and adding this in quadrature to the Poisson noise in the photon counts (using the FMOS gain of 2.5 counts per electron). This noise estimate is then propagated through each stage in the reduction process to produce variance spectra accompanying the 1D spectra. This method over-estimates the noise in faint objects as the noise in the dark-current is determined before flat-

fielding removes pixel-to-pixel variations.

4.5 Optimal Sky-Subtraction

The observing mode chosen makes a big difference to the quality of sky-subtraction achieved as well as the number of objects observable within a night. For a large redshift survey the ideal scenario would use the point-and-stare observing mode, allowing 80% of the fibres on-source and more fields observable in a night, given 1 hour integration times per configuration.

Sharp & Parkinson (2010) show that, with standard point and stare sky subtraction, the noise reaches floor due to systematics, preventing stacking analysis for fainter sources. Although we are not worried about long integration times for a redshift survey, sky subtraction residuals will still hamper the assignment of redshifts to fainter sources. The PCA (Principle Component Analysis) method of sky subtraction allows good sky subtraction with the point and stare approach. At the moment it is not possible to test the method properly due to the mis-alignment of the OH-suppression mask, which changes the shape of the sky-lines in a systematic way as the mask feature passes over them. One way to produce the PCA eigenvectors for such data would be to use many frames and find a set of eigenvectors for each fibre, or a group of only a few adjacent fibres, so that the shape of the sky lines are not varying within each template set due to instrumental effects.

Principal component analysis decomposes a set of possibly correlated variables into a set of uncorrelated, or orthogonal variables, or eigenvectors. In the case of modeling the sky emission, the algorithm finds the pixels that vary with intensity from frame to frame and essentially group them together according to whether they vary in the same way as other pixels. If you have one sky line, for example, covering a few pixels, these pixels will all vary with intensity by the same amounts and will all contribute to the same eigenvector. Since separate OH-line intensities vary to differing amounts, these variations will provide contributions to different eigenvectors. The algorithm decomposes the spectra into a finite number of eigenvectors, which is not a complete set, but higher order variations tend to be fitting to the noise, and can generally be left out.

Once the OH-mask is aligned, however, the problem of sky-line residuals is mostly solved and this method still requires the background continuum to be subtracted off first. Clean subtraction of the continuum requires accurate calibration of wavelength-dependent fibre:fibre throughput differences and this will likely

be the limiting factor for any future long exposures /stacking analysis to be performed with FMOS spectra in the future, regardless of the use of PCA sky subtraction.

Chapter 5

Spectra of objects in the UKIDSS-UDS

5.1 Performance

5.1.1 Testing Flux Calibration

When performing the flux calibration (Section 4.3.11), the stellar spectrum is scaled from the integrated spectral flux obtained through the WFCAM J-band filter (estimated from the model stellar spectrum, to avoid the effect of mask features) to the photometry within a 2" diameter aperture, from the images convolved to 1" seeing. This scaling should produce consistent fluxes for spectra of other point-source objects with visible continuum. To test the consistency of the flux calibration from object to object, the flux obtained from the flux-calibrated spectra through the J-band filter are compared to the catalogue photometry, separately for the December and October observations, and the results displayed in Figure 5.1.

Two different estimates are given for the magnitude of the spectrum within the J-band filter. One estimate is taken directly from the observed spectrum, convolved with the filter profile (blue points) and one is taken from a spline fitted to the spectral shape (pink points). The shape was fitted in the same way as at the flux calibration stage, where only points not affected by the mask are used as contol points for the spline. Error bars given to the continuum flux measurements taken directly from the spectrum are estimated using the noise values propagated through the pipeline (Section 4.4). These underestimate systematic errors due to imperfect sky subtraction for the fainter sources.

These plots show that the flux calibration is much more stable in the data taken in December (5.1(b)),

where the point source continuum magnitudes show an average deviation from the photometric magnitudes (from continuum fit) of 0.16 or an average flux difference of $\pm 14\%$. In October, however, these fluxes are only consistent to $\pm 20\%$. This is most likely due to the problems with fibre positioning experienced in the October engineering run (see section 4.2). Between each fibre re-configuration (every 4 science plus sky frame pairs) the object positions in the focal plane were slowly changing and the fibres losing object flux by differing amounts depending on their position within the field. Although, when combining the frames they were weighted to take account of the loss of flux from the bright stars in the frame, this cannot correct for any positional dependencies in the loss of flux from other objects.

The accuracy achieved with the data taken in December is consistent with expected flux losses due to fibre tilt. The flat field frames for both these data sets were taken with the fibres in home position, whereas when they are configured to the field layout, each fibre is tilted, which causes a move of the fibre away from the focal plane, resulting in a loss of efficiency in collecting radiation. This effect also depends on the position of the fibre with respect to the centre of the field due to non-telecentricity. This effect also varies with wavelength.

These effects where simulated in Gillingham et. al., (2004) for fibre angles pointing radially towards or away from the centre of the field. An estimate of the fibre collection efficiency due to this effect is included in the spine to object software available from the FMOS website[1]. Using this efficiency as a correction factor to the fibre fluxes reduced the average flux difference to $\pm 11\%$, with the brightest three sources being on average 7% too bright. For each of these sources, the fitted continuum-derived flux and observed spectrum-derived flux bracket the photometric value. The remaining inconsistency between derived flux measurements could be due to the wavelength dependence of the fibre efficiency, and differences in seeing. It is clearly necessary to take the flat-field images when the fibres are in their field configuration, to take account of all of these effects. Applying the same corrections to the October data did not improve the flux calibration, indicating that the spine positioning errors are dominating the accuracy in the flux calibration of this data set.

The flux measurements from the spectra for the non-point sources tend to be fainter than the photometry. This is as expected, since the scaling assumes a point source with 1" FWHM seeing. The photometric aperture is larger than the fibre aperture (1.2" diameter on sky) so, for a source profile flatter than that of a

[1] http://www.naoj.org/Observing/Instruments/FMOS/

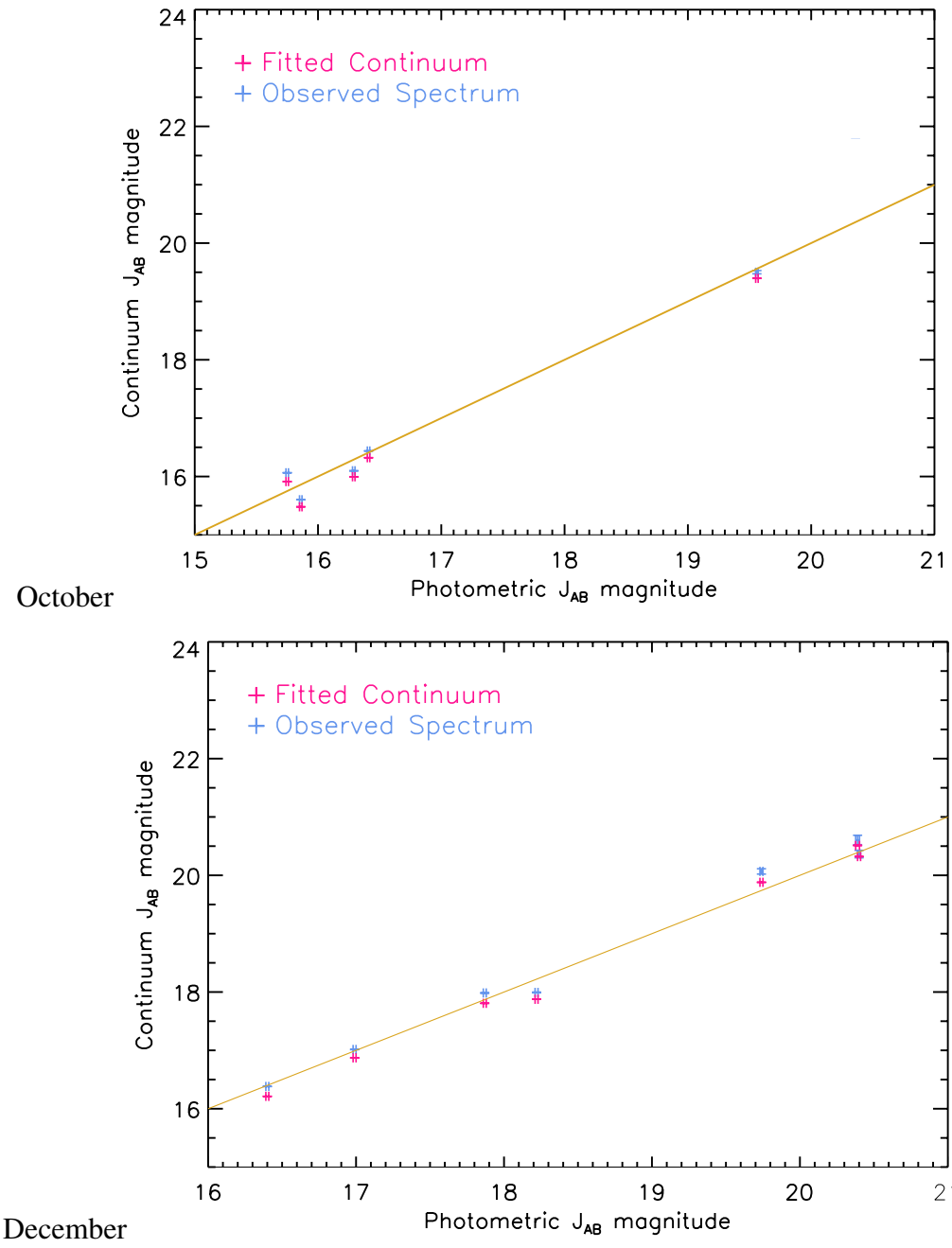

Figure 5.1: Testing the flux calibration. Comparison of continuum magnitudes through the J-band filter for flux calibrated data with the UKIDSS broad-band photometry

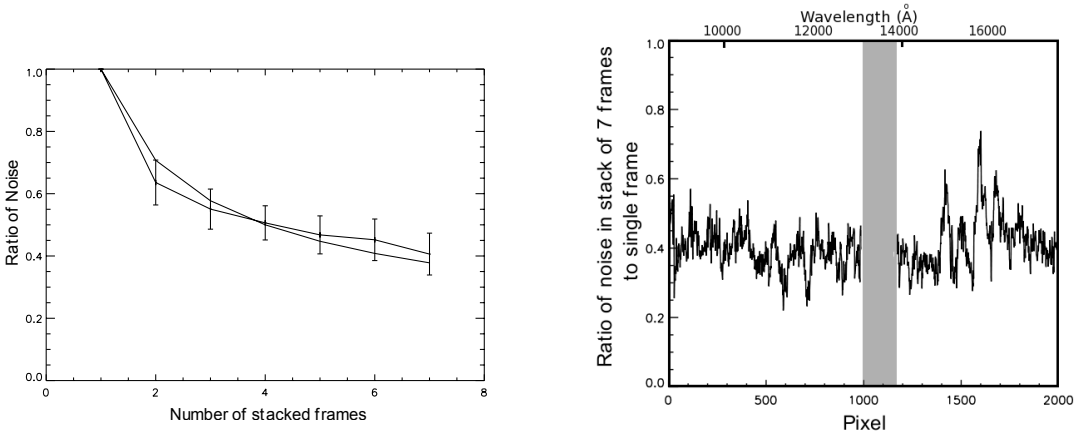

Figure 5.2: The decrease in noise, averaged for all the spectra, with stacking of individual frames (a) compared to the Poisson-limited case and (b) for the stack of 7 frames, how the noise has decreased as a function of pixel number/wavelength. The shaded region corresponds to the region occupied by the slit.

point source, the fraction of flux in the photometric aperture to the fibre aperture will be larger.

5.1.2 Noise

Figure 5.2 shows the average noise decrease for the number of averaged frames compared with the Poisson-limited case for the data taken with IRS1 in December 2009. This is measured taking the average noise in each stacked frame (with number of frames contributing to each stack varying), measured directly from the spectra as the standard-deviation of the clipped distribution per pixel. The average noise is divided by the measured noise from the single frame and the points and errors in Figure 5.2 (a) are the mode and standard deviation, respectively for the values of all of the pixels. This shows that on average the frames seem to be following the Poisson-limited case, with the noise decreasing with the square root of the number of frames contributing to the stack, though there is evidence that a floor is being reached at which the systematics are dominating, since the relationship is starting to flatten off at a stack of about 4 frames.

The behavior of the noise is strongly dependent on the wavelength, as shown in panel (b) of Figure 5.2. This panel shows the ratio of noise in the stack of 7 frames to the single frame. The wavelength increases with pixel number. It can be seen that, in some regions the ratio is as high as 0.7, these regions correspond to regions affected by sky lines. It should be noted that this effect is also dependent on where the spectrum sits on the mask (as to how well the sky lines are masked), since this is an average for all of the spectra.

What this indicates is that for certain regions of the spectra, the noise is approaching the Poisson limit,

but that the mis-alignment of the mask creates large systematic residuals at the sky-subtraction stage, indicating a need for either a larger training set for any PCA analysis to track the change in shape of the sky-lines as the mask cuts across them, or true alignment of the mask. These regions with very high sky-line residuals will hamper the detection of true emission lines.

5.2 Targeting HiZELS with FMOS

Targets from the High-Z Emission Line Survey (HiZELS) were included in the source list for both sets of observations. In October, only objects detected in the HiZELS NB_H filter were observed (nbH objects). This filter has a central wavelength of 1.619μm (Best et al., 2010) and observes Hα emission in galaxies at $z \sim 1.47$. This puts the Hα line near the middle of the FMOS H-band mask, and the Hβ and [OIII] lines within the J-band, allowing secure, multiple-line redshifts of these objects.

As discussed in Section 4.2, IRS2 was employed in high-res mode during the October observations, with half-throughput (. As such only IRS1 observations are summarised below. In December, 7 nbH objects were observed, 4 in IRS1 and 3 in IRS2 as well as 20 nbJ (selected from the NB_J filter) objects (9 in IRS1, 11 in IRS2) and 3 H2S1 (selected from the H_2(S1) filter) objects.

HiZELS objects provide a valuable input sample for testing the capabilities of FMOS, and FMOS provides valuable spectroscopic follow-up of these narrow-band selected objects.

The objects observed with IRS1 have had a higher success rate for detections due to the lower thermal background. The main factors contributing to the success rate of detections are; the quality of the sky subtraction and alignment of the OH-suppression mask. The HiZELS NB_J filter sits within a relatively heavily masked region of the mask (Figure 5.3 (a)). With the mask imperfectly aligned, a non-detection is most likely due to poor sky subtraction in this region and from the Hα being partially masked.

The most secure detection of Hα within the HiZELS sample is for nbJ-38031 (Table 5.1, Figure, 5.6) which gives a spectroscopic redshift of 0.855, placing Hα right at the long wavelength end of the NB_J filter.

The objects observed in October gave better results, with 8 of the 13 objects yielding a possible redshift, a few of which are shown in Figure 5.4.

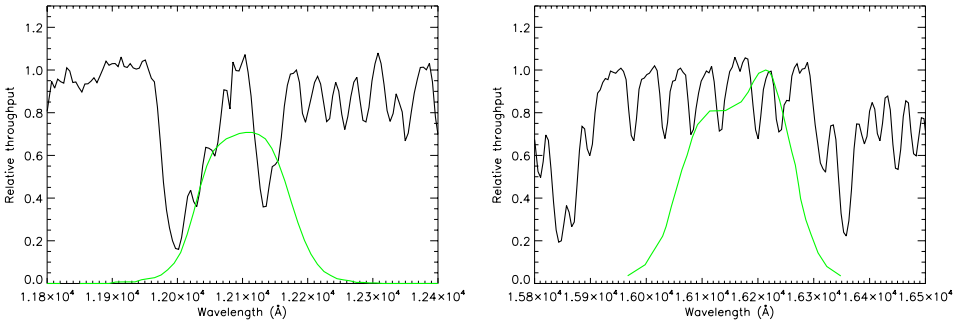

(a) NB_J filter (b) NB_H filter

Figure 5.3: The HiZELS narrow band filters plotted in green with the relative throughput of the OH-suppression mask over-plotted for low-resolution mode

Date	Spectrograph	HiZELS ID	Spec number	Hα Flux	photo-z	spec-z	quality	observed lines
Oct09	IRS1	nbH-2	21	2.986E-16	1.64	1.496±0.001	5	Hα, NII, SII, masked OIII? Evidence of broadening - AGN
		nbH-10	24	1.261E-16	1.43	1.468±0.001	3	Hα, Hβ, OIII?
		nbH-15	45	5.879E-17	1.41	1.495±0.01	2	Hα, possible OIII, Hβ
		nbH-44	81	5.386E-17	1.45	1.446±0.001	2	possible sky line residuals at Hα
		nbH-32	102	1.807E-16	1.41	1.453±0.001	5	good Hα, OIII, and Hβ
		nbH-22	116	8.735E-17	1.46	1.465±0.001	1	possible Hα
		nbH-1	119	2.588E-16	1.43	1.46±0.001	3	bright Hα, possible OIII, Hβ
		nbH-19	121	9.499E-17	1.42			
		nbH-26	123	1.087E-16	1.47			
		nbH-21	130	1.283E-16	1.45	1.47±0.001	2	bright Hα but mask at Hβ
		nbH-23	148	1.881E-16	1.4			
		nbH-29	151	1.096E-16	1.47			
		nbH-58	162		1.41			
Dec09	IRS1	H2S1-23386	1	8.0856E-17	2.42			
		nbH-2	34		1.64	1.496±0.001	5	good Hα, OIII, Hβ, agrees with Oct09
		nbJ-34230	59	1.21945E-16	0.8			
		nbJ-55723	109	1.7902E-16	0.82	0.847±0.002	2	
		nbJ-38031	132	2.6403E-16	0.85	0.855±0.001	5	bright Hα, NII
		nbJ-42400	134	8.5524E-17	0.85			
		nbH-55	142	1.145E-16	1.41			
		nbJ-56083	144	3.0758E-16	0.8	0.83±0.001	1	poor sky subtraction, line under mask feature
		nbJ-58281	146	1.9562E-16	0.85			
		nbH-19	147	9.499E-17	1.42			
		nbJ-56660	174	1.0788E-16	0.85	0.835±0.001	1	either both sky line residuals or
		nbJ-57606	175	8.8372E-17	0.82	0.835±0.001	1	both Hα
		nbJ-58231	176	7.4111E-17	0.8			
		nbH-24	192	9.363E-17	1.41			
	IRS2	nbJ-28172	24	1.0062E-16	0.82			
		H2S1-26358	25	1.0138E-16	2.45			
		nbH-27	28	1.747E-16	1.48			
		nbJ-26017	30	7.7877E-17	0.82			
		H2S1-33987	36	1.1629E-16	1.98			
		H2S1-39002	39	1.1495E-16	2.19			
		nbJ-39133	40	1.3733E-16	0.82			
		nbJ-43634	54	1.8601E-16	0.8			
		nbJ-41130	56	1.9514E-16	0.85			
		nbJ-35800	59	2.5125E-16	0.85			
		nbH-39	64	1.444E-16	1.43			
		nbJ-46043	73	1.0767E-16	0.85			
		nbJ-66380	88	1.1120E-16	0.85			
		nbH-37	97	1.534E-16	1.47	1.44	2	possible Hα and Hβ
		nbJ-38883	107	8.3959E-17	0.87			
		nbJ-33250	109	9.0457E-17	0.85			
		nbJ-35257	146	1.01916E-16	0.8			

Table 5.1: HiZELS objects observed in October 2009 and December 2009. The quality flag provides a qualitative measure of the confidence in the redshift determination, with 5 being a secure redshift and 1 being the least secure.

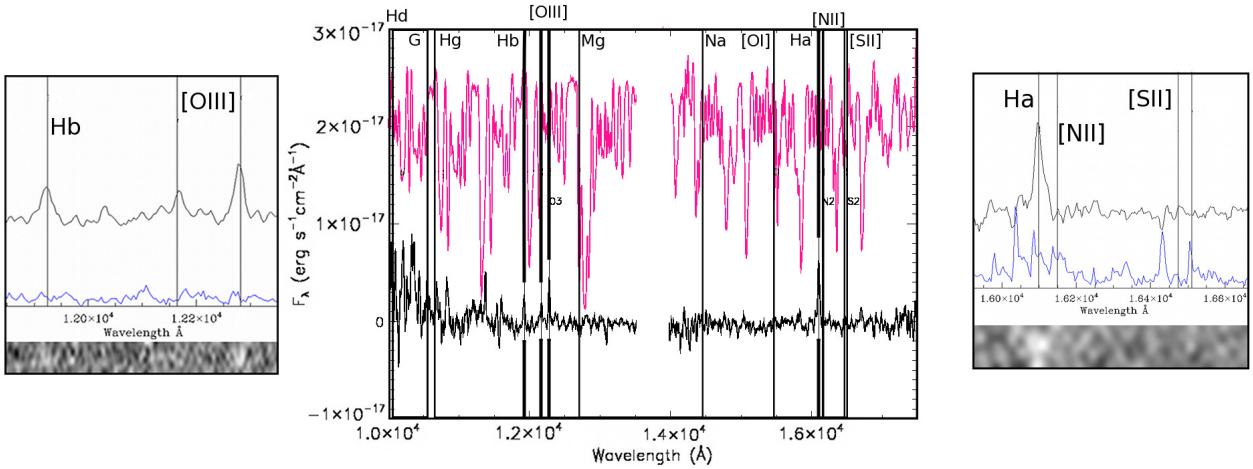

(a) nbH-32, z_{spec}=1.453

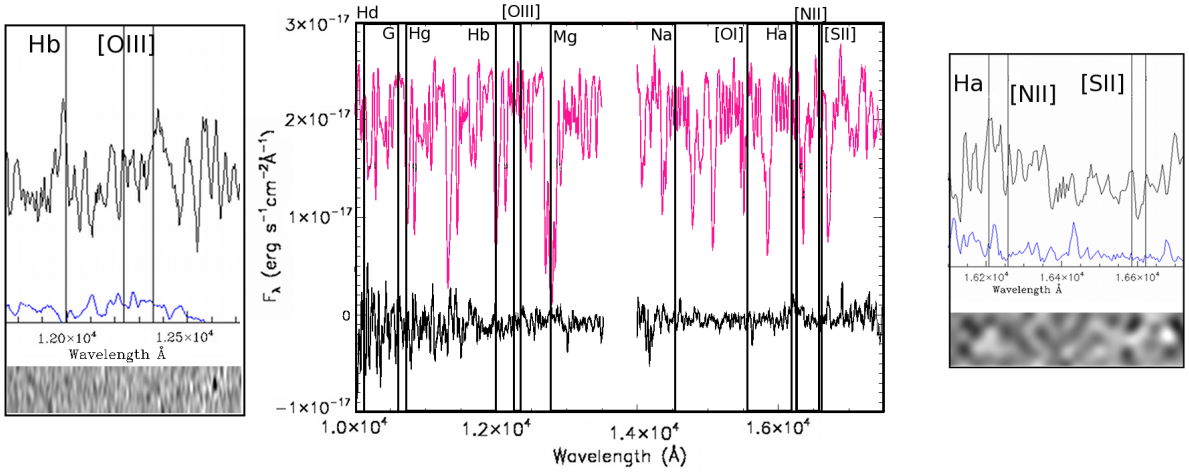

(b) nbH-10, z_{spec}=1.468

Figure 5.4: Two HiZELS objects detected in October 2009, with their newly determined spectroscopic redshifts. The pink line shows the relative throughput of the mask from the flat-field image. These show the exact positions of the mask features while they are imperfectly aligned. The central empty regions in the plots correspond to the position of the slit. Regions around the emission lines are shown to the left and right of the main spectrum with the corresponding 2D spectrum at these points. The blue lines on these zoomed-in sections show the residual sky subtracted from each spectrum (after initial sky subtraction performed on a frame by frame basis, see text for details of both levels of sky subtraction) and so peaks in this show the region of any suspected sky line residuals in the spectra (not same scale as spectrum, scale and offset chosen to for illustrative purpose).

5.2.1 HiZELS as a test of FMOS

Spectroscopic vs. Narrow-band imaging determination of emission line flux

The Narrow-band determination of the Hα flux given in Table 5.1 is determined from the narrow-band and broad-band fluxes in the following way:

$$F_{line} = \Delta\lambda_{NB_J} \frac{f_{NB_J} - f_J}{1 - (\Delta\lambda_{NB_J}/\Delta\lambda_J)} \tag{5.1}$$

This estimate of the line flux includes any contribution from the nearby [NII] line and depends on the position of Hα within the narrow-band filter. It is calculated from narrow-band and broad-band fluxes within a 3" diameter aperture on source (Sobral et al., 2009). These fluxes can be compared to those obtained from the spectra containing good signal-to-noise Hα detections, by convolving the line profile with the HiZELS narrow-band filter profile. The flux determined from the spectra must include any [NII] emission to remain consistent with the narrow-band line fluxes. An aperture correction also needs to be applied on a source-by-source basis since the fibre aperture is significantly smaller than the HiZELS aperture, being 1.2" diameter on sky.

The Hα+[NII] flux estimates were obtained by summing the flux within the extent of the two lines after first having subtracted off the continuum, determined from adjacent regions of the spectrum, free from sky-line residuals. The errors are estimated by taking all the other spectra with no continuum or emission lines in the region of the Hα and performing the same operation. The errors are the standard deviation of the clipped distribution in fluxes. These error estimates then ensure that if the Hα emission is sat over a sky-line residual, the error should account for this. It is perhaps helpful to point out that the signal to noise estimates given in Table 5.2 are for the original emission line detection, with the noise estimated from adjacent regions of the same spectrum. The spectroscopically measured narrow-band flux estimates will have a different signal to noise ratio, depending on where they fall within the filter profile.

The aperture corrections were estimated using photometry performed on the H-band or J-band UKIDSS images, depending on the HiZELS detection filter (nbH or nbJ respectively), after first scaling the flux calibration to the photometry of the calibration star within a 1.2" aperture. Assuming the Hα emission is

uniform across the object, the ratio between the flux in a 1.2" aperture and the flux within a 3" diameter aperture (the size of aperture used for the HiZELS photometry (Sobral et al., 2009)), provides an estimate of the aperture correction. The H-band image was used with seeing FWHM of 1". The effect of seeing on this aperture correction was estimated using the original H-band image with seeing FWHM of ∼0.7". The effects of seeing are much smaller than the error estimates in the original flux estimate.

The main sources of error in these flux determinations will be from the positioning of the fibres and the sky-subtraction. To estimate the errors introduced by fibre positioning can be modeled, to an extent, when applying the aperture correction. A monte-carlo simulation of the error in positioning uses a maximum error of 1.5" radius, and a number of fibre centres distributed normally about the object centre with a sigma of 1.5" (radius from centre within which 68% of the objects fall is 0.75"). This is a lot larger than the quoted positional accuracy of the fibres (∼0.2") as here the dominant error is in the loss of flux with time due to the misalignment between the FMOS wide-field corrector and the telescope axis (section 4.2). The quoted positional accuracy is a measurement of the accuracy of the acquirement of the fibre positions in the initial configuration, and would underestimate the positional errors in this case. A sigma of 1.5" was chosen as the offset between source position and actual fibre position varied with time, and was dependent on position in the field of view. The brightest sources showed a decrease of at least a factor of 10 in S/N over the October integration (for the usable frames, see section 4.2), indicating that the fibre had moved far off centre though still managing to detect some of the source flux. For a likely galaxy size of 1-2" (including seeing) a displacement of radius 1.1-2.1" is required to put the fibre completely off source and so the 1 sigma value of the positional uncertainty was chosen to be smaller than this, though a fairly flat distribution of offsets was desired since these large offsets were systematically occurring across the field of view. The distribution of aperture corrections ($\frac{fluxwithin3"aperture}{fluxwithin1.2"aperture}$) gives a sharp minimum, where the fibre is correctly centred, and increases with a shape dependent on the profile of the source. The maximum aperture correction plotted in Figure 5.5 is taken as the aperture correction at which the histogram of counts falls to half its maximum value. As such this is not a definite maximum aperture correction but is an estimate fairly independent of the cutoff radius chosen and is chosen mainly to illustrate the effect of the positioning of the fibres on the error in the flux estimates. This treatment of the aperture correction will be an over-estimate for the one source, nbJ-38031 taken from the December data since the fibres were re-configured after each frame and

the variation in detected source flux was much smaller.

The comparison of Narrow-Band fluxes to those measured from the spectra are displayed in Figure 5.5. The black points and error bars show the estimates using the minimum aperture correction, for well positioned fibres, and the pink points plus error bars show the estimates using the maximum aperture correction estimate. Other than the one source, the spectroscopically determined estimates are systematically low, though by varying amounts. The one high point (for object nbH-21) is probably affected by a near-by sky-line residual producing the high value. This indicates that, as expected, the inaccuracy of fibre positioning is the dominant source of error in the absolute flux calibration for this data set and that we cannot assume a linear calibration between flux measured from the spectra and the true object flux.

We would expect the estimates for sources measured in December to be better as the fibre positioning was re-calibrated between each pair of sky and object observations. The one HiZELS source with good signal-to-noise from this data set (nbJ38031) shows a much lower flux estimate with respect to the narrow-band flux estimate, however. This is not a truly comparable object, however, as it is an nbJ-detected object, whereas all of the October observations were of nbH-detected objects. This puts the emission line within a heavily masked region. It can be seen from Figure 5.6 that the emission line is not only on the edge of the nbJ filter, which makes the nbJ-measured line flux less reliable, though the effect should be to underestimate the line flux, not over-estimate it, but it is also possible that some of the Hα and [NII] emission is being cut out by the mask. This effect would not be large enough to increase the estimate of the narrow-band flux by a factor of $\sim 3-4$. It is still possible that the fibre positioning is not accurate enough to recover the full flux in this line but the range of modeled aperture corrections do not account for the flux difference, though there is one flaw in the assumption chosen here, and that is that the Hα emission follows the same distribution as the profile of the source in the broad-band image. A larger sample of good signal-to-noise detections with corresponding narrow-band photometry, with detections at all positions within the filter would be needed to untangle what is going on here. Unfortunately the position of the masked sky lines within the wavelength range of this particular narrow-band filter make this difficult.

The HiZELS objects provide an independent test of the flux calibration of the data-set, using the narrow-band determined line fluxes as a comparison to the flux returned by convolving the line emission with the narrow-band filter profile. This comparison displays that, as expected for this data set, the absolute flux

Date	HiZELS ID	spec-z	Hα S/N	Narrow-Band line flux	Hα+[NII] flux through HiZELS filter	Aperture Corrn		Corrected filter flux
						min	max	(using min Aperture Correction)
Oct09	nbH-32	1.453	8.8	1.807E-16	1.15E-16±2.56E-17	1.03	1.28	1.18E-16±2.64E-17
	nbH-21	1.47	5.8	1.283E-16	9.00E-17±2.09E-17	2.05	2.34	1.85E-16±4.28E-17
	nbH-1	1.46	6.8	2.588E-16	7.97E-17±3.85E-17	1.56	2.10	1.24E-16±6.01E-17
	nbH-10	1.468	3.1	1.261E-16	5.51E-17±3.87E-17	1.48	2.03	8.15E-17±5.07E-17
Dec09	nbJ-38031	0.85	6.2	2.6403E-16	6.799E-17±1.199E-17	1.32	1.75	8.94E-17±1.58E-17

Table 5.2: Narrow band fluxes vs. those determine spectroscopically as described in the text.

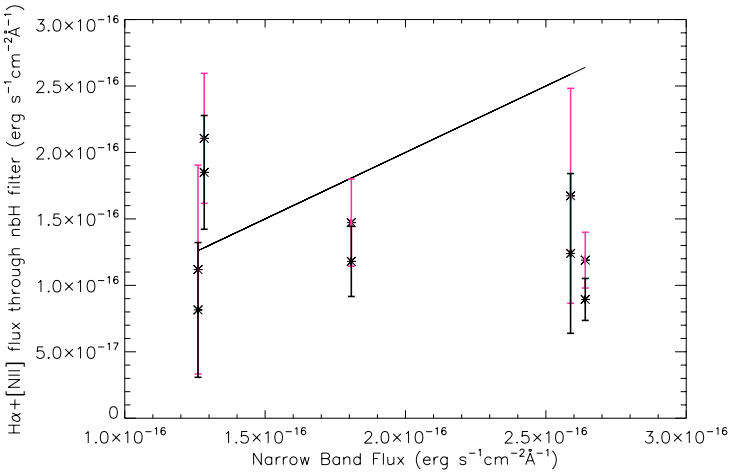

Figure 5.5: The Hα+[NII] fluxes determined by convolving the spectra with the HiZELS nbH filter profile, and corrected using an aperture correction, are plotted against the fluxes determined from the narrow band images, according to Equation 5.1. The errors are estimated by performing the same operation at the same positions in other, empty spectra. The pink points and error bars show those estimated with the maximum aperture correction and the black points plus error bars show those estimated with the smallest aperture correction, where the aperture corrections are explained in the text.

calibration is not accurate enough to determine absolute star formation rates of objects from line detections alone. The reasons for this are many, including the absence of a fibre-flat taken with the fibres in their observing positions and difficulties in the fibre positioning during the observations.

5.2.2 FMOS as a test for HiZELS

FMOS provides valuable test of the selection criteria of HiZELS emission line objects, checking that the narrow-band detection is, indeed produced by Hα with spectroscopic redshifts, and testing the contamination of the selection by AGN and the contamination of [NII] to the Hα flux estimates. FMOS is particularly valuable for checking the properties of the nbH-selected objects, since they require spectroscopic targeting in the near-infrared to secure multiple-line spectroscopic redshifts, and to check the rate of AGN contamination. The multiplicity of FMOS, along with it's wide field of view make it capable of targeting large

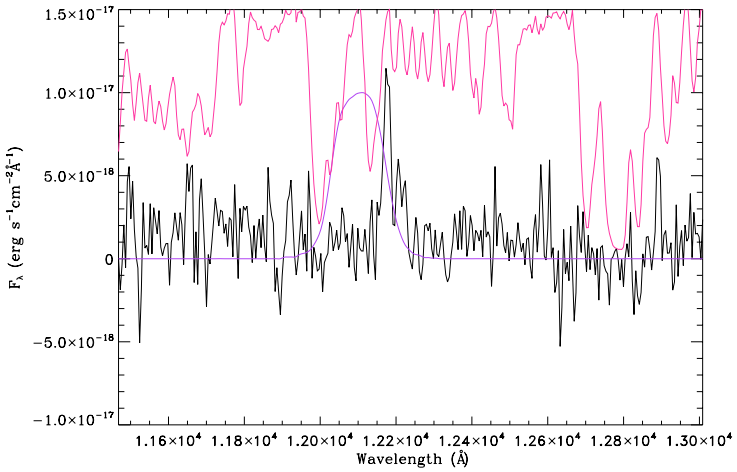

Figure 5.6: The un-smoothed spectrum of nbJ38031 in the region of the Hα and [NII] lines. The purple line shows the position of the nbJ HiZELS filter and where Hα falls within the filter. The pink line shows how the throughput varies in this region due to the OH-suppression mask.

proportions of the objects relatively cheaply in terms of telescope time.

By targeting these galaxies, we have provided spectroscopic redshifts for 14 of the sources, 8 of which are nbH sources. The systematic sky residuals have hampered the assignment of redshifts to the nbJ objects, where we only expect to observe Hα, and so depend on a single line for a redshift estimates. For the nbH-objects, however, we are doing better. With the current observations, we cannot offer any insight into the possible redshift distribution of Hα within the narrow-band filters, due to the small number of objects with assigned redshifts. We can also not say whether a non-detection is an indication that the line flux is too low for FMOS, as the mask is still not fully aligned and is creating difficulties with sky subtraction, and could be cutting out the line emission.

We can, however, say that the early indications show that the rate of contamination due to AGN seems to be low. From our nine objects with detected Hα, only one, nbH-2, has evidence of *possibly* harboring an AGN, with emission lines broader than for the other galaxies in the HiZELS sample ($\sigma \sim 211$ km s^{-1}), and relatively high amounts of [NII] and [SII] emission. This velocity dispersion is consistent with that of an elliptical galaxy and does not require the presence of a black hole to produce these velocities.

In this case we look to the emission lines to tell us if there is any hint of AGN activity. Baldwin et al. (1981) first suggested the use of the ratios of [NII] to Hα and [OIII] to Hβ flux as a method for identifying AGN (come to be known as the BPT diagram). The details of the line strengths of different species in an

object spectrum can tell us a lot about the excitation mechanism which is producing that line emission. Three main excitation mechanisms that contribute to exciting various species are; energetic UV continuum radiation from young, hot O and B type stars; power-law continuum produced in AGN due to release of the rest mass of matter being accreted onto a super-massive black hole, and shock wave heating. The radiation present in AGN produces emission lines for a wide range of excitations, from a continuum that extends far into the UV, while in starburst galaxies the ionising radiation drops bluewards of the Lyman limit. In AGN we actually see an enhancement of both high- and low-ionisation lines in AGN relative to what's found in HII regions. This is because the more energetic radiation penetrates further into the inter-stellar gas clouds producing partially ionised zones. [NII] and [SII] are two such low-ionisation lines, of which [NII] is clearly visible in the spectrum of nbH-2 shown above and the presence of [SII] is hinted at, though the detection is ropey.

The advantage of the BPT diagnostic is that the lines being compared are close in wavelength and so should be mostly unaffected by differential extinction between them. Narrow-line AGN are observed to lie at upper right corner of the plot, away from the star-forming sequence. The ratio of [NII] to Hα flux, determined from Gaussian profiles fitted with fixed relative positions and the Gaussian widths to be the same for each of the lines, places the object at $log(I([NII])/I(H\alpha) = -0.5 \pm 0.2$, where the errors are determined as explained below for fits performed in IRAF. The [OIII] and Hβ detections are not high enough signal to noise and are hampered by systematics in the sky subtraction and so the corresponding ratio of [OIII] to Hβ flux is not available to give a firm determination of the source of ionising flux. The observed [NII]/Hα ratio is observed in both star-forming galaxies and AGN. It is possible that this [NII] contribution could be observed in a particularly strong starburst but, given that the broadening of the line is consistent with an elliptical galaxy, this explanation looks unlikely. We do not tend to see such strong starbursts in ellipticals. In this case, therefore it is more likely that the high ratio of [NII]:Hα flux is due to an AGN.

For the objects where we have narrow-band line fluxes, a high signal-to-noise detection of Hα and where the emission lines reside within the filter (not at it's edge), we can produce a true star-fromation rate estimate from the Hα emission, separating it from any [NII] emission. For this, we use that narrow-band flux determination as an absolute flux calibration to scale the emission-line flux first, with the results given in Table 5.3. The first flux measurement is made from a direct sum of all pixels containing possible Hα flux,

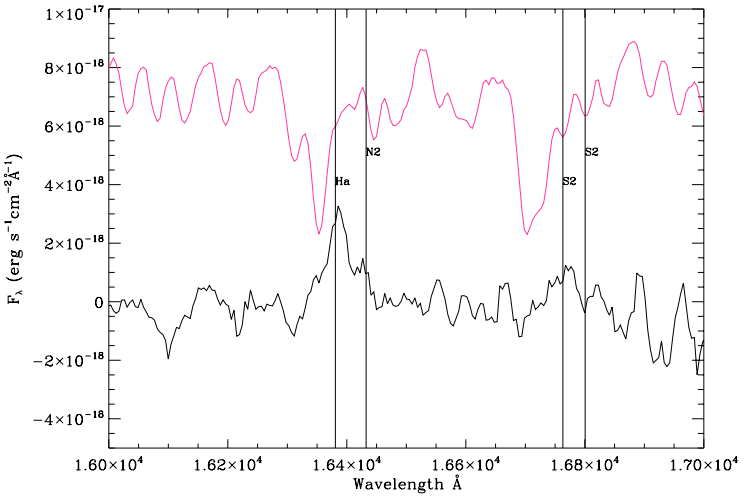

Figure 5.7: The Hα detection for nbH-2, a potential AGN. The pink line shows the throughput from the mask.

and the error associated is taken from the distribution of fluxes estimated from empty spectra in the same region (to account for systematic errors), together with the error in the spectroscopically measured narrow-band flux measurement, used to scale the values to the fluxes measured from the narrow-band images. The gaussian fits are performed in IRAF, using splot, with a contribution from [NII](6584Å) also fitted, requiring the relative wavelengths and FWHM for both lines to remain constant in the fit. The errors for these measurements are provided by IRAF, where monte-carlo simulations are produced by adding gaussian noise, defined by the noise model, to the original fit parameters, and new fitting parameters obtained. These errors are again combined with the error in the spectroscopically-determined narrow-band flux estimates. The star formation rates are determined from the direct sum of pixels containing possible Hα flux, and the errors are taken from the error in this sum.

These estimates indicate that we are detecting objects with SFR of $\sim$24M$_{\odot}$ yr^{-1} with S/N in Hα of $\sim$7-8 (being cautious of the result for nbH21, given the proximity to a possible large sky residual, as mentioned above). These are effectively aperture corrected, total SFRs and bode well for reaching a lower SFR limit with data unhindered by the fibre-positioning sky subtraction problems exhibited here.

The velocity dispersion measurements were taken from the best-fit FWHM for the Hα lines. To take account of the PSF of the instrument, the width of the calibration arc lines were measured in the vicinity

Object	Hα flux (direct sum) erg s^{-1}cm^{-2}	Hα flux (gaussian fit) erg s^{-1}cm^{-2}	Measured Gaussian FWHM (convolved with instrument PSF) Å	Velocity sigma km s^{-1}	SFR M$_\odot$ yr^{-1}
nbH32	3.436E-16±2.6E-17	3.337E-16±2.8E-17	25.97±2.576	131	23.3±1.8
nbH21	1.018E-16±1.2E-17	1.010E-16±1.4E-17	27.62±4.188	150	10.9±2.2
nbH1	2.281E-16±3.1E-17	2.219E-16±3.5E-17	21.24±3.984	unresolved	24.0±3.3

Table 5.3: Calibrated star formation rates (SFR) from measured Hα flux scaled according to the flux measured through the narrow band filter.

of the detected Hα with a FWHM of $\sim$ 20Å. This corresponds to a velocity dispersion of $\sigma \sim$ 158km s^{-1} (at $\sim$ 16000Å). As such the measured velocity dispersions are subject to large errors and the two lines for which this quantity are estimated are only partially resolved.

5.3 Other Targets and Impact on Target Selection

The full list of objects with assigned spectroscopic redshifts are listed in Appendix D. These targets are not selected from a single selection function. They include broad-line AGN, narrow-line AGN and star-forming galaxies and they cover a wide range in redshifts. As such they cannot be used as a cohesive sample for testing a particular selection mechanism. What they can show, however, is whether a crude cut in B-band magnitude is appropriate to preferentially select star-forming galaxies.

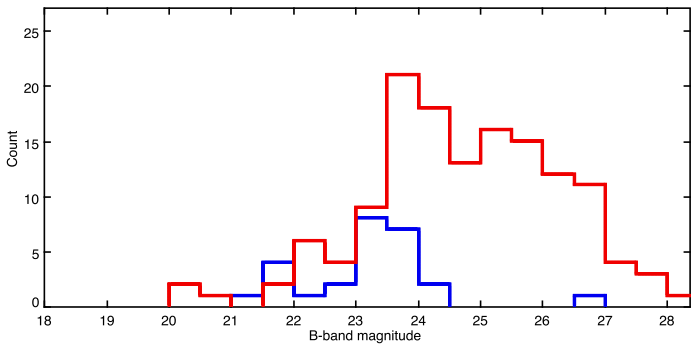

Figure 5.8: Distribution of B-band magnitudes of objects targeted in December with redshift $z > 1.2$ (red histogram) and all objects in December that have been assigned a redshift (blue histogram)

Figure 5.8 shows that, although the targets from December with redshift $z > 1.2$ covered a broad range of B-band magnitudes (red histogram), barring one object, the only only targets to secure redshifts had a

B-band magnitude < 24.5, justifying a B-band cut.

Given that the success of detections depends on the positions of the individual spectra on the OH mask, and also it's redshift (which part of the spectrum the emission lines fall in), one cannot say anything about the sources not assigned a redshift.

Chapter 6

ISAAC Observations of JKCS041

6.1 Introduction

Figure 6.1: The optical/near-infrared false colour image at the position of the potential cluster JKCS 041 with the X-ray detection shown in blue.[1]

JKCS 041 is a possible galaxy cluster in the CFHTLS Deep-1 field. It's detection is reported in Andreon et al. (2009) with a photometric redshift estimate of $z_{phot} \sim 1.9$. With the current highest redshift cluster detection (at the time of writing) at 1.753 (Henry et al., 2010), derived from the spectroscopic redshift of the brightest galaxy member, JKCS 041 would be the highest redshift cluster detected to date, if the photometric redshift estimate is accurate.

The cluster was detected as an over-density of sources of similar colour, from the J- and K-band photometry released in the UKIDSS Early Data Release (Dye et al., 2006) using a version of the red sequence

1. Image credit - X-ray: NASA/CXC/INAF/S. Andreon et al. Optical: DSS; ESO/VLT

method (Gladders & Yee, 2000). This colour is consistent with the presence of the 4000Å break falling within the region of the the J- and K-bands, and the over-density of sources in the colour space indicates that there are more objects than usual in a small redshift range. The red sequence method uses the observational result that all clusters seem to contain a population of early-type galaxies, called the red-sequence, that lie along a linear colour-magnitude relation, and were formed at high redshift.

There is an X-ray detection at the position of the observed over-density and is shown in blue in Figure 6.1. Andreon et al. (2009) find a best-fitting spectral model to the observed X-ray spectrum, with a temperature of $7.6^{+5.3}_{-3.3}$keV for a plasma model with redshift fixed at 1.9. This temperature, in turn, provides an estimate of $R_{500} = 0.52$Mpc (the radius within which the density is 500 times the critical density at the cluster redshift), and a mass within this radius $M_{500} = 2.9^{+3.8}_{-2.4}$ x $10^{14} M_{\odot}$. These estimates all depend on the X-ray source being associated with the observed over-density and being situated at redshift 1.9.

6.1.1 Spectroscopic follow-up

It is still possible that the detected structure could be a line-of-sight blend of smaller structures since the accuracy in photometric redshifts or colour analysis are limited by the sampling of the SED by the filter set. This limit in photometric redshift accuracy produces confusion in the line-of-sight direction, in this case, an optimistic photometric redshift error of $\delta z \sim 0.02$ equates to a distance along the line of sight of $\sim$30Mpc. These errors need to be reduced before we can tell whether these objects are all associated with one halo. This can be achieved with spectroscopic redshifts of member galaxies.

6.2 Observations

In November 2009, three possible member galaxies were targeted with ISAAC on the VLT. The three galaxies were placed within two slits, with the configuration shown in 6.2.

Over 4 consecutive half-nights, the objects were targeted over the second half of the night. Slit 1 was observed on the first three nights, with slit 2 being observed at the end of the third night, as well as on the final night.

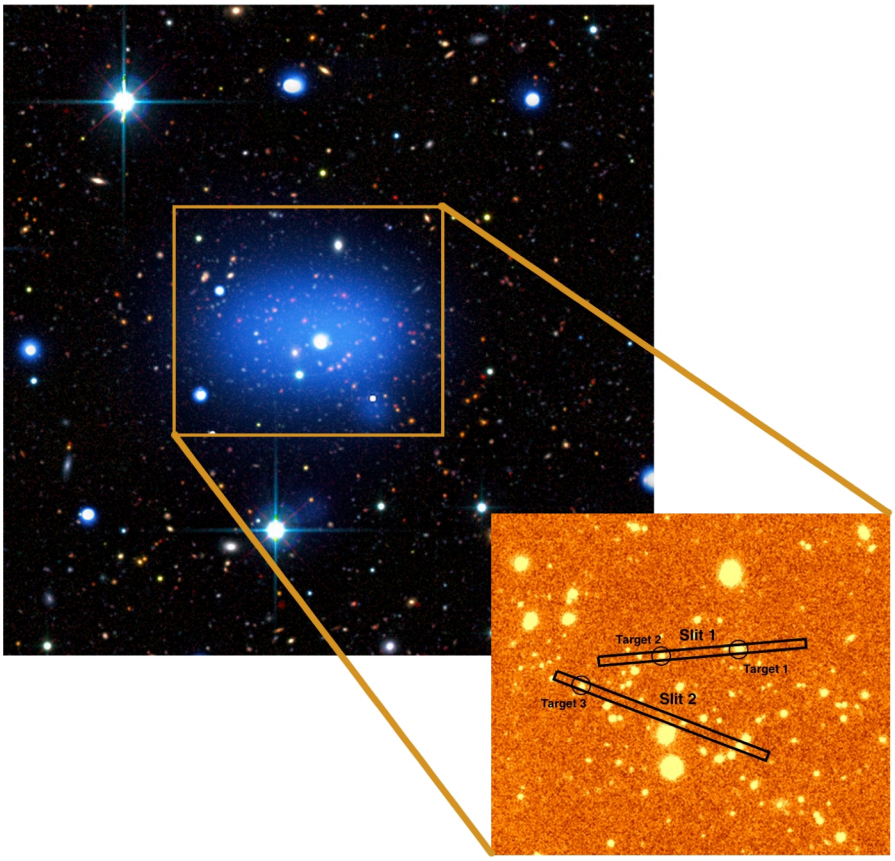

Figure 6.2: The targets chosen for spectroscopy. Two objects were targeted in Slit 1 and one targeted in Slit 2. [1]

1. Background Image credit - X-ray: NASA/CXC/INAF/S. Andreon et al. Optical: DSS; ESO/VLT

6.2.1 Observing Strategy

Each slit was observed employing the ABBA method of sky subtraction. This method places the objects at two different positions along the slit in consecutive observations (position A then position B). The first stage of sky subtraction is a simple subtraction of frame B from frame A. This leaves an image with a negative and positive trace of the object. The residual sky present due to temporal changes in the background emission is then removed by shifting the object trace in frame B to lie over frame A and subtracting the negative trace from the positive trace.

6.2.2 Calibration Observations

Standard stars were observed at the beginning and end of each half-night observing. They were chosen to have airmass close to that of the observations at the beginning and end of the night respectively. These observations were used for flux calibration and telluric correction of the object spectra.

Arc observations and dark frames were also taken for each night's observations. The arc frames were used for wavelength calibration, to be refined for the on-sky observations using atmospheric OH lines.

6.3 Data Reduction

A combination of ISAAC pipeline procedures (Observatory, 2009), IRAF tasks and purpose-written IDL programs were used to reduce this data. The faintness of the objects made the data unsuitable for complete reduction using the pipeline routines. This is because the absence of object detections in the single frames meant that any cross-correlation employed in the stacking pipeline procedure, for refinement of the telescope nod estimates, would not work. The signal-to-noise of the object in the stacked frame is also not high enough to define the trace across the entire image. The image distortions were therefore first corrected before stacking so that the resultant spectra were straight and could be summed in the dispersion direction before extraction.

6.3.1 Flat Fielding

The flat field lamp is imaged each night before observations are taken. The ISAAC pipeline procedure isaac_spc_flat was used to combine the individual flat field images. The procedure takes the normalised difference of an image with the flat field lamp on and another image with the lamp off. It then takes account of the non-uniform illumination of the slit by the lamp by fitting a polynomial to the image in the slit direction, to divide the image by. Multiple flat-field observations are then averaged.

The shape of the flat-field lamp was then divided out by fitting a cubic spline of order 100 to the flat field image in the dispersion direction. Due to a slight tilt of the slit with respect to the detector pixel grid and also the curvature of the image in the slit direction, the flat-field image was first divided into sections in the slit direction and each section fit to individually. The normalised sections were then reassembled into the final flat-field image.

When splitting the image into sections, care must be taken to ensure that the boundary between the top and bottom detector chips is not in the middle of a section. Fitting to either side of this boundary independently enables the removal of any residual bias left in the averaged flat-field image.

Each science and calibration frame is divided by this flat-field image to remove variations in pixel-to-pixel sensitivity.

6.3.2 Cosmic Ray Removal and bad pixel masking

Bad pixels were masked using the bad pixel maps supplied by the observatory. The cosmic rays were detected and removed on a frame by frame basis using L.A. Cosmic (van Dokkum, 2001), an IRAF routine that detects cosmic rays from their sharp edges using a Laplacian edge detection algorithm.

6.3.3 Correcting Slit Curvature and Wavelength Calibration

A couple of times a year, the observatory observes a standard star at different positions along the slit to be used for correcting curvature in the images in the spatial direction. These can be used, along with the calibration arc images to model the image distortion, in both the wavelength and spatial directions, and correct for it. The method used to do this is based on that detailed in Valdes (1986) and the steps are as follows:

- First take a calibration arc image and identify the lines along some dispersion line using the task identify.
- Use reidentify to find the positions of the same lines at equally spaced positions along the slit.
- Fit a two-dimensional function to the wavelength solution as a function of both line and column number using fitcoords.
- Now, for each startrace image, use identify to record the position of the centre of the spectrum along some column (if the dispersion direction is along the columns then you would identify its position along a line).
- Use reidentify to assign the centre of the spectrum with this value at all points along the dispersion direction.
- Combine all the database entries for the startrace frames and fit a two-dimensional function to the distortions in the slit direction using fitcoords (fitcoords allows you to combine the data by inputting a list of files and switching the combine switch on).
- The results of these two coordinate function fits are used together in the transform task to correct the image distortions and produce an image that is linear in both the spatial and dispersion directions.

First a calibration arc image is needed. Each night, a few arc image frames were taken and were flat fielded before averaging using imcombine to reduce noise. The startrace observations were obtained from the ESO science archive.

6.3.4 Image Stacking

The data are taken in ABBA format. This means that successive frames are taken with the object positioned at different places along the slit, first at position A, then at position B. Each sequence of nodded observations are first combined in pairs of frames (AB, BA). The first stage is to subtract a B-frame from an A-frame then, subtract this frame from itself, with an offset defined by the size of the nod between the observations. For these observations, the pointing information supplied in the headers is used to determine the distance of the nod and to interpolated successive pairs to the same position. This is not optimal as the telescope pointing

is not usually very accurately calibrated for these nodding observations, but the spectra are not visible in individual frames, so their precise locations cannot be determined to provide better estimates of the nodding offsets.

Other observers (Kriek et al. (2008), for example) have tackled this problem when targeting equally faint objects by placing the standard star at the approximate position of the object on the slit after each frame.

6.3.5 Telluric Correction and Flux Calibration

There are no spectrophotometric standard stars available for calibrating near-infrared observations.

Two standard stars were observed each night, chosen to be close in airmass to the observations at the beginning of the night and the end of the night respectively. The stars chosen were all B-type stars that have a fairly featureless spectra in the wavelength of interest that can be modeled as a black-body spectrum of the appropriate temperature, given the spectral classification of the star.

The frames containing the standard star exposures were reduced, stacked and extracted in the same way as for the object frames. To remove the instrumental response function and correct the atmospheric telluric absorption features, the standard star with observed airmass closest to that of the observations is divided through the observed frames.

The most important factor in this correction is to leave the observed object spectra with no instrumental imprint left on the continuum. No attempt to match effective airmass is attempted further than choosing the star with closest matching airmass for the correction. This is because any scaling applied to the stellar spectrum will scale the instrumental response function that is still present. The airmass corrections are also expected to be small in the near-infrared, so choosing the star closest in airmass should be reasonable.

This stage provides relative flux calibration by multiplying the telluric-corrected frame by the appropriate blackbody curve of the star.

6.3.6 Noise Estimates

The noise in the final spectra is dominated by the sky. The noise is tracked in the reduction process starting from the sky subtracted, nodded frames. The noise at each wavelength is estimated using 3σ clipping about the median value for each column within the region of complete sky subtraction. When the standard

deviation of the clipped distribution varies by less than a fraction of a percent, that standard deviation is recorded as the noise.

This noise is combined with the noise from the telluric spectrum when the images are divided through by the standard star, according to

$$(\frac{\sigma_{corr}}{corr})^2 = (\frac{\sigma_{obs}}{obs})^2 + (\frac{\sigma_{tell}}{tell})^2$$

where σ_{corr} is the noise of the telluric corrected image, σ_{obs} is the noise in the sky subtracted, nodded image and σ_{tell} is the noise in the telluric spectrum. This is applied on a row by row basis to the noise image for each image contributing to the stack.

The noise in the bright telluric spectrum is assumed to be dominated by poisson statistics. To estimate this noise, the units for each observed frame must first be converted back into photon counts. The observations are taken in NDR mode with 6 equally spaced reads and the units of the final frames are an average of the individual detector integration times. The gain of the detector is 4.5 e^-/ADU so multiplying the image by the gain gives the average number of electrons per read. According to poisson statistics, the signal to noise varies as $\frac{N}{\sqrt{N}}$ where N is the number of electrons in this case. In the case of NDR mode the signal to noise varies as

$$SNR = SNR_{DC}\sqrt{\frac{N(N+1)}{6(N-1)}}$$

where SNR_{DC} is the signal to noise ratio of the direct counts. The two observations in the nodding sequence are also averaged further reducing this noise by $\sqrt{2}$. This is then converted back to the original units.

During flux calibration, the noise is then multiplied by the same blackbody spectrum as the data and the errors for each nodded frame are then combined in quadrature during stacking, taking account of the differences in coverage of the pixels due to cosmic rays and bad pixels.

6.3.7 Spectrum Extraction

The profile of the standard star observations was used to weight the pixel rows according to the S/N in the star observation. The rows for which the flux in the stellar profile was greater than 10% of the maximum were then summed to make the final 1D spectrum.

6.3.8 Combining Spectra

Spectra from the separate nights are combined in 2D, scaling each to match the flux in the extracted, binned spectra for each night, then weighted according to signal to noise in the 2D frames. The scaling to match the flux in each night's stacked frame corrects for the differences in seeing between the different nights, and any differences in relative flux calibration. The images are then interpolated to the same wavelength solution and shifted by integer pixel shifts in the vertical direction so that the peak in the flux in the 2D trace falls within the same pixel in the final stacked image. The 1D spectrum was then extracted as for the single night observations.

Target 1 was observed on the first three nights, and all three nights were used in the final stack, whereas the second night's observations were not used for the final stacked spectrum of Target 2. The weather and seeing were not optimal on the second night, and the observed trace was too low signal to noise. With the poorer sky subtraction possible from the second night's observations, including this data does not improve the overall signal to noise of Target 2. Target 3 was observed in slit 2 on the final nights, only one night's worth of data is stacked to make the final spectrum for this object.

6.3.9 Low-resolution Binned Spectra

When binning the spectra, a monte-carlo approach is used to provide an estimate of the bin value and its error. This method was chosen since the sky subtraction is imperfect and one cannot assume that the errors are independent.

It is assumed that the error in each pixel follows a gaussian distribution with its width defined by the error assigned to that pixel. 6000 random realisations of the bin are then produced with each pixel assigned a random value within the gaussian distribution centered on the measured value, and with width given by the pixel error. The bin is then assigned the modal value determined by 3σ clipping of the distribution of random values, its error is the standard deviation of this clipped distribution. This should prevent regions of poor sky subtraction from affecting the binned value.

Each of the low-resolution, binned spectra shown in Figure 6.3 show continuum that is fairly flat across the wavelength range. The large telluric absorption feature at ~ 11300Å takes out a lot of the information at lower wavelengths. These regions are cut at a high atmospheric transmission since there has been no scaling

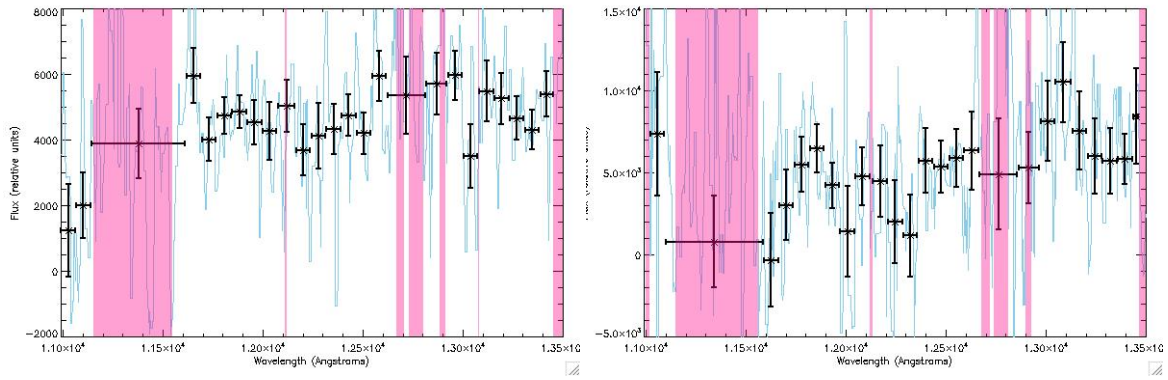

(a) Target 1

(b) Target 2

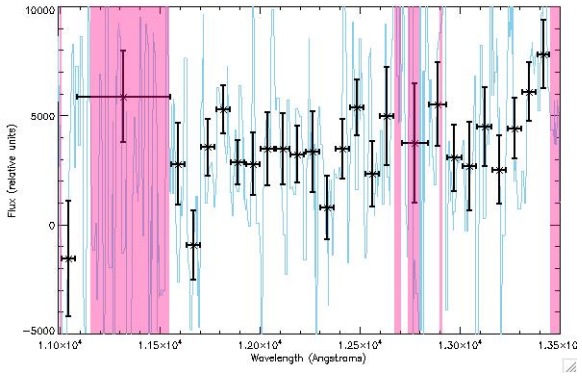

(c) Target 3

Figure 6.3: Low-resolution binned spectra for the three target galaxies. The pink shaded regions show regions excluded from the bins where the atmospheric transmission fell below 90 percent, as determined from the telluric star observations. The un-binned spectrum is over-plotted in blue.

applied to the star-observations to fit to the telluric absorption accurately, so the regions are un-reliable. Wavelengths below 11000Å are not included as the throughput falls off steeply at these low wavelengths. It is clear that to be able to determine what is going on (what redshifts these objects are at), we need to extend the wavelength range using broad-band photometric data.

It can also be seen from comparison of the binned spectrum and original spectrum for Target 2 that poor sky subtraction is affecting the binned values, though the continuum is consistent with being fairly flat to within the errors.

6.4 Broad-band photometric data

To add to the spectroscopic data, broad-band photometric data is available from the optical to the near-infrared from the public T0005 release of the CFHTLS-Deep survey and VIDEO. The J, H and K_s VIDEO images used here were mosaiced, calibrated and registered to the CFHTLS astrometric frame (Bonfield, D., private communication).

Photometry was performed on all eight images using SExtractor in dual image mode, selecting from the H-band where the targets are bright, and weighting using the H-band confidence image. The chosen aperture size, 2" diameter, ensures the apertures on the sources of interest are not contaminated by neighboring objects. The differences in seeing in each band were taken into account by calculating a point-source aperture correction for each image to correct the flux in a 2" diameter aperture to the total flux. The measured aperture corrections are documented in Table 6.4. A point-source aperture correction was chosen to account for differences in seeing, as opposed to the approach taken in Chapter 2 of convolving each image to the broadest PSF, since each of the three sources is only partially resolved in the images, so the point-source approximation is not a bad one. The region of the image is also quite crowded so broadening of the PSF is not preferable.

The stars chosen for calculating the aperture correction where chosen separately in each image from the locus of points in a plot of flux ratio (2" aperture/3" aperture) against flux. The point sources produce a well-defined locus in this plot and the saturated stars can be identified as they vary from the well-defined point source ratio. The curve of growth of the stellar profiles were examined in different sized apertures and an aperture of diameter 10" was chosen as the estimate of total flux. The mean in standard deviation in the

Filter	3" point source aperture correction (fraction of total flux within 3")
u*	0.949±0.006
g*	0.953±0.008
r*	0.952±0.008
i*	0.954±0.008
z*	0.945±0.013
J	0.878±0.006
H	0.897±0.012
Ks	0.913±0.018

ratio between the 3" aperture flux and total is then the aperture correction and error respectively.

The photometric errors are calculated for each source taking account of the correlated noise present in the VIDEO images due to the registering of the images to the CFHTLS pixel grid, which is smaller than the natural size of the VISTA pixels (see Section 2.3.2 for description). The error in the aperture correction is also added in quadrature to the photometric errors.

The photometric zeropoints were tested by comparing to the Pickles stellar library (Pickles, 1998) as in Chapter 2. Corrections were made to the zeropoints of the J, H and Ks bands of 0.1, 0.2 and 0.1 respectively, with an error of 0.05 in the calibration.

6.4.1 Photometric redshifts, broad-band data only

The same template set as used in Chapter 4 was used to find photometric redshift estimates for the targeted objects. To test the accuracy of the redshifts, they were compared to the VIMOS VLT Deep Survey (VVDS) spectroscopic redshifts (Le Fèvre et al., 2005). Only objects flagged with 95 and 100% confidence in the redshift were used as a comparison. The results are shown in Figure 6.4, and the photometric redshift estimates for the individual targeted objects are shown in Figure 6.5.

Further calibration of the photometric zeropoints were required at this stage, as displayed in Figure 6.4 (a). There is an option in Le Phare (Ilbert et al., 2006) that allows the user to find best-fitting zeropoint offsets to the data by using the fact that any systematic offsets will be independent of redshift. The program iteratively finds the best-fitting zeropoint shifts by setting the photometric redshift to the known spectroscopic redshifts of a sample, allowing the best-fitting templates to vary between each iteration. There are options to fit these shifts as a function of colour, redshift or template. All of these options, however take the original

Filter	Zeropoint correction
u*	0.18
g*	-0.096
r*	-0.064
i*	-0.067
z*	-0.04
J	0.025
H	0.248
Ks	0.025

Table 6.1: Photometric zeropoint calibrations from Le Phare (Ilbert et al., 2006)

task of calibrating the photometric zeropoints of the data to training the redshift estimates and calibrating errors within the templates themselves. Since the targeted objects are expected to be at higher redshift than we have photometric redshifts for, these options are not used, given that there is no way to model how the calibrations will be affecting the estimates of objects at higher redshift. The calibrated zeropoint shifts for each of the bands are recorded in Table 6.1.

Although the photometric redshift estimates have been improved by this zeropoint calibration, there is still a large scatter for redshifts above $z_{spec} \sim 1$, most likely due to the gap in filter coverage between the CFHT z*-band filter and the VIDEO J-band filter preventing the tight constraint of the 4000Å break between these filters at these redshifts. The VIDEO Y-band should improve this uncertainty. The redshift estimates are systematically lower than the spectroscopic redshifts above $z_{spec} \sim 1$, which is an important consideration when looking at the photometric redshifts of the target galaxies (Figure 6.5, results summarised in Table 6.2). All three estimates place the 4000Å break between the z* and J-band filters. The Y-band images will therefore be crucial for determining photometric redshifts of the other potential cluster members.

6.5 Redshifts from Spectro-Photometric Fits

The binned spectra are used together with the broad-band photometry to improve the photometric redshift estimates, with the hope of constraining the shape of the continuum in the region covered by the spectroscopy. This requires the absolute flux calibration of the binned spectra, which is achieved by scaling the flux obtained by convolving the un-binned spectrum with the filter profile to that obtained by photometry. The flux errors for the bins are combined in quadrature with the error on the photometric measurement. The

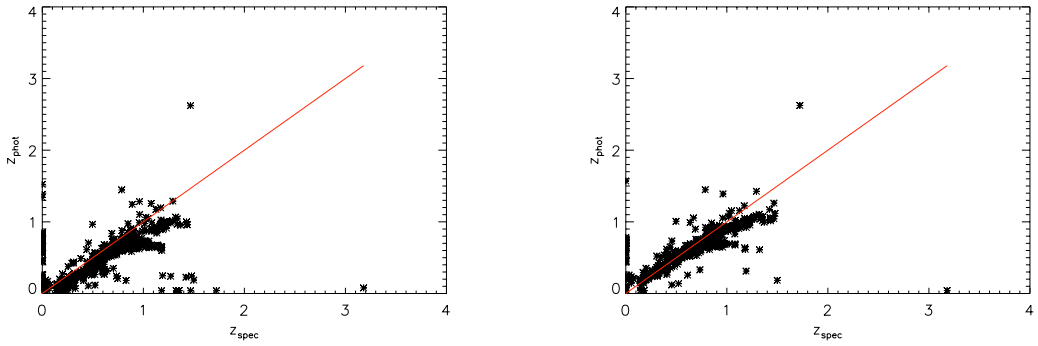

(a) (b)

Figure 6.4: Comparison of spectroscopic redshifts to photometric redshifts. [a] Shows the comparison after applying zeropoint corrections from comparison with stellar colours, but withouth calibrating the zeropoints with Le Phare (Ilbert et al., 2006). [b] Shows the improvement after further calibrating the zeropoints with Le Phare.

Object	Photometric redshift estimates	
	Broad-band data alone	Spectro-photometric fit
Target 1	$1.9024^{+0.0205}_{-0.0232}$	$1.8867^{+0.0034}_{-0.0117}$
Target 2	$1.4997^{+0.0262}_{-0.0263}$	$1.4788^{+0.0112}_{-0.0101}$
Target 3	$1.7475^{+0.0512}_{-0.0267}$	$1.7463^{+0.044}_{-0.0541}$

Table 6.2: Photometric redshift estimates, with upper and lower error values quoted from the upper and lower 68% confidence interval. Both the estimates determined with and without the spectroscopic information are included.

bins are then used as separate top-hat filters in Le Phare to constrain the position of the 4000Å break between the z* and J-bands, any masked regions in the binned section are also masked in these filters. Figure 6.6 shows the results, with the best-fitting photometric redshift estimate and upper and lower errors defined by the upper and lower 68% confidence contours. These are determined in Le Phare from contours of equal $\Delta\chi^2 = 1$.

These indicate that the binned spectrum for object 1 is indeed tightening the constraints on the photometric redshift estimate. The errors on the binned spectrum for object 3 are too large, and actually broaden the 68% confidence interval. The confidence intervals for object 2 are tightened but, given the level of systematic errors plaguing the spectrum, for both objects 2 and 3 it is not possible to categorically discount the presence of a break within the observed wavelength range and, despite the effort to make the errors representative of the systematic and Poissonian errors present, they likely still underestimate the systematics.

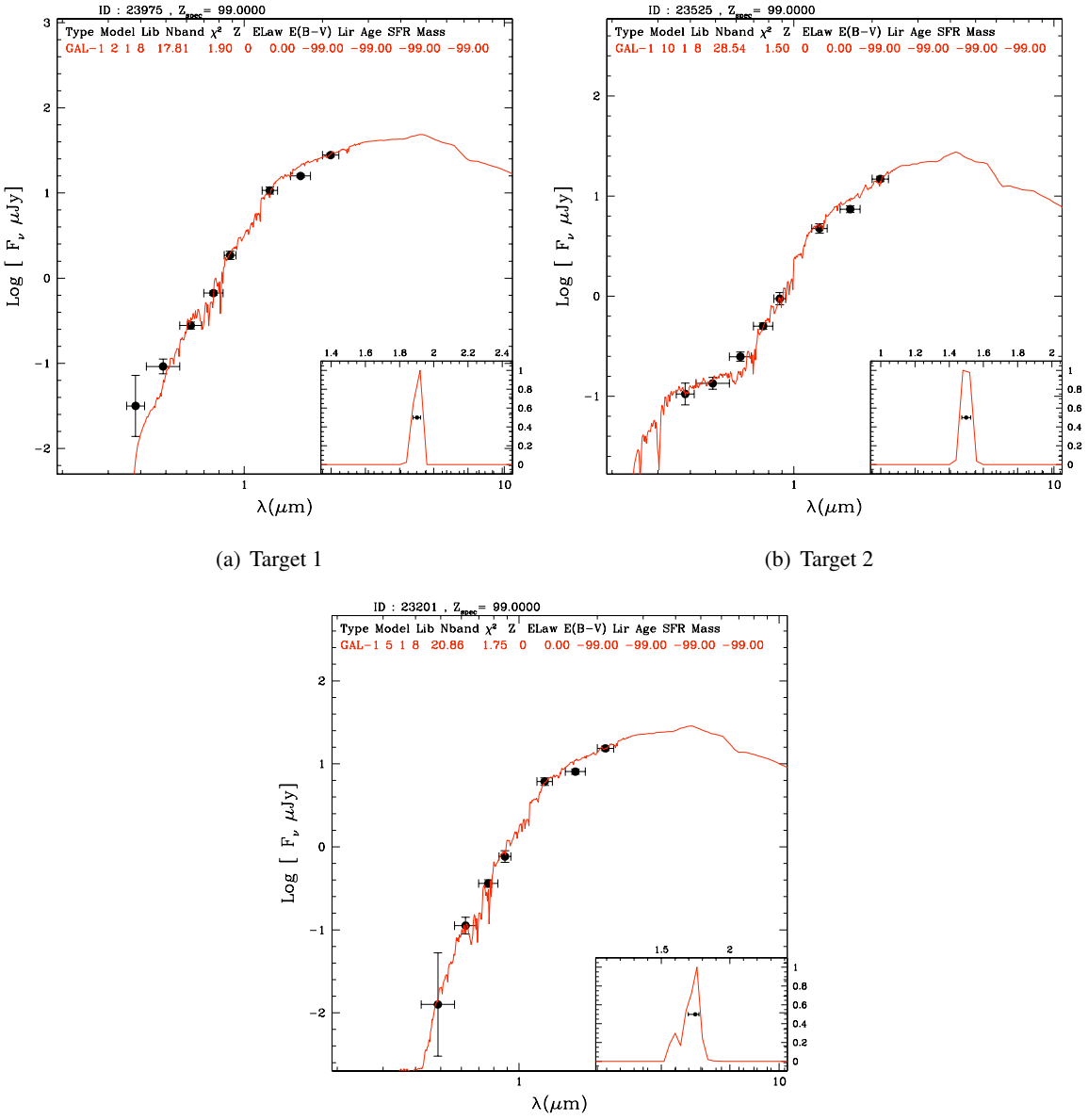

(a) Target 1

(b) Target 2

(c) Target 3

Figure 6.5: Best-fitting templates and SEDs for the three target objects. The insets show the probability distribution functions P(z).

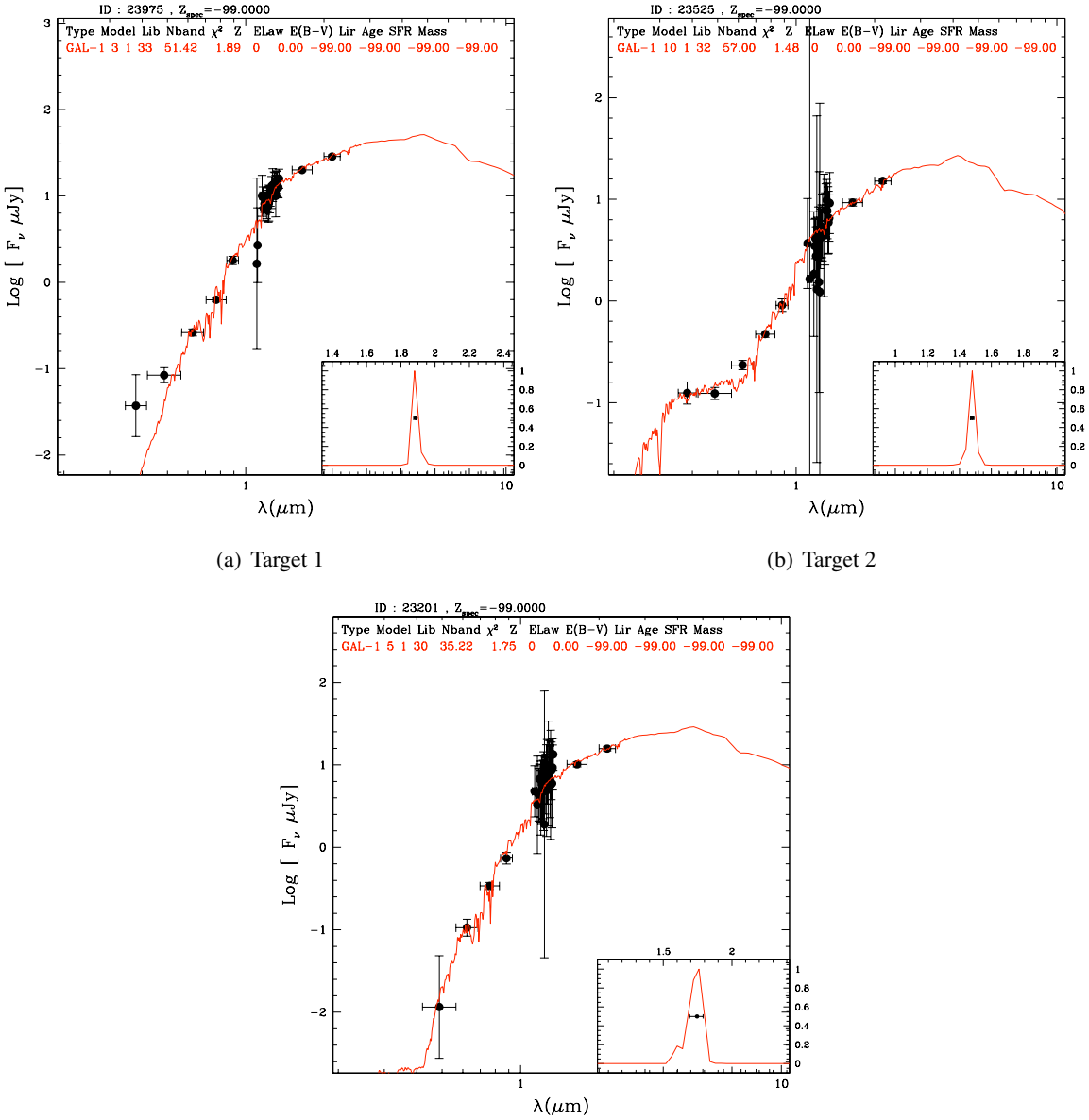

(a) Target 1

(b) Target 2

(c) Target 3

Figure 6.6: The best-fitting templates and SEDs for the targets after including the binned spectra in the fitting process.

The spectrum for object 1, however, shows continuum with good signal to noise and a drop in flux in the two bluest redshift bins. This drop is seen in the 2D spectrum also, and does not follow the fall off in throughput of the instrument. When compared to the photometry in the spectro-photometric fit, it is worrying to see that both points are systematically lower than the fitted SED, though they do agree within the errors.

There is not yet sufficient evidence to spectroscopically confirm the cluster. Photometric redshift estimates for these three potential cluster members are discrepant, though all agree that the 4000Å break should sit between the z* and the J-band, and the best quality spectro-photometric fit indicates a redshift of $1.8867^{+0.0034}_{-0.0117}$ for that particular potential member. Y-band imaging and further spectroscopic observations are needed to further this investigation though the current evidence does not support the hypothesis that these three objects belong to a cluster, with their varying photometric redshift solutions.

6.6 Observing faint continuum sources with FMOS

Spectroscopy of faint continuum sources is difficult, especially in the near-infrared where you have bright sky emission and broad telluric absorption features. With traditional slit spectroscopy, the best results for stacking observations of very faint sources has been achieved by placing the star to be used for telluric correction at the position that you want the object to be on the slit, and nodding between object and star. This provides a stellar trace for each observation of the object that can be seen and detected, where the object is not yet visible. This can be used in stacking to find the exact offset between the sky-subtraction nod that places the object at a different position along the slit, where otherwise you only have the approximate offset provided by the telescope telemetry.

The sky subtraction technique also has a huge impact on the quality of the stacked spectrum, with the ABB'A' technique providing the best handle on systematics as the subsequent nods sample different places on the detector. These systematics are usually not noticeable as they are smaller than the poisson noise and readnoise of the detectors, but when stacking many observations they become important. Imperfect flat-fielding is one possible cause, especially if you are first removing the spectral shape of the flat field.

Fibre spectroscopy takes out the difficulty of finding the faint source on the detector as the traces are defined in the fibre flat field. Changing which fibres are on the target could also help to mitigate some of

the systematics that the ABB'A' strategy takes care of. Stars can also be targeted simultaneously with the objects for telluric absorption correction thanks to the multiplicity of the fibre-fed system. The problems to be faced by FMOS for targeting continuum are different, the biggest ones being:

- Accuracy of flux calibration and correction of wavelength-dependent differences in fibre-fibre throughput.
- Sky subtraction.

Without improvement on the sky subtraction, continuum observations of faint sources will not be possible. Figure 5.2 shows this, with the systematics in sky-line residuals preventing the reduction in noise afforded by stacking in most of the H-band. Given the possibilities of Poisson-limited sky subtraction offered by using PCA fitting to the sky lines (Sharp & Parkinson, 2010), these types of observations may be possible in the future, given an aligned OH-mask or a large enough set of observations to use as a training set for the routine.

Chapter 7

Conclusions

7.0.1 RSD target selection

The target selection for a redshift survey designed to measure redshift space distortions depends heavily on the available broad-band photometric data available and over what areas. For conducting observations with FMOS in cross-beam switch mode we require a minimum surface density of objects at ~ 1000 per square degree, for beam-switching or dedicated fibre sky-subtraction, ~ 2000 objects per square degree is optimal. In Chapter 3, I use the band-merged photometric catalogue for the UDS field to look at how best to select galaxies in the redshift range $1.4 < z_{spec} < 1.7$, comparing colour selections to photometric redshift estimates. From this I find that B-z-K and B-z-ch1 colour selections perform poorly at isolating galaxies in the tight redshift range, peaking at a success of $\sim 20-25\%$ for both selections. The comparison of photometric redshift estimates to spectroscopic estimates, however, indicate a success rate of $\sim 50\%$, for the depths afforded in the UDS.

When considering different target fields from which to draw the target population, I find that the depth and coverage afforded by SWIRE, for the regions with full depth in the UKIDSS-DXS image, and full set of optical filters, a comparable success rate of photometric redshifts is reached. Including Spitzer IRAC filters does not improve the photometric redshift estimates in this case. In the absence of the U/B-band and the z-band the IRAC bands do improve the photometric redshift estimates and a redshift success rate of $\sim 42\%$ is reached. This would allow the use of the Lockman hole field, which has no z-band imaging, though the selection mechanism for all fields should be consistent and so if this were the case then all fields should have

targets selected without use of the z-band images.

Given the number density of sources from the catalogue with full K-band depth and full filter coverage reaches 1000 objects per square degree at a B-band magnitude of 25 (AB), an area of at least 60 square degrees would be required, assuming that half of these will give you a redshift in the correct range, which is optimistic given that the fraction of objects with emission line flux falling below the observable flux limit has not yet been truly modeled and accounted for. The SWIRE survey is therefore too small, though the wavelength coverage is good.

Looking at the CFHTLS survey, with the inclusion of IRAC ch1 and ch2 photometry a photometric redshift success rate of $\sim 38\%$ can be reached. Without deeper z-band data to select the catalogues from, however, the number density of sources is again too low.

7.0.2 FMOS performance

The UDS was targeted by FMOS in October and November 2009, employing beam-switching for the method of sky subtraction. The data taken in October 2009 displayed problems in fibre positioning, which was corrected for in the data taken in December 2009 by correcting the field configuration after every pair of sky+object frames. The absolute flux calibration of continuum for point sources was found to be accurate to $\sim 11\%$ for the December data, with the accuracy limited by the form of flat field frames taken with these observations. Flat-field frames should be taken with the spines configured in the field positions to account for variation in fibre throughput with fibre tilt.

The noise in the data is sky-subtraction limited due to the miss-alignment of the OH-suppression mask. Despite this, FMOS has secured 70 redshifts for the targets, with 23 of these not having previously been assigned a spectroscopic redshift.

7.0.3 Spectroscopic targeting of HiZELS

Using HiZELS narrow-band flux measurements to provide an absolute flux calibration, we find that objects with total SFR of $\sim 23 M_{\odot}$ have been observed with S/N$\sim 7-9$ in 1.5 hours, where the spread is dependent on the surface brightness of Hα and hence what fraction is observed through the fibre aperture. Although robust estimates were only found for two of the HiZELS objects, this provides a valuable measure for the

true performance of FMOS for sources that are not points and for line widths that are partially resolved.

7.0.4 JKCS 041

Long-slit spectroscopy of JKCS 041 has provided a tighter constraint on the photometric redshift of the possible cluster, at $1.8867^{+0.0034}_{-0.0117}$. Poor signal to noise and high systematics in the spectra of the other two targets prevented secure redshifts to be determined, although they indicate quite a large spread in redshift (one object at ~ 1.48, one at ~ 1.75, further spectroscopic targeting is required to securely confirm that the X-ray detection is indeed associated with a cluster at high redshift. The presented spectro-photometric fits, however, do not support the hypothesis that these objects belong to a cluster.

Although fibre spectroscopy with FMOS would solve some difficulties involved with targeting faint continuum sources, namely the knowledge of where on the detector the spectrum is positioned, the systematics introduced at the stage of sky-subtraction need to be much reduced before any sort of stacking can be performed on FMOS spectra. Given probable improvements offered by the PCA method of sky subtraction, this possibility should be investigated further in the future. If one were to try to mitigate some of the systematics introduced by flat-fielding/extracting the spectrum from the same position on the detector then the object could be observed through more than one fibre, though then the fibre:fibre throughput calibrations need to be more accurately measured and corrected using a flat field with the fibres configured to their observing positions.

Chapter 8

Current and Future Work

In November 2010, FMOS is targeting objects in the UDS over 10 nights of GTO time. This will provide the perfect data set to fully test the different selection mechanisms for choosing the targets for the redshift survey. Given a large number of observations with the spectrograph in a stable configuration will provide the perfect training set for testing PCA sky-subtraction methods, whether the OH-suppression mask is aligned or not.

Within the target sample is the full sample of $\sim$ 150 HiZELS nbH-selected objects from the UDS field. Given improved sky subtraction, stable fibre configurations (compared to the observations taken in October 2009) we expect an improved redshift success rate for these objects. This will provide a statistical contamination rate of the sample from other emission lines, as well as the AGN contamination rate. With reduced systematic errors left from sky-subtraction, I will be stacking these sources to find the average Hα to Hβ ratio, to test whether the average dust properties of star-forming galaxies are any different at $z \sim 1.45$. Given a large enough sample of observed objects, this can be done in bins of Hα luminosity and compared to the extinction estimates derived by comparing $24\mu m$ SFR estimates to Hα-derived SFRs.

Appendix A

Expectation-Maximisation Algorithm

This Appendix describes the Expectation-Maximisation Algorithm used to calculate the final normalisations of convolved K-band profiles, and hence the IRAC fluxes. This algorithm was the basis for a program written in IDL that starts from predicted IRAC profiles (from K-band profiles convolved to the IRAC PSF) registered to the correct astrometry and pixel grid, and returns the fluxes for each object.

If you have μ_i expected counts at pixel i, defined by the prior information of all the overlapping object profiles at that pixel ($h_{k,i}$), and the background value, b, at that pixel (Equation A.1) then α_k is the normalisation of the profile of object k.

$$\mu_i = \Sigma_{k=1}^{K} \alpha_k h_{k,i} + b \tag{A.1}$$

The probability, P of measuring the observed number of counts, x_i at that pixel is given by Equation A.2, following Poisson statistics.

$$P = \{X_i = x_i\} = exp(-\mu_i)\frac{\mu_i^{x_i}}{x_i!} \tag{A.2}$$

Then the likelihood for the entire image of M pixels is given by Equation A.3, since the probability for each pixel is assumed independent.

$$L(\mathbf{x},\mu) = \prod_{i=1}^{M} exp(-\mu_i)\frac{\mu_i^{x_i}}{x_i!} \tag{A.3}$$

This likelihood can then be maximised with respect to α_k (A.4,A.5).

$$\frac{\partial logL(\mathbf{x},\mu)}{\partial \alpha_k} = 0 = -\sum_{i=1}^{M} h_{k,i} + \sum_{i=1}^{M} x_i \frac{h_{k,i}}{\sum_{j=1}^{K} \alpha_j h_{j,i} + b} \tag{A.4}$$

$$\Rightarrow \sum_{i=1}^{M} h_{k,i} = \sum_{i=1}^{M} x_i \frac{h_{k,i}}{\sum_{j=1}^{K} \alpha_i h_{j,i} + b} \tag{A.5}$$

The best-fitting normalisation of each model profile can then be obtained by solving the set of non-linear equations iteratively (A.6,A.7)

$$\alpha_k^{(n+1)} = \alpha_k^{(n)} \frac{\sum_{i=1}^{M} (x_i/\mu_i^{(n)}) h_{k,i}}{\sum_{i=1}^{M} h_{k,i}} \tag{A.6}$$

$$\mu_i^{(n)} = \sum_{j}^{(n)} \alpha_j^{(n)} h_{j,i} + b \tag{A.7}$$

Appendix B

Identifying Stars

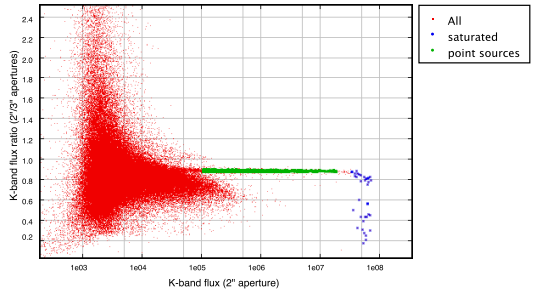

(a) Selection of point sources from the flux ratio between two different sized apertures

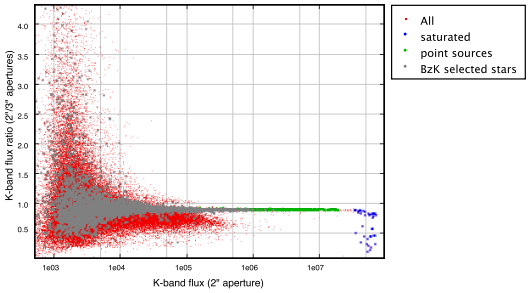

(b) Flux ratio vs flux for both BzK selected sources and point sources.

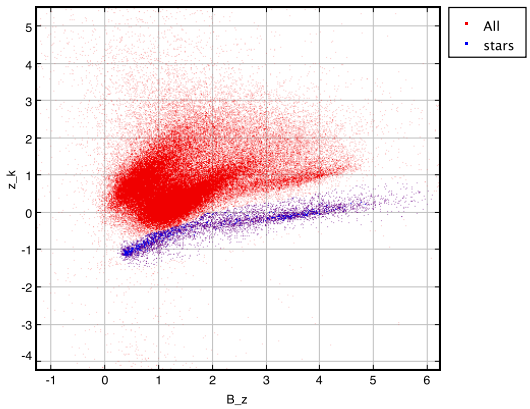

(c) B-z vs. z-K shows how stars are selected using the BzK selection.

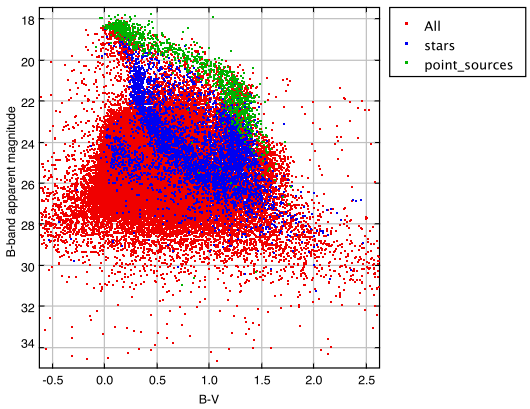

(d) B vs. B-V colour.

Figure B.1: Selection of stars from the UDS catalogue

The figure in this appendix (B.1) displays how stars are selected from both the BzK stellar locus (selected as in B.1 (c), (b) shows how these compare to the point sources chosen from the K-band flux ratio between 2" and 3" sized apertures) (Daddi et al., 2004) and from the flux ratio between two different sized apertures B.1 (a). B.1 (d) shows that the BzK selection primarily selects main-sequence stars, while the flux ratio mainly selects red giants, which are much brighter in K.

Appendix C

B-band magnitude

In this appendix the results for the scaled masses and observed B-band magnitudes are recorded for a range of star formation histories, ages and extinction. Each mass and B-band magnitude is that required to produce the limiting Hα flux of 1E-16 erg s$-$1 cm$-$2 (see section 3.3.1). If the final scaling required to reach this limiting flux produces a final stellar mass that is too high, the entry is crossed out and discounted as unphysical. This is a very simplified demonstration of how the observed B-band magnitude of a galaxy is linked to the extinction and Hα flux. Only the star forming population is considered here, the mass of a galaxy is not directly linked to the UV continuum since it is the longer lived, lower mass stellar population that dominates the mass of a galaxy, however this population does not affect the Hα flux or the UV continuum. In reality the galaxy mass is likely to be made up from many star formation episodes.

Extinction E(B-V)				0		0.1		0.2		0.3		0.4		0.5	
tau	Age now (Gyr)	redshift	age at redshift (Gyr)	scaled mass ($M_\odot$)	apparent B-band magnitude (AB)	mass	B-band	mass	B-band	mass	B-band	mass	B-band	mass	B-band
~~0.1~~	~~9.72~~	~~1.4~~	~~0.7~~	~~8.5320e+11~~	~~21.691~~										
0.1	9.72	1.7	0.006	9.8754e+07	23.7	2.224E08	23.8	2.3796E08	24.8	3.6986E08	25.3	5.7415e+08	25.8	8.8967e+08	26.3
~~0.1~~	~~11~~	~~1.4~~	~~1.98~~	~~6.2132e+12~~	~~23.991~~										
~~0.1~~	~~11~~	~~1.7~~	~~1.286~~	~~5.5128e+12~~	~~24.047~~										
~~0.1~~	~~12~~	~~1.4~~	~~2.98~~	~~6.9052e+12~~	~~24.844~~										
~~0.1~~	~~12~~	~~1.7~~	~~2.286~~	~~9.2639e+12~~	~~25.154~~										
0.3	9.72	1.4	0.7	2.2659e+10	23.2	5.1034e+10	23.2	5.4600e+10	24.1	8.4865e+10	24.5	1.3174e+11	25.0	2.0413e+11	25.4
0.3	9.72	1.7	0.006	9.8007e+07	23.6	2.2074e+08	23.7	2.3616e+08	24.6	3.6707e+08	25.1	5.6981e+08	25.6	8.8294e+08	26.1
~~0.3~~	~~11~~	~~1.4~~	~~1.98~~	~~1.2950e+12~~	~~23.128~~										
0.3	11	1.7	1.286	2.3889e+11	23.1	5.3804e+11	23.2	5.7564e+11	24.1	~~8.9472e+11~~	~~24.6~~				
~~0.3~~	~~12~~	~~1.4~~	~~2.98~~	~~5.7379e+12~~	~~24.265~~										
~~0.3~~	~~12~~	~~1.7~~	~~2.286~~	~~4.0882e+12~~	~~23.491~~										
0.7	9.72	1.4	0.7	9.7256e+09	23.3	2.1904e+10	23.3	2.3435e+10	24.2	3.6425e+10	24.6	5.6544e+10	25.1	8.7618e+10	25.5
0.7	9.72	1.7	0.006	9.7788e+07	23.5	2.2024e+08	23.6	2.3563e+08	24.5	3.6625e+08	25.1	5.6853e+08	25.6	8.8097e+08	26.1
0.7	11	1.4	1.98	8.1635e+10	23.2	1.8386e+11	23.3	1.9671e+11	24.1	3.0575e+11	24.6	4.7462e+11	25.0	7.3545e+11	25.5
0.7	11	1.7	1.286	4.3845e+10	23.2	9.8750e+10	23.3	1.0565e+11	24.2	1.6421e+11	24.7	2.5491e+11	25.2	3.9500e+11	25.7
0.7	12	1.4	2.98	3.3268e+11	23.3	7.4928e+11	23.3	~~8.0164e+11~~	~~24.2~~						
0.7	12	1.7	2.286	2.0324e+11	23.2	4.5775e+11	23.3	4.8973e+11	24.2	~~7.6120e+11~~	~~24.7~~				
1	9.72	1.4	0.7	8.2087e+09	23.3	1.8488e+10	23.4	1.9780e+10	24.2	3.0744e+10	24.7	4.7725e+10	25.1	7.3952e+10	25.6
1	9.72	1.7	0.006	9.7758e+07	23.5	2.2017e+08	23.6	2.3556e+08	24.5	3.6613e+08	25.0	5.6836e+08	25.6	8.8070e+08	26.1
1	11	1.4	1.98	4.6148e+10	23.3	1.0394e+11	23.3	1.1120e+11	24.2	1.7284e+11	24.6	2.6830e+11	25.1	4.1575e+11	25.5
1	11	1.7	1.286	3.1469e+10	23.2	7.0876e+10	23.3	7.5829e+10	24.2	1.1786e+11	24.7	1.8296e+11	25.2	2.8350e+11	25.7
1	12	1.4	2.98	1.3209e+11	23.3	2.9750e+11	23.3	3.1829e+11	24.2	4.9472e+11	24.6	7.6796e+11	25.1	1.1900e+12	25.5
1	12	1.7	2.286	1.0341e+11	23.2	2.3290e+11	23.3	2.4918e+11	24.2	3.8730e+11	24.7	6.0122e+11	25.2	9.3162e+11	25.7
3	9.72	1.4	0.7	6.4154e+09	23.3	1.4449e+10	23.4	1.5459e+10	24.2	2.4029e+10	24.7	3.7299e+10	25.1	5.7796e+10	25.6
3	9.72	1.7	0.006	9.7679e+07	23.5	2.1999e+08	23.6	2.3537e+08	24.5	3.6583e+08	25.0	5.6790e+08	25.5	8.7999e+08	26.0
3	11	1.4	1.98	2.1129e+10	23.3	4.7588e+10	23.4	5.0913e+10	24.2	7.9135e+10	24.7	1.2284e+11	25.1	1.9035e+11	25.6
3	11	1.7	1.286	1.9743e+10	23.2	4.4466e+10	23.3	4.7573e+10	24.2	7.3944e+10	24.7	1.1478e+11	25.3	1.7786e+11	25.8
3	12	1.4	2.98	3.7245e+10	23.3	8.3885e+10	23.4	8.9747e+10	24.2	1.3949e+11	24.7	2.1654e+11	25.1	3.3554e+11	25.6
3	12	1.7	2.286	4.1151e+10	23.2	9.2682e+10	23.3	9.9159e+10	24.2	1.5412e+11	24.7	2.3925e+11	25.2	3.7073e+11	25.8
5	9.72	1.4	0.7	6.1238e+09	23.3	1.3792e+10	23.4	1.4756e+10	24.2	2.2935e+10	24.7	3.5603e+10	25.1	5.5169e+10	25.6
5	9.72	1.7	0.006	9.7665e+07	23.5	2.1997e+08	23.6	2.3533e+08	24.5	3.6579e+08	25.0	5.6782e+08	25.5	8.7986e+08	26.0
5	11	1.4	1.98	1.8405e+10	23.3	4.1453e+10	23.4	4.4349e+10	24.2	6.8932e+10	24.7	1.0700e+11	25.1	1.6581e+11	25.6
5	11	1.7	1.286	1.8125e+10	23.2	4.0822e+10	23.3	4.3675e+10	24.2	6.7884e+10	24.7	1.0538e+11	25.3	1.6329e+11	25.8
5	12	1.4	2.98	2.9992e+10	23.3	6.7549e+10	23.4	7.2270e+10	24.2	1.1233e+11	24.7	1.7437e+11	25.1	2.7020e+11	25.6
5	12	1.7	2.286	3.5039e+10	23.2	7.8917e+10	23.3	8.4431e+10	24.2	1.3123e+11	24.7	2.0371e+11	25.3	3.1567e+11	25.8
15	9.72	1.4	0.7	5.8491e+09	23.4	1.3174e+10	23.4	1.4094e+10	24.3	2.1907e+10	24.7	3.4006e+10	25.1	5.2694e+10	25.6
15	9.72	1.7	0.006	9.7654e+07	23.5	2.1994e+08	23.6	2.3531e+08	24.5	3.6574e+08	25.0	5.6775e+08	25.5	8.7976e+08	26.0
15	11	1.4	1.98	1.6147e+10	23.3	3.6367e+10	23.4	3.8908e+10	24.2	6.0476e+10	24.7	9.3878e+10	25.1	1.4547e+11	25.6
15	11	1.7	1.286	1.6688e+10	23.2	3.7585e+10	23.3	4.0212e+10	24.2	6.2502e+10	24.8	9.7023e+10	25.3	1.5034e+11	25.8
15	12	1.4	2.98	2.4521e+10	23.3	5.5227e+10	23.4	5.9087e+10	24.2	9.1839e+10	24.7	1.4256e+11	25.1	2.2091e+11	25.6
15	12	1.7	2.286	3.0110e+10	23.2	6.7815e+10	23.3	7.2554e+10	24.2	1.1277e+11	24.8	1.7506e+11	25.3	2.7126e+11	25.8
				Brightest	23.1		23.2		24.1		24.5		25.0		25.4
				Faintest	23.6		23.8		24.8		25.3		25.8		26.3
				Mean	23.3	1.05E11	23.4	1.12E11	24.3	1.42E11	24.8	1.51E11	25.2	3.91E11	25.0

Table C.1: This table shows the stellar masses and observed B-band magnitudes for stellar populations providing Hα emission of 1E-16 erg s^{-1} cm^{-2} for various star formation histories.

Appendix D

FMOS spectroscopic redshifts

Aperture	Ra	Dec	Prev Spec-z	Hα spec-z	quality	observed lines
3	34.62392	-4.95303	0.705	0.705	5	Bright Hα+NII
15	34.61083	-5.00217	1.047	agreeish	4	Ha next to slit
17	34.63192	-5.03881	0.712	agree	2	Ha and SII but in messy region
21						see HiZELS
26	34.5395	-4.996	1.095	agree	4	Huge OIII, SII
27	34.53362	-4.9505	0.711	agree	4	good Ha SII
48	34.53875	-5.03969	1.018	agree	4	good Ha, OII into noisy region
50	34.56242	-5.06903	1.2	1.388	1	looks more like Ha with poss Hb than AGN
68	34.43225	-4.87411	0.875	agree	4	good Ha
77	34.39512	-4.81689	0.881	agree	4	good Ha SII
86	34.46142	-5.0275	0.706	agree	2	Ha
89	34.46217	-5.12097	n/a	1.17	4	Hb, Ha, NII, OIII (1)
102	34.37892	-5.02778	0.801	agree	Ha	
110	34.32792	-4.87389	n/a	1.32	3	broad Ha, Hb, OIII (1)
118	34.29225	-4.87	1.03 (p)	$\sim$0.99	2	Ha
128	34.37983	-5.11925	1.27	agree	4	Ha+large NII, OIII (1)
132	34.40667	-5.19881	0.921	agree	2	Ha
166	34.29562	-5.12797	0.824	agree	3	paritally masked, bright Ha
173	34.2785	-5.22517	0.626	agree	3	bright Ha

Table D.1: October observations, IRS1

Aperture	Ra	Dec	Prev Spec-z	Hα spec-z	quality	observed lines
9	34.53571	-5.20678	1.036	agree	3	Ha
14	34.43862	-5.28336	n/a	0.915	2	Ha
16	34.37038	-5.29819	0.786	agree	2	Ha
25	34.38354	-5.22561	1.342	agree	4	bright, broad Ha, NII
27	34.40667	-5.19881	0.921	agree	3	Ha, NII
32	34.53846	-5.12411	n/a	1.406	3	Ha, partially masked Hb
34	34.56533	-5.08622	n/a	1.495	3	Ha, NII, SII
36	34.57329	-5.06633	n/a	1.457	2	Ha, NII, poss Hb
51	34.26525	-5.25822	0.807	agree	3	Ha
52	34.27129	-5.27481	0.809	agree	3	broad Ha, NII
54	34.18592	-5.27364	0.758	agree	3	Ha
58	34.24167	-5.21186	0.896	agree	3	Ha
65	34.37983	-5.11925	1.27	agree	3	good Ha, NII, poss OII, Hb
76	34.51438	-5.01822	1.044	agree	4	Ha, OII, Hb into noisy region
79	34.46271	-5.05081	0.873	agree	3	Ha, SII
86	34.32283	-5.16761	1.03	1.033	3	Ha
90	34.17154	-5.22172	1.053	agree	3	Ha near slit
94	34.12371	-5.21389	n/a	1.44	4	Ha, OIII, Hb
104	34.32733	-5.04436	0.822	agree	2	partially masked Ha
130	34.16296	-5.14297	n/a	1.474	2	Ha and poss OII (1)
132	34.12312	-5.16219	HiZELS nbJ	0.855	3	Ha
135	34.09579	-5.13506	2.09	agree	4	Huge OII emission, small amt OII?
149			1.445	1.449	5	Ha, OIII
153	34.45088	-4.86392	1.602	1.605	3	OIII
155	34.43488	-4.86522	0.707	agree	3	ha
156	34.38162	-4.88819	n/a	1.405	3	ha, hb, OIII, all faint
160	34.31804	-4.95325	1.18	agree	5	ha, OIII
184	34.32792	-4.87389	1.319	agree	4	broad ha, poss hb
186	34.35429	-4.84364	1.479	agree	4	Ha, hb
196	34.17517	-4.93317	0.6	agree	4	bright Ha

Table D.2: December observations, IRS1

Aperture	Ra	Dec	Prev Spec-z	Hα spec-z	quality	observed lines
15			n/a	1.49	1	possible Ha
67			1.026	agree	5	broad Ha/NII near slit
74			0.995 (p)	0.895	3	Ha,NII
96			0.806	agree	4	Ha,NII
104			0.805	agree	4	Ha
112			1.42	agree	4	broad Ha
117			0.981	agree	4	broad Ha
126			0.714	agree	5	good continuum, Huge Ha/NII, very broad
141			1.382	1.389	2	Ha+Hb

Table D.3: December observations, IRS2

Appendix E

Measurements of cosmic SFR compiled by Hopkins (2004)

The following table documents the work done by many different authors to contribute to the understanding of the form of the cosmic SFR. This list is not exhaustive and only includes the measurements compiled in Hopkins (2004).

Reference	SFR estimator	Redshift
Giavalisco et al. (2004)	1500Å	3 points over range $\sim 3.780 - 5.74$
Wilson et al. (2002)	2500Å	3 points over range $\sim 0.350 - 1.35$
Massarotti et al. (2001)	1500Å	3 points over range $\sim 1.500 - 4.000$
Sullivan et al. (2000)	2000Å	0.150 *pm* 0.150
Steidel et al. (1999)	1700Å	2 points $\sim 3.040 - 4.130$
Cowie et al. (1999)	2000Å	2 points $\sim 0.700 - 1.250$
Treyer et al. (1998)	2000Å	0.150 ± 0.150
Connolly et al. (1997)	2800Å	3 points over range $\sim 0.750 - 1.750$
Lilly et al. (1996)	2800Å	3 points over range$\sim 0.350 - 0.875$
Madau et al. (1996)	1600Å	2 points over range$\sim 2.750 - 4.000$
Teplitz et al. (2003)	[OII]	0.900 ± 0.500
Gallego et al. (2002)	[OII]	0.025 ± 0.025
Hogg et al. (1998)	[OII]	11 points over range $\sim 0.200 - 1.2$
Hammer et al. (1997)	[OII]	3 points over range $\sim 0.375 - 0.875$
Pettini et al. (1998)	Hβ	2.750 ± 0.750
PŐrez-GonzĞlez et al. (2003)	Hα	0.025 ± 0.025
Tresse et al. (2002)	Hα	$0.700^{+0.400}_{-0.200}$
Moorwood et al. (2000)	Hα	2.200 ± 0.050
Hopkins et al. (2000)	Hα	1.250 ± 0.550
Sullivan et al. (2000)	Hα	0.150 ± 0.150
Glazebrook et al. (1999)	Hα	0.900 ± 0.100
Yan et al. (1999)	Hα	1.300 ± 0.600
Tresse & Maddox (1998)	Hα	0.200 ± 0.100
Gallego et al. (1995)	Hα	0.022 ± 0.022
Flores et al. (1999)	$15\mu m$	3 points over range $\sim 0.350 - 0.875$
Barger et al. (2000)	$850\mu m$	2 points over range $\sim 2.000 - 4.500$
Hughes et al. (1998)	$850\mu m$	3.000 ± 1.000
Condon et al. (2002)	1.4GHz	0.005 ± 0.005
Sadler et al. (2002)	1.4GHz	0.080 ± 0.080
Serjeant et al. (2002)	1.4GHz	0.010 ± 0.010
Machalski & Godlowshki (2000)	1.4GHz	0.070 ± 0.070
Haarsma et al. (2000)	1.4GHz	5 points over range $\sim 0.280 - 1.6$
Condon (1989)	1.4GHz	0.005 ± 0.005
Sadler et al. (2002)	1.4GHz	0.080 ± 0.080
Serjeant et al. (2002)	1.4GHz	0.010 ± 0.010
Machalski & Godlowshki (2000)	1.4GHz	0.070 ± 0.070
Haarsma et al. (2000)	1.4GHz	5 points over range $\sim 0.280 - 1.6$
Condon (1989)	1.4GHz	0.005 ± 0.005
Georgakakis et al. (2003)	X-ray(0.5-2keV)	$0.24^{+0.06}_{-0.24}$

Table E.1: The references for the cosmic SFR measurements contributing to the picture of how this varies with redshift, as compiled by Hopkins (2004)

Bibliography

ABDALLA, F. B., BANERJI, M., LAHAV, O. & RASHKOV, V., 2008. A Comparison of Six Photometric Redshift Methods Applied to 1.5 Million Luminous Red Galaxies. eprint arXiv:0812.3831. URL http://adsabs.harvard.edu/abs/2008arXiv0812.3831A.

AMENDOLA, L., 2000. Perturbations in a coupled scalar field cosmology. Monthly Notices of the Royal Astronomical Society, **312**(3), 521–530. ISSN 0035-8711. URL http://adsabs.harvard.edu/abs/2000MNRAS.312..521A.

ANDREON, S., MAUGHAN, B., TRINCHIERI, G. & KURK, J., 2009. JKCS 041: a colour-detected galaxy cluster at z phot ˜ 1.9 with deep potential well as confirmed by X-ray data. Astronomy and Astrophysics, **507**(1), 147–157. ISSN 0004-6361. URL http://adsabs.harvard.edu/abs/2009A&A...507..147A.

BALDWIN, J. A., PHILLIPS, M. M. & TERLEVICH, R., 1981. Classification parameters for the emission-line spectra of extragalactic objects. Publications of the Astronomical Society of the Pacific, **93**, 5. ISSN 0004-6280. URL http://adsabs.harvard.edu/abs/1981PASP...93....5B.

BERTIN, E., 2006. SExtractor User Manual.

BEST, P., SMAIL, I., SOBRAL, D., GEACH, J., GARN, T., IVISON, R., KURK, J., DALTON, G., CIRASUOLO, M. & CASALI, M., 2010. HiZELS: the High Redshift Emission Line Survey with UKIRT. eprint arXiv:1003.5183. URL http://adsabs.harvard.edu/abs/2010arXiv1003.5183B.

BOLZONELLA, M., MIRALLES, J.-M. & PELLÓ, R., 2000. Photometric redshifts based on standard SED fitting procedures. Astronomy and Astrophysics. URL http://adsabs.harvard.edu/abs/2000A%26A...363..476B.

BOWER, R. G., BENSON, A. J., MALBON, R., HELLY, J. C., FRENK, C. S., BAUGH, C. M., COLE, S. & LACEY, C. G., 2006. Breaking the hierarchy of galaxy formation. Monthly Notices of the Royal Astronomical Society, **370**(2), 060616014113004–??? ISSN 0035-8711. URL http://adsabs.harvard.edu/abs/2006MNRAS.370..645B.

BRUZUAL, G. & CHARLOT, S., 2003. Stellar population synthesis at the resolution of 2003. Monthly Notices of the Royal Astronomical Society, **344**(4), 1000–1028. ISSN 0035-8711. URL http://adsabs.harvard.edu/abs/2003MNRAS.344.1000B.

BUNDY, K., ELLIS, R. S., CONSELICE, C. J., TAYLOR, J. E., COOPER, M. C., WILLMER, C. N. A., WEINER, B. J., COIL, A. L., NOESKE, K. G. & EISENHARDT, P. R. M., 2006.

The Mass Assembly History of Field Galaxies: Detection of an Evolving Mass Limit for Star-Forming Galaxies. The Astrophysical Journal, **651**(1), 120–141. ISSN 0004-637X. URL http://adsabs.harvard.edu/abs/2006ApJ...651..120B.

CALZETTI, D., 1997. Reddening and Star Formation in Starburst Galaxies. The Astronomical Journal, **113**, 162. ISSN 00046256. URL http://adsabs.harvard.edu/abs/1997AJ....113..162C.

CALZETTI, D., ARMUS, L., BOHLIN, R. C., KINNEY, A. L., KOORNNEEF, J. & STORCHI-BERGMANN, T., 2000. The Dust Content and Opacity of Actively Star-forming Galaxies. The Astrophysical Journal, **533**(2), 682–695. ISSN 0004-637X. URL http://adsabs.harvard.edu/abs/2000ApJ...533..682C.

CAPOZZIELLO, S., CARDONE, V. F. & TROISI, A., 2005. Reconciling dark energy models with f(R) theories. Physical Review D, **71**(4). ISSN 1550-7998. URL http://adsabs.harvard.edu/abs/2005PhRvD..71d3503C.

CASALI, M., ADAMSON, A., ALVES DE OLIVEIRA, C., ALMAINI, O., BURCH, K. ET AL., 2007. The UKIRT wide-field camera. Astronomy and Astrophysics, **467**(2), 777–784. ISSN 0004-6361. URL http://adsabs.harvard.edu/abs/2007A&A...467..777C.

CEN, R. & OSTRIKER, J. P., 2006. Where Are the Baryons? II. Feedback Effects. The Astrophysical Journal, **650**(2), 560–572. ISSN 0004-637X. URL http://adsabs.harvard.edu/abs/2006ApJ...650..560C.

COLEMAN, G. D., WU, C.-C. & WEEDMAN, D. W., 1980. Colors and magnitudes predicted for high redshift galaxies. The Astrophysical Journal Supplement Series, **43**, 393. ISSN 0067-0049. URL http://adsabs.harvard.edu/abs/1980ApJS...43..393C.

COLLESS, M., DALTON, G., MADDOX, S., SUTHERLAND, W., NORBERG, P. ET AL., 2001. The 2dF Galaxy Redshift Survey: spectra and redshifts. Monthly Notices of the Royal Astronomical Society, **328**(4), 1039–1063. ISSN 00358711. URL http://adsabs.harvard.edu/abs/2001MNRAS.328.1039C.

COLLISTER, A. A. & LAHAV, O., 2004. ANN z : Estimating Photometric Redshifts Using Artificial Neural Networks. Publications of the Astronomical Society of the Pacific, **116**(818), 345–351. ISSN 0004-6280. URL http://adsabs.harvard.edu/abs/2004PASP..116..345C.

COOPER, M. C., NEWMAN, J. A., COIL, A. L., CROTON, D. J., GERKE, B. F., YAN, R., DAVIS, M., FABER, S. M., GUHATHAKURTA, P., KOO, D. C., WEINER, B. J. & WILLMER, C. N. A., 2007. The DEEP2 galaxy redshift survey: evolution of the colour-density relation at $0.4 < z < 1.35$. Monthly Notices of the Royal Astronomical Society, **376**(4), 1445–1459. ISSN 0035-8711. URL http://adsabs.harvard.edu/abs/2007MNRAS.376.1445C.

COOPER, M. C., NEWMAN, J. A., CROTON, D. J., WEINER, B. J., WILLMER, C. N. A., GERKE, B. F., MADGWICK, D. S., FABER, S. M., DAVIS, M., COIL, A. L., FINKBEINER, D. P., GUHATHAKURTA, P. & KOO, D. C., 2006. The DEEP2 Galaxy Redshift Survey: the relationship between galaxy properties and environment at z ˜ 1. Monthly Notices of the Royal Astronomical Society, **370**(1), 060615023248011–??? ISSN 0035-8711. URL http://adsabs.harvard.edu/abs/2006MNRAS.370..198C.

COWIE, L. L., SONGAILA, A., HU, E. M. & COHEN, J. G., 1996. New Insight on Galaxy Formation and Evolution From Keck Spectroscopy of the Hawaii Deep Fields. The Astronomical Journal, **112**, 839. ISSN 00046256. URL http://adsabs.harvard.edu/abs/1996AJ....112..839C.

CUCCIATI, O., IOVINO, A., MARINONI, C., ILBERT, O., BARDELLI, S. ET AL., 2006. The VIMOS VLT Deep Survey: the build-up of the colour-density relation. Astronomy and Astrophysics, **458**(1), 39–52. ISSN 0004-6361. URL http://adsabs.harvard.edu/abs/2006A%26A...458...39C.

DADDI, E., CIMATTI, A., RENZINI, A., FONTANA, A., MIGNOLI, M., POZZETTI, L., TOZZI, P. & ZAMORANI, G., 2004. A New Photometric Technique for the Joint Selection of Star-forming and Passive Galaxies at 1.4 â< z â< 2.5. The Astrophysical Journal, **617**(2), 746–764. ISSN 0004-637X. URL http://adsabs.harvard.edu/abs/2004ApJ...617..746D.

DE LUCIA, G. & BLAIZOT, J., 2007. The hierarchical formation of the brightest cluster galaxies. Monthly Notices of the Royal Astronomical Society, **375**(1), 2–14. ISSN 0035-8711. URL http://adsabs.harvard.edu/abs/2007MNRAS.375....2D.

DE SANTIS, C., GRAZIAN, A., FONTANA, A. & SANTINI, P., 2007. ConvPhot: A profile-matching algorithm for precision photometry. New Astronomy, **12**(4), 271–288. ISSN 13841076. URL http://adsabs.harvard.edu/abs/2007NewA...12..271D.

DOHERTY, M., BUNKER, A., SHARP, R., DALTON, G., PARRY, I. & LEWIS, I., 2006. The star formation rate at redshift one: Halpha spectroscopy with CIRPASS. Monthly Notices of the Royal Astronomical Society, **370**(1), 060615023248002–??? ISSN 0035-8711. URL http://adsabs.harvard.edu/abs/2006MNRAS.370..331D.

DOHERTY, M., BUNKER, A., SHARP, R., DALTON, G., PARRY, I., LEWIS, I., MACDONALD, E., WOLF, C. & HIPPELEIN, H., 2004. Multi-object near-infrared Hα spectroscopy of z $\sim$ 1 star-forming galaxies in the Hubble Deep Field North. Monthly Notices of the Royal Astronomical Society, **354**(1), L7–L12. ISSN 00358711. URL http://adsabs.harvard.edu/abs/2004MNRAS.354L...7D.

DRESSLER, A., 1980. Galaxy morphology in rich clusters - Implications for the formation and evolution of galaxies. The Astrophysical Journal, **236**, 351. ISSN 0004-637X. URL http://adsabs.harvard.edu/abs/1980ApJ...236..351D.

DRINKWATER, M. J., JUREK, R. J., BLAKE, C., WOODS, D., PIMBBLET, K. A. ET AL., 2010. The WiggleZ Dark Energy Survey: survey design and first data release. Monthly Notices of the Royal Astronomical Society, **401**(3), 1429–1452. ISSN 00358711. URL http://adsabs.harvard.edu/abs/2010MNRAS.401.1429D.

DUNLOP, J., AKIYAMA, MASAYUKI, ALEXANDER, DAVID, ALMAINI, OMAR, BORYS, COLIN ET AL., 2007. A Spitzer Public Legacy survey of the UKIDSS Ultra Deep Survey. Spitzer Proposal ID #40021. URL http://adsabs.harvard.edu/abs/2007sptz.prop40021D.

DVALI, G., 2000. 4D gravity on a brane in 5D Minkowski space. Physics Letters B, **485**(1-3), 208–214. ISSN 03702693. URL http://adsabs.harvard.edu/abs/2000PhLB..485..208D.

DYE, S., WARREN, S. J., HAMBLY, N. C., CROSS, N. J. G., HODGKIN, S. T. ET AL., 2006. The UKIRT Infrared Deep Sky Survey Early Data Release. Monthly Notices of the Royal Astronomical Society, **372**(3), 1227–1252. ISSN 0035-8711. URL http://adsabs.harvard.edu/abs/2006MNRAS.372.1227D.

FABER, S. M., WILLMER, C. N. A., WOLF, C., KOO, D. C., WEINER, B. J. ET AL., 2007. Galaxy Luminosity Functions to z ∼1 from DEEP2 and COMBO-17: Implications for Red Galaxy Formation. The Astrophysical Journal, **665**(1), 265–294. ISSN 0004-637X. URL http://adsabs.harvard.edu/abs/2007ApJ...665..265F.

FOUCAUD, S., ALMAINI, O., SMAIL, I., CONSELICE, C. J., LANE, K. P., EDGE, A. C., SIMPSON, C., DUNLOP, J. S., MCLURE, R. J., CIRASUOLO, M., HIRST, P., WATSON, M. G. & PAGE, M. J., 2007. Number counts and clustering properties of bright distant red galaxies in the UKIDSS Ultra Deep Survey Early Data Release. Monthly Notices of the Royal Astronomical Society: Letters, **376**(1), L20–L24. ISSN 1745-3925. URL http://doi.wiley.com/10.1111/j.1745-3933.2007.00278.x.

FURUSAWA, H., KOSUGI, G., AKIYAMA, M., TAKATA, T., SEKIGUCHI, K. ET AL., 2008. The Subaru/ XMM-Newton Deep Survey (SXDS). II. Optical Imaging and Photometric Catalogs1. The Astrophysical Journal Supplement Series, **176**(1), 1–18. ISSN 0067-0049. URL http://adsabs.harvard.edu/abs/2008ApJS..176....1F.

GARN, T. & BEST, P. N., 2010. Predicting dust extinction from the stellar mass of a galaxy. Monthly Notices of the Royal Astronomical Society, **409**(1), 421–432. ISSN 00358711. URL http://adsabs.harvard.edu/abs/2010MNRAS.tmp.1318G.

GARN, T., SOBRAL, D., BEST, P. N., GEACH, J. E., SMAIL, I., CIRASUOLO, M., DALTON, G. B., DUNLOP, J. S., MCLURE, R. J. & FARRAH, D., 2010. Obscured star formation at z = 0.84 with HiZELS: the relationship between star formation rate and Hα or ultraviolet dust extinction. Monthly Notices of the Royal Astronomical Society, **402**(3), 2017–2030. ISSN 00358711. URL http://adsabs.harvard.edu/abs/2010MNRAS.402.2017G.

GEACH, J. E., SMAIL, I., BEST, P. N., KURK, J., CASALI, M., IVISON, R. J. & COPPIN, K., 2008. HiZELS: a high-redshift survey of Hα emitters - I. The cosmic star formation rate and clustering at z = 2.23. Monthly Notices of the Royal Astronomical Society, **388**(4), 1473–1486. ISSN 00358711. URL http://adsabs.harvard.edu/abs/2008MNRAS.388.1473G.

GLADDERS, M. D. & YEE, H. K. C., 2000. A New Method For Galaxy Cluster Detection. I. The Algorithm. The Astronomical Journal, **120**(4), 2148–2162. ISSN 00046256. URL http://adsabs.harvard.edu/abs/2000AJ....120.2148G.

GLADDERS, M. D., YEE, H. K. C., MAJUMDAR, S., BARRIENTOS, L. F., HOEKSTRA, H., HALL, P. B. & INFANTE, L., 2007. Cosmological Constraints from the Red-Sequence Cluster Survey. The Astrophysical Journal, **655**(1), 128–134. ISSN 0004-637X. URL http://adsabs.harvard.edu/abs/2007ApJ...655..128G.

GUZZO, L., PIERLEONI, M., MENEUX, B., BRANCHINI, E., LE FÈVRE, O. ET AL., 2008. A test of the nature of cosmic acceleration using galaxy redshift distortions. Nature, **451**(7178), 541–4. ISSN 1476-4687. URL http://cdsads.u-strasbg.fr/abs/2008Natur.451..541G.

HAMBLY, N. C., COLLINS, R. S., CROSS, N. J. G., MANN, R. G., READ, M. A., SUTORIUS, E. T. W., BOND, I., BRYANT, J., EMERSON, J. P., LAWRENCE, A., RIMOLDINI, L., STEWART, J. M., WILLIAMS, P. M., ADAMSON, A., HIRST, P., DYE, S. & WARREN, S. J., 2008. The WFCAM Science Archive. Monthly Notices of the Royal Astronomical Society, **384**(2), 637–662. ISSN 00358711. URL http://adsabs.harvard.edu/abs/2008MNRAS.384..637H.

HANDBOOK, I. I., 2010. IRAC Instrument Handbook.

HAWKINS, E., MADDOX, S., COLE, S., LAHAV, O., MADGWICK, D. S. ET AL., 2003. The 2dF Galaxy Redshift Survey: correlation functions, peculiar velocities and the matter density of the Universe. Monthly Notices of the Royal Astronomical Society, **346**(1), 78–96. ISSN 0035-8711. URL http://adsabs.harvard.edu/abs/2003MNRAS.346...78H.

HENRY, J. P., SALVATO, M., FINOGUENOV, A., BOUCHE, N., BRUNNER, H., BURWITZ, V., BUSCHKAMP, P., EGAMI, E., FOERSTER-SCHREIBER, N., FOTOPOULOU, S., GENZEL, R., HASSINGER, G., MAINIERI, V., ROVILOS, M. & SZOKOLY, G., 2010. An X-ray Selected Galaxy Cluster in the Lockman Hole at Redshift 1.753. eprint arXiv:1010.0688. URL http://adsabs.harvard.edu/abs/2010arXiv1010.0688H.

HEWETT, P. C., WARREN, S. J., LEGGETT, S. K. & HODGKIN, S. T., 2006. The UKIRT Infrared Deep Sky Survey ZY JHK photometric system: passbands and synthetic colours. Monthly Notices of the Royal Astronomical Society, **367**(2), 454–468. ISSN 0035-8711. URL http://adsabs.harvard.edu/abs/2006MNRAS.367..454H.

HILDEBRANDT, H., ARNOUTS, S., CAPAK, P., MOUSTAKAS, L. A., WOLF, C. ET AL., 2010. PHAT: PHoto-z Accuracy Testing. 22. URL http://arxiv.org/abs/1008.0658.

HOPKINS, A. M., 2004. On the Evolution of Star-forming Galaxies. The Astrophysical Journal, **615**(1), 209–221. ISSN 0004-637X. URL http://adsabs.harvard.edu/abs/2004ApJ...615..209H.

ILBERT, O., ARNOUTS, S., MCCRACKEN, H. J., BOLZONELLA, M., BERTIN, E. ET AL., 2006. Accurate photometric redshifts for the CFHT legacy survey calibrated using the VIMOS VLT deep survey. Astronomy and Astrophysics, **457**(3), 841–856. ISSN 0004-6361. URL http://adsabs.harvard.edu/abs/2006A&A...457..841I.

ILBERT, O., CAPAK, P., SALVATO, M., AUSSEL, H., MCCRACKEN, H. J. ET AL., 2009. COSMOS PHOTOMETRIC REDSHIFTS WITH 30-BANDS FOR 2-deg 2. The Astrophysical Journal, **690**(2), 1236–1249. ISSN 0004-637X. URL http://adsabs.harvard.edu/abs/2009ApJ...690.1236I.

KAUFFMANN, G., HECKMAN, T. M., SIMON WHITE, D. M., CHARLOT, S., TREMONTI, C. ET AL., 2003. Stellar masses and star formation histories for 10 5 galaxies from the Sloan Digital Sky Survey. Monthly Notices of the Royal Astronomical Society, **341**(1), 33–53. ISSN 00358711. URL http://adsabs.harvard.edu/abs/2003MNRAS.341...33K.

KENNICUTT, R. C., 1998. STAR FORMATION IN GALAXIES ALONG THE HUBBLE SEQUENCE. Annual Review of Astronomy and Astrophysics, **36**(1), 189–231. ISSN 0066-4146. URL http://adsabs.harvard.edu/abs/1998ARA&A..36..189K.

KIMURA, M., MAIHARA, T., IWAMURO, F., AKIYAMA, M., TAMURA, N. ET AL., 2010. The Fibre Multi-Object Spectrograph (FMOS) for Subaru Telescope. 12. URL http://arxiv.org/abs/1006.3102.

KODAMA, T., ARIMOTO, N., BARGER, A. J. & ARAG'ON-SALAMANCA, A., 1998. Evolution of the colour-magnitude relation of early-type galaxies in distant clusters. Astronomy and Astrophysics. URL http://adsabs.harvard.edu/abs/1998A&A...334...99K.

KODAMA, T., SMAIL, I., NAKATA, F., OKAMURA, S. & BOWER, R. G., 2001. The Transformation of Galaxies within the Large-Scale Structure around a z=0.41 Cluster. The Astrophysical Journal, **562**(1), L9–L13. ISSN 0004637X. URL http://adsabs.harvard.edu/abs/2001ApJ...562L...9K.

KRIEK, M., VAN DOKKUM, P. G., FRANX, M., ILLINGWORTH, G. D., MARCHESINI, D., QUADRI, R., RUDNICK, G., TAYLOR, E. N., FÖRSTER SCHREIBER, N. M., GAWISER, E., LABBÉ, I., LIRA, P. & WUYTS, S., 2008. A Near-Infrared Spectroscopic Survey of K-selected Galaxies at z ˜ 2.3: Redshifts and Implications for Broadband Photometric Studies. The Astrophysical Journal, **677**(1), 219–237. URL http://adsabs.harvard.edu/abs/2008ApJ...677..219K.

LAWRENCE, A., WARREN, S. J., ALMAINI, O., EDGE, A. C., HAMBLY, N. C. ET AL., 2007. The UKIRT Infrared Deep Sky Survey (UKIDSS). Monthly Notices of the Royal Astronomical Society, **379**(4), 1599–1617. ISSN 0035-8711. URL http://adsabs.harvard.edu/abs/2007MNRAS.379.1599L.

LE FÈVRE, O., GUZZO, L., MENEUX, B., POLLO, A., CAPPI, A. ET AL., 2005. The VIMOS VLT deep survey. Astronomy and Astrophysics, **439**(3), 877–885. ISSN 0004-6361. URL http://adsabs.harvard.edu/abs/2005A&A...439..877L.

LILLY, S. J., LE FÈVRE, O., HAMMER, F. & CRAMPTON, D., 1996. The Canada-France Redshift Survey: The Luminosity Density and Star Formation History of the Universe to $z \sim 1$. The Astrophysical Journal, **460**(1). ISSN 0004637X. URL http://adsabs.harvard.edu/abs/1996ApJ...460L...1L.

LONSDALE, C. J., SMITH, H. E., ROWAN-ROBINSON, M., SURACE, J., SHUPE, D. ET AL., 2003. SWIRE: The SIRTF Wide-Area Infrared Extragalactic Survey. Publications of the Astronomical Society of the Pacific, **115**(810), 897–927. ISSN 0004-6280. URL http://adsabs.harvard.edu/abs/2003PASP..115..897L.

MAKOVOZ, D. & KHAN, I., 2005. Mosaicking with MOPEX. Astronomical Data Analysis Software and Systems XIV ASP Conference Series, **347**. URL http://adsabs.harvard.edu/abs/2005ASPC..347...81M.

MARINONI, C., LE FÈVRE, O., MENEUX, B., IOVINO, A., POLLO, A. ET AL., 2005. The VIMOS VLT Deep Survey. Astronomy and Astrophysics, **442**(3), 801–825. ISSN 0004-6361. URL http://adsabs.harvard.edu/abs/2005A&A...442..801M.

MENCI, N., FONTANA, A., GIALLONGO, E., GRAZIAN, A. & SALIMBENI, S., 2006. The Abundance of Distant and Extremely Red Galaxies: The Role of AGN Feedback in Hierarchical Models. The Astrophysical Journal, **647**(2), 753–762. ISSN 0004-637X. URL http://adsabs.harvard.edu/abs/2006ApJ...647..753M.

MONACO, P., FONTANOT, F. & TAFFONI, G., 2007. The morgana model for the rise of galaxies and active nuclei. Monthly Notices of the Royal Astronomical Society, **375**(4), 1189–1219. ISSN 00358711. URL http://adsabs.harvard.edu/abs/2007MNRAS.375.1189M.

NAGAMINE, K., OSTRIKER, J. P., FUKUGITA, M. & CEN, R., 2006. The History of Cosmological Star Formation: Three Independent Approaches and a Critical Test Using the Extragalactic Background Light. The Astrophysical Journal, **653**(2), 881–893. ISSN 0004-637X. URL http://adsabs.harvard.edu/abs/2006ApJ...653..881N.

OBSERVATORY, E. S., 2009. VERY LARGE TELESCOPE Issac pipeline user manual. Quality.

PEACOCK, J. A., COLE, S., NORBERG, P., BAUGH, C. M., BLAND-HAWTHORN, J. ET AL., 2001. A measurement of the cosmological mass density from clustering in the 2dF Galaxy Redshift Survey. Nature, **410**(6825), 169–73. ISSN 0028-0836. URL http://arxiv.org/abs/astro-ph/0103143.

PERCIVAL, W. J., REID, B. A., EISENSTEIN, D. J., BAHCALL, N. A., BUDAVARI, T. ET AL., 2010. Baryon acoustic oscillations in the Sloan Digital Sky Survey Data Release 7 galaxy sample. Monthly Notices of the Royal Astronomical Society, **401**(4), 2148–2168. ISSN 00358711. URL http://adsabs.harvard.edu/abs/2010MNRAS.401.2148P.

PERLMUTTER, S., ALDERING, G., GOLDHABER, G., KNOP, R. A., NUGENT, P. ET AL., 1999. Measurements of Ω and Λ from 42 High-Redshift Supernovae. The Astrophysical Journal, **517**(2), 565–586. ISSN 0004-637X. URL http://adsabs.harvard.edu/abs/1999ApJ...517..565P.

PICKLES, A. J., 1998. A Stellar Spectral Flux Library: 1150-25000 Å. Publications of the Astronomical Society of the Pacific, **110**(749), 863–878. ISSN 0004-6280. URL http://adsabs.harvard.edu/abs/1998PASP..110..863P.

POLLETTA, M., TAJER, M., MARASCHI, L., TRINCHIERI, G., LONSDALE, C. J. ET AL., 2007. Spectral Energy Distributions of Hard X-Ray Selected Active Galactic Nuclei in the XMM-Newton Medium Deep Survey. The Astrophysical Journal, **663**(1), 81–102. ISSN 0004-637X. URL http://adsabs.harvard.edu/abs/2007ApJ...663...81P.

RAYNER, J. T., CUSHING, M. C. & VACCA, W. D., 2009. THE INFRARED TELESCOPE FACILITY (IRTF) SPECTRAL LIBRARY: COOL STARS. The Astrophysical Journal Supplement Series, **185**(2), 289–432. ISSN 0067-0049. URL http://adsabs.harvard.edu/abs/2009ApJS..185..289R.

REACH, W. T., MEGEATH, S. T., COHEN, M., HORA, J., CAREY, S., SURACE, J., WILLNER, S. P., BARMBY, P., WILSON, G., GLACCUM, W., LOWRANCE, P., MARENGO, M. & FAZIO, G. G., 2005. Absolute Calibration of the Infrared Array Camera on the Spitzer Space Telescope. Publications of the Astronomical Society of the Pacific, **117**(835), 978–990. ISSN 0004-6280. URL http://adsabs.harvard.edu/abs/2005PASP..117..978R.

RIEKE, G. H., ALONSO-HERRERO, A., WEINER, B. J., PÉREZ-GONZÁLEZ, P. G., BLAYLOCK, M., DONLEY, J. L. & MARCILLAC, D., 2009. DETERMINING STAR FORMATION RATES FOR INFRARED GALAXIES. The Astrophysical Journal, **692**(1), 556–573. ISSN 0004-637X. URL http://adsabs.harvard.edu/abs/2009ApJ...692..556R.

RIESS, A. G., FILIPPENKO, A. V., CHALLIS, P., CLOCCHIATTI, A., DIERCKS, A. ET AL., 1998. Observational Evidence from Supernovae for an Accelerating Universe and a Cosmological Constant. The Astronomical Journal, **116**(3), 1009–1038. ISSN 00046256. URL http://adsabs.harvard.edu/abs/1998AJ....116.1009R.

RODIGHIERO, G., VACCARI, M., FRANCESCHINI, A., TRESSE, L., LE FEVRE, O. ET AL., 2010. Mid- and far-infrared luminosity functions and galaxy evolution from multiwavelength Spitzer observations up to z ˜ 2.5. Astronomy and Astrophysics, **515**, A8. ISSN 0004-6361. URL http://adsabs.harvard.edu/abs/2010A&A...515A...8R.

ROSS, N. P., DA ÂNGELA, J., SHANKS, T., WAKE, D. A., CANNON, R. D. ET AL., 2007. The 2dF-SDSS LRG and QSO Survey: the LRG 2-point correlation function and redshift-space distortions. Monthly Notices of the Royal Astronomical Society, **381**(2), 573–588. ISSN 0035-8711. URL http://adsabs.harvard.edu/abs/2007MNRAS.381..573R.

SANTINI, P., FONTANA, A., GRAZIAN, A., SALIMBENI, S., FIORE, F., FONTANOT, F., BOUTSIA, K., CASTELLANO, M., CRISTIANI, S., DE SANTIS, C., GALLOZZI, S., GIALLONGO, E., MENCI, N., NONINO, M., PARIS, D., PENTERICCI, L. & VANZELLA, E., 2009. Star formation and mass assembly in high redshift galaxies. Astronomy and Astrophysics, **504**(3), 751–767. ISSN 0004-6361. URL http://adsabs.harvard.edu/abs/2009A%26A...504..751S.

SEATON, M. J., 1979. Interstellar extinction in the UV. Royal Astronomical Society, **187**. URL http://adsabs.harvard.edu/abs/1979MNRAS.187P..73S.

SHAPLEY, A. E., STEIDEL, C. C., PETTINI, M. & ADELBERGER, K. L., 2003. Rest-Frame Ultraviolet Spectra of z˜3 lyman break galaxies. The Astrophysical Journal, **588**(1), 65–89. ISSN 0004-637X. URL http://adsabs.harvard.edu/abs/2003ApJ...588...65S.

SHARP, R. & PARKINSON, H., 2010. Sky subtraction at the Poisson limit with fibre-optic multi-object spectroscopy. 18. URL http://arxiv.org/abs/1007.0648.

SIMARD, L., WILLMER, C. N. A., VOGT, N. P., SARAJEDINI, V. L., PHILLIPS, A. C., WEINER, B. J., KOO, D. C., IM, M., ILLINGWORTH, G. D. & FABER, S. M., 2002. The DEEP Groth Strip Survey. II. Hubble Space Telescope Structural Parameters of Galaxies in the Groth Strip. The Astrophysical Journal Supplement Series, **142**(1), 1–33. ISSN 0067-0049. URL http://adsabs.harvard.edu/abs/2002ApJS..142....1S.

SOBRAL, D., BEST, P. N., GEACH, J. E., SMAIL, I., CIRASUOLO, M., GARN, T., DALTON, G. B. & KURK, J., 2010a. The clustering and evolution of Hα emitters at z $\sim$ 1 from HiZELS. Monthly Notices of the Royal Astronomical Society, **404**(3), 1551–1563. ISSN 00358711. URL http://adsabs.harvard.edu/abs/2010MNRAS.404.1551S.

SOBRAL, D., BEST, P. N., GEACH, J. E., SMAIL, I., KURK, J., CIRASUOLO, M., CASALI, M., IVISON, R. J., COPPIN, K. & DALTON, G. B., 2009. HiZELS: a high-redshift survey of Hα emitters - II. The nature of star-forming galaxies at z = 0.84. Monthly Notices of the Royal Astronomical Society, **398**(1), 75–90. ISSN 00358711. URL http://adsabs.harvard.edu/abs/2009MNRAS.398...75S.

SOBRAL, D., BEST, P. N., SMAIL, I., GEACH, J. E., CIRASUOLO, M., GARN, T. & DALTON, G. B., 2010b. The dependence of star formation activity on environment and stellar mass at z$\sim$ 1 from the HiZELS-Hα survey. Monthly Notices of the Royal Astronomical Society, **-1**, no–no. ISSN 00358711. URL http://adsabs.harvard.edu/abs/2010MNRAS.tmp.1657S.

SORBA, R. & SAWICKI, M., 2010. Using the 1.6um Bump to Study Rest-frame NIR Selected Galaxies at Redshift 2. eprint arXiv:1007.4951. URL http://adsabs.harvard.edu/abs/2010arXiv1007.4951S.

STOREY, P. J. & HUMMER, D. G., 1995. Recombination line intensities for hydrogenic ions-IV. Total recombination coefficients and machine-readable tables for Z=1 to 8. Monthly Notices of the Royal Astronomical Society, **272**(1), 41–48. URL http://adsabs.harvard.edu/abs/1995MNRAS.272...41S.

SUMIYOSHI, M., TOTANI, T., OSHIGE, S., GLAZEBROOK, K., AKIYAMA, M., MOROKUMA, T., MOTOHARA, K., SHIMASAKU, K., HAYASHI, M., YOSHIDA, M., KASHIKAWA, N. & KODAMA, T., 2009. Photometric H alpha and [O II] Luminosity Function of SDF and SXDF

Galaxies: Implications for Future Baryon Oscillation Surveys. eprint arXiv:0902.2064. URL http://adsabs.harvard.edu/abs/2009arXiv0902.2064S.

SURACE, J. A., SHUPE, D. L., FANG, F., LONSDALE, C. J. & HATZIMINAOGLOU, E., 2005. The SWIRE Data Release 2 : Image Atlases and Source Catalogs for. Source, 1–71.

VALDES, F., 1986. Reduction of long slit spectra with IRAF. Astronomy, (March).

VAN DOKKUM, P. G., 2001. Cosmic-Ray Rejection by Laplacian Edge Detection. URL http://arxiv.org/abs/astro-ph/0108003.

WARREN, S. J., CROSS, N. J. G., DYE, S., HAMBLY, N. C., ALMAINI, O. ET AL., 2007a. The UKIRT Infrared Deep Sky Survey Second Data Release. eprint arXiv:astro-ph/0703037. URL http://adsabs.harvard.edu/abs/2007astro.ph..3037W.

WARREN, S. J., HAMBLY, N. C., DYE, S., ALMAINI, O., CROSS, N. J. G. ET AL., 2007b. The United Kingdom Infrared Telescope Infrared Deep Sky Survey First Data Release. Monthly Notices of the Royal Astronomical Society, **375**(1), 213–226. ISSN 0035-8711. URL http://adsabs.harvard.edu/abs/2007MNRAS.375..213W.

WETTERICH, C., 1995. An asymptotically vanishing time-dependent cosmological "constant". Astronomy and Astrophysics. URL http://adsabs.harvard.edu/abs/1995A%26A...301..321W.

WILD, V., WALCHER, C. J., JOHANSSON, P. H., TRESSE, L., CHARLOT, S., POLLO, A., LE FÈVRE, O. & DE RAVEL, L., 2009. Post-starburst galaxies: more than just an interesting curiosity. Monthly Notices of the Royal Astronomical Society, **395**(1), 144–159. ISSN 00358711. URL http://adsabs.harvard.edu/abs/2009MNRAS.395..144W.

WORTHEY, G., 1994. Comprehensive stellar population models and the disentanglement of age and metallicity effects. The Astrophysical Journal Supplement Series, **95**, 107. ISSN 0067-0049. URL http://adsabs.harvard.edu/abs/1994ApJS...95..107W.

YEE, H. K. C., GLADDERS, M. D., GILBANK, D. G., MAJUMDAR, S., HOEKSTRA, H., ELLINGSON, E. & THE RCS-2 COLLABORATION, 2007. The Red-Sequence Cluster Surveys. eprint arXiv:astro-ph/0701839. URL http://adsabs.harvard.edu/abs/2007astro.ph..1839Y.